A Measurement of the Tau Electronic Branching Ratio

by

Steven Hugh Robertson

B.Sc., University of Calgary, 1990
B.Sc., University of Calgary, 1992
M.Sc., University of Victoria, 1994

A Dissertation Submitted in Partial Fulfillment of the
Requirements for the Degree of

DOCTOR OF PHILOSOPHY

in the Department of Physics and Astronomy.

We accept this dissertation as conforming
to the required standard

Dr. R. Sobie, Co-supervisor (Department of Physics and Astronomy)

Dr. R. Keeler, Co-supervisor (Department of Physics and Astronomy)

Dr. M. Lefebvre, Departmental Member (Department of Physics and Astronomy)

Dr. G. Beer, Departmental Member (Department of Physics and Astronomy)

Dr. C. Qian, Outside Member (Department of Chemistry)

Dr. P. Kitching, External Examiner (Department of Physics, University of Alberta)

Co-supervisor: Dr. R. Sobie

Co-supervisor: Dr. R. Keeler

Abstract

The branching ratio for the decay $\tau^- \to e^- \bar{\nu}_e \nu_\tau$ has been measured using data collected by the OPAL experiment at LEP. In total 33073 $\tau^- \to e^- \bar{\nu}_e \nu_\tau$ candidates were identified from a sample of 186197 selected τ decays, giving a branching ratio of $B(\tau^- \to e^- \bar{\nu}_e \nu_\tau) = (17.81 \pm 0.09\ (\text{stat}) \pm 0.06\ (\text{syst}))\%$. This result is combined with other electroweak measurements to test e - μ and μ - τ universality in charged-current weak interactions. Additionally, a value of the strong coupling constant $\alpha_s(m_\tau^2)$ has been extracted from $B(\tau^- \to e^- \bar{\nu}_e \nu_\tau)$ and evolved to the Z^0 mass scale to give $\alpha_s(m_Z^2) = 0.1204 \pm 0.0011\ (\text{exp}) \pm 0.0019\ (\text{theory})$.

Examiners:

Dr. R. Sobie, Co-supervisor (Department of Physics and Astronomy)

Dr. R. Keeler, Co-supervisor (Department of Physics and Astronomy)

Dr. M. Lefebvre, Departmental Member (Department of Physics and Astronomy)

Dr. G. Beer, Departmental Member (Department of Physics and Astronomy)

Dr. C. Qian, Outside Member (Department of Chemistry)

Dr. P. Kitching, External Examiner (Department of Physics, University of Alberta)

Contents

List of Tables

List of Figures

Chapter 1

Introduction

This thesis presents a measurement of the branching ratio $B(\tau^- \to e^- \bar{\nu}_e \nu_\tau)$ for the decay[1] of tau (τ) leptons into electrons (e) and neutrinos (ν) using data collected between 1991 and 1995 by the OPAL[2] collaboration. The OPAL detector is a general purpose experiment located at the LEP[3] collider at the European Centre for Particle Physics (CERN) near Geneva, Switzerland.

The branching ratio measurement is combined with other recent measurements of properties of the τ and muon (μ) in order to test the universality of leptonic charged-current couplings assumed by the Standard Model (SM) of electroweak interactions. Surprisingly, this fully leptonic electroweak decay channel can also be used to determine the strong coupling constant (α_s) which characterizes the strength of the strong interaction. Recent theoretical improvements have reduced the uncertainties associated with the determination of α_s presented in this thesis, making it competitive with the best α_s measurements currently available.

The thesis is organized as follows. The remainder of this chapter is used to give a

[1] Charge conjugation is assumed throughout this work. When quoted decay modes list only the negative charge state, the corresponding positive charge state is implied

[2] Omni Purpose Apparatus for LEP

[3] Large Electron Positron

conceptual overview of the physics context in which the analysis takes place. A more detailed discussion of the pertinent theory, including derivations of equations used in the analysis, is presented in chapter 2. Chapter 3 describes the experimental apparatus, including the LEP collider, the OPAL detector, and the event reconstruction and offline analysis hardware and software. Chapters 4 and 5 describe the selection of τ events from the OPAL data set, and the further selection of $\tau^- \to e^- \bar{\nu}_e \nu_\tau$ decays from the selected sample of τ-pair events. The $\tau^- \to e^- \bar{\nu}_e \nu_\tau$ branching ratio results are presented in chapter 6, along with an evaluation and discussion of experimental uncertainties. In chapter 7 this measurement is used to perform tests of the universality of leptonic charged-current couplings, and to evaluate the strong coupling constant α_s. Chapter 8 summarizes the results and presents the conclusions.

1.1 Theory overview

The interactions between fundamental particles via the electromagnetic (EM), weak and strong forces are described by the highly successful Standard Model (SM) [1]. Although recent precision measurements of electroweak quantities have tested the SM to a remarkable degree, no significant deviations from theoretical expectations have been observed. Any such deviation would be an indication of "new physics", either providing evidence supporting supersymmetry or similar theories, or possibly something completely unanticipated.

Within the SM, "matter" is composed of point-like spin 1/2 particles called *fermions* which interact with one another through four fundamental forces[4]. Fundamental fermions in the SM consist of two categories of particles: *quarks* which interact via all four of the fundamental forces, and *leptons* which do not interact by

[4] The fourth force is *gravity*.

Fermions (spin 1/2)

Leptons			Quarks		
Flavour	Charge	Mass (GeV)	Flavour	Charge	Mass (GeV)
ν_e	0	$< 1.5 \times 10^{-8}$	u	$+2/3$	$(1.5-5) \times 10^{-3}$
e^-	-1	5.110×10^{-4}	d	$-1/3$	$(3-9) \times 10^{-3}$
ν_μ	0	$< 1.7 \times 10^{-4}$	c	$+2/3$	$1.1-1.4$
μ^-	-1	0.1057	s	$-1/3$	$0.06-0.17$
ν_τ	0	$< 1.8 \times 10^{-2}$	t	$+2/3$	173.8 ± 5.2
τ^-	-1	1.777	b	$-1/3$	$4.1-4.4$

Table 1.1: Properties of the fermions in the Standard Model [2]. The charges are given in units of the positron (e^+) charge, and the vertical divisions separate the three fermion generations. Antiparticle states are not listed but are implied via charge conjugation.

the strong force. Essentially all of the physics within our everyday experience can be described using a model containing only four fundamental fermions: two quarks (u and d) and two leptons (ν_e and e^-), which together form the first *generation* of matter. The quarks each possess fractional electric charge: $+2/3$ for the u quark and $-1/3$ for the d quark (in units of the positron charge e). The electron (e^-) has charge -1, while the electron neutrino (ν_e) is neutral.

More exotic forms of matter composed of other fundamental fermions are observed in cosmic ray and particle accelerator experiments. These particles can be organized into two additional generations of fermions each consisting of two quarks and two leptons with properties which are identical to their first-generation counterparts in all respects except for their masses. The fundamental fermions therefore consist of the three charged leptons e^- (electron), μ^- (muon), and τ^- (tau), the three neutrino

Bosons (spin 1)

Force	Mediator(s)	Charge	Mass (GeV)
EM	photon (γ)	0	0
Weak	Z^0	0	91.187 ± 0.007
	W^+	$+1$	80.41 ± 0.10
	W^-	-1	80.41 ± 0.10
Strong	8 gluons (g)	0	0

Table 1.2: Properties of gauge bosons in the Standard Model [2].

flavours ν_e, ν_μ, ν_τ, and the six quarks flavours labeled (u, d, s, c, t, and b)[5]. Some of the properties of these fundamental fermions are listed in table 1.1. The fermions of each successive generation are typically an order of magnitude more massive than those of the previous generation. The reason for the existence of these recurring generations with this apparent mass hierarchy is one of the outstanding questions in particle physics.

The fundamental fermions interact with one another through the strong, weak and electromagnetic (EM) forces. The gravitational force is sufficiently weak at the length and mass scales accessible to particle physicists that its effects are negligible. Each of the fundamental forces is mediated by the exchange of integer-spin particles called *gauge bosons*, which couple to a "charge" carried by the fermion with a strength which is characteristic of the force. For example, the massless gauge boson associated with the EM force, the photon (γ), couples to the electron with a strength proportional to its electric charge ($-e$) as shown in figure 1.1a. The Coulomb repulsion between two electrons results from the exchange of these photons. The gauge bosons associated

[5]For each of the fundamental fermions mentioned above, there exists an additional fermion called an *antiparticle* of identical mass but with opposite quantum numbers. The most familiar of these is the positron e^+, which is the positively-charged counterpart of the electron e^-.

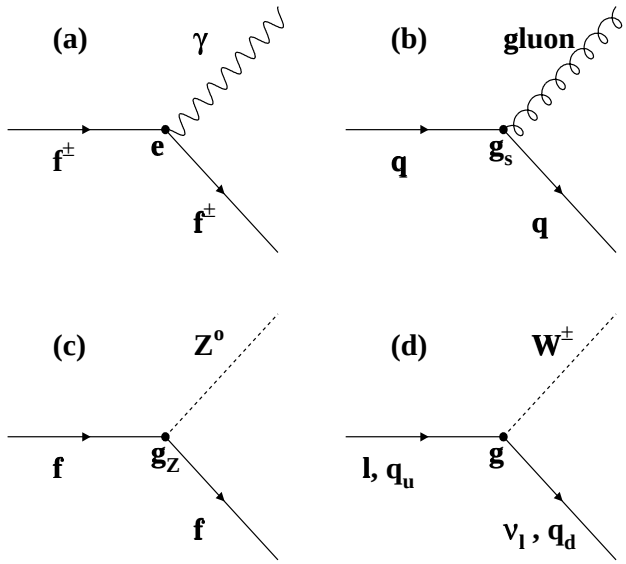

Figure 1.1: Fermion-boson vertices permitted in the SM: (a) the coupling of a photon (γ) to a charged fermion ($f^{\pm}$) with coupling constant e to give the EM force; (b) the coupling of a gluon to to a quark (q) to give the strong force; (c) the weak neutral-current coupling of a fermion (f) to a Z^0 and (d) the weak charged-current coupling of a $W^{\pm}$ to fermions. The weak charged-current couples u-type quarks to d-type quarks and charged leptons (l) to their associated neutrinos (ν_l).

with the strong, weak and EM forces are listed in table 1.2 and their couplings to fermions are illustrated in figure 1.1.

In general, the effective strength of each of the forces is dependent on the energy scale q^2 at which the interaction takes place.[6] At low energies the strength of the EM force is characterized by a dimensionless parameter called the fine structure constant[7]

$$\alpha \equiv \frac{e^2}{4\pi} \simeq \frac{1}{137} \sim 10^{-2} \quad .$$

This quantity is a measure of the electrostatic repulsion energy, as a fraction of the electron rest mass energy, of two electrons separated by a distance of one electron Compton wavelength ($\hbar/m_e c$).

[6]It is conventional to characterize the energy scale by the square of the exchanged four-momentum in an interaction, denoted by q^2 and with dimensions of GeV^2 (also see following footnote).

[7]Natural units ($\hbar = c = 1$) are used throughout this work unless otherwise explicitly stated.

The strength of the fundamental forces can be compared by defining similar measures for the remaining forces. Two electrons separated by this distance possess a gravitational potential energy of $\alpha_g \sim 10^{-45}$, many orders of magnitude smaller than the EM repulsion energy. By contrast, at an energy scale of the order of the proton mass ($q^2 \sim 1$ GeV^2), the strong coupling constant α_s is of order unity, and the charged-current weak interaction mediated by the $W^{\pm}$ has a coupling strength $\alpha_W \sim 10^{-6}$.

The apparent "weakness" of the weak force compared to the EM force is however misleading. At low energies, the large masses of the $W^{\pm}$ and Z^0 gauge bosons which mediate the weak force effectively suppress the weak coupling strength by a factor $(1/m_W)^2 \sim 10^{-4}$ compared to the EM force. This mass suppression becomes less important at energy scales on the order of $m_W \sim 10^2$ GeV^2, so that the EM and weak forces become of comparable strength at high q^2. As a result, the couplings e and g in figures 1.1a and d are actually of similar size, suggesting that the weak and EM forces may be "unified" at these energy scales. Unification implies that the two forces can be described by a common theory and a common coupling constant. For example, the electric and and magnetic forces are unified in Maxwell's theory of electromagnetism by identifying the "charge" associated with the magnetic force e_M with the electric charge e to give the Lorentz force:

$$F = \overbrace{eE}^{\text{electric}} + \overbrace{e_M(v \times B)}^{\text{magnetic}} = e(E + v \times B) \quad .$$

In a relativistic theory, these two forces are inseparable, and appear as two manifestations of the same force. At low velocities the magnetic force appears to be much weaker than the electric force, but the two become of comparable strength at high velocities.

A partial unification of the weak and EM forces was achieved by Glashow, Salam and Weinberg (GSW) [3] who constructed a model of electroweak interactions based on a spontaneously broken local gauge symmetry. In this model the weak and EM forces are intrinsically linked, but full unification is not achieved because there remain two separate coupling constants. It is currently believed that all of the fundamental forces are actually manifestations of a single "unified" force, and that at sufficiently high energies these forces will be indistinguishable, and described by a common theory with only a single coupling constant. Unification of the strong and electroweak forces is expected to occur at an energy scale of $q^2 \sim 10^{15}$ GeV, far beyond the reach of foreseeable accelerator-based physics experiments.

At the much lower energy scales currently accessible to experiments, the couplings α_s, α_W, and α are found to be very different from one another. This is a consequence of the *running* of the coupling constants with q^2. In a quantum field theory, a single "charge" cannot exist in isolation. Its presence induces a "cloud" of *virtual* particles which surround the charge and effectively polarize the vacuum in a manner analogous to an electric charge polarizing a dielectric material. Depending on the nature of the charge (i.e. electromagnetic, weak or strong), this polarization will either increase or decrease the effective field strength which would be experienced by a test charge placed at some distance from the original charge. In the case of the EM force, this effect is known as *charge screening*, and it reduces the strength of the EM field at large distances and hence the effective strength of the EM force at low q^2. As q^2 increases, the test charge penetrates more of this cloud of virtual charged particles thereby reducing the amount of charge screening so that the test charge experiences more of the "bare" charge. The coupling strength $\alpha \equiv \alpha(q^2)$ slowly increases with q^2 in a manner that is characteristic of the symmetry group underlying the gauge

field theory. The running of the coupling constants with q^2 is quantified by a process known as *renormalization group evolution*.

In contrast to the EM force, the strong force exhibits a sort of "anti-screening" which causes the effective strong-charge, called *colour*, to increase with increasing distance from the original bare charge. This causes $\alpha_s(q^2)$ to decrease with increasing q^2, a property known as *asymptotic freedom*. In fact, beyond a distance of approximately 10^{-15} m, the colour charge becomes so strong that the potential energy between two quarks exceeds the mass-energy of light quark-antiquark pairs, and real particles can be created from the vacuum. This has the consequence that quarks have never been observed to exist in isolation, appearing only in bound states of two or three quarks referred to collectively as *hadrons*. The observed bound states of quarks are colour-singlets possessing zero or integer values of electric charge and consisting of either a quark and an anti-quark (*mesons*), or a combination of three quarks or three anti-quarks (*baryons*).

1.2 Analysis overview

In the work presented here, the branching ratio has been evaluated for the decay $\tau^- \to e^- \bar{\nu}_e \nu_\tau$ [4]. This process, which proceeds via the charged-current weak interaction mediated by the $W^\pm$, is well defined and calculable within the SM. Because this decay channel is comparatively "clean" from an experimental point of view, it is suitable for use as a precision test of SM predictions. The required precision of better than $\sim 1\%$ demands that systematic uncertainties due to Monte Carlo modelling of detector performance be carefully controlled and that non-τ background contributions in the τ sample be well understood. Candidate $\tau^- \to e^- \bar{\nu}_e \nu_\tau$ decays are identified from the sample of τ decays using a procedure based on a likelihood

selection. This selection has been carefully constructed to be robust against potential measurement biases due to the possible mis-modelling of the selection variables and has been throughly tested for any such biases.

Comparison of this branching ratio measurement with other leptonic decay processes ($\tau^- \to \mu^- \bar{\nu}_\mu \nu_\tau$ and $\mu^- \to \mathrm{e}^- \bar{\nu}_\mathrm{e} \nu_\mu$) can test the SM assumption that the weak force couplings to the different lepton generations are identical. Any measured deviation in these couplings would be an indication of non-SM physics or neutrino mass and could shed some light on the problem of recurring fermion generations. These tests of the universality of leptonic charged-current couplings are described in section 2.3.

Because this branching ratio measurement expresses the partial decay width for $\tau^- \to \mathrm{e}^- \bar{\nu}_\mathrm{e} \nu_\tau$ as a fraction of the total τ decay width, its value is sensitive to the τ partial decay width to hadronic final states. Since the τ hadronic decay width is subject to large contributions due to the strong force, this branching ratio measurement can be used to make indirect tests of QCD, the gauge field theory of the strong interaction. In particular, a measurement of the strong coupling constant $\alpha_s(m_\tau^2)$ can be made at the τ mass scale ($m_\tau = 1777.0 \pm 0.3$ MeV/c^2) [2] as is described in section 2.4. This result is evolved to the Z^0 mass scale ($m_\mathrm{Z} = 91.187 \pm 0.007$ GeV) [2] for comparison with direct measurements of $\alpha_s(m_\mathrm{Z}^2)$, providing a stringent test of renormalization group evolution and QCD. Because of the large sensitivity of this measurement to α_s and the comparatively small theoretical uncertainties associated with it, this method gives one of the most precise determinations of the strong coupling constant to date.

Chapter 2

Theory

2.1 The Weak Interaction

The SM is constructed by combining the GSW model of electroweak interactions with quantum chromodynamics (QCD), the theory of the strong interaction. Both of these are based on quantum field theories in which the interactions between fermions arise as a result of the invariance of the SM Langrangian under a class of local symmetry transformations called *gauge transformations*. The internal symmetries of the SM are described by the group structure $SU(3)_c \times SU(2)_L \times U(1)_Y$, where the $SU(3)_c$ group structure defines the couplings between strongly interacting particles by the exchange of colour (c) carrying gauge bosons called *gluons*, and the $SU(2)_L \times U(1)_Y$ groups define the electroweak interaction. The subscript L indicates that the charged-current weak force couples only to left-handed fermions. The subscript Y denotes the weak hypercharge, defined by $Q = T^3 + Y/2$ where Q is the electric charge and T^3 is the third component of the weak isospin. The local structure of each of these symmetries requires the introduction of a set of massless gauge bosons which mediate the interaction. The limited range and suppression of the weak force relative to the EM force indicates however that the gauge bosons associated with these interactions

Leptons	T	T^3	Y	Quarks	T	T^3	Y
ν_e	1/2	1/2	-1	u_L	1/2	1/2	1/3
e_L^-	1/2	$-1/2$	-1	d_L	1/2	$-1/2$	1/3
				u_R	0	0	4/3
e_R^-	0	0	-2	d_R	0	0	$-2/3$

Table 2.1: Weak isospin (T) and weak hypercharge (Y) assignments for the leptons and quarks. The third component T^3 of the weak isospin is given by $T^3 = Q - Y/2$ and the left and right-handed chiral states are denoted by the subscripts L and R. The second and third generation fermions have identical isospin and hypercharge assignments as their first generation counterparts.

are in fact massive, and so a way had to be found to incorporate massive gauge bosons into the theory without destroying the symmetry of the Lagrangian. In the GSW model, the $SU(2)_L \times U(1)_Y$ symmetry of the Lagrangian is spontaneously broken by the introduction of a scalar Higgs field [5], leaving a residual $U(1)_Q$ symmetry which is associated with the EM interaction. The coupling of the Higgs field to the weak gauge bosons and fermions is found to introduce the appropriate mass terms into the SM Lagrangian in a gauge invariant, Lorentz invariant and renormalizable way. However, the presence of this field implies the existence of a massive scalar particle known as the Higgs boson which has yet to be observed.

After symmetry breaking, the "unified" electroweak force is resolved into the separate EM and weak forces. The photon (γ), which is the gauge boson associated with the residual $U(1)_Q$ gauge symmetry of the EM interaction, remains massless. The three gauge bosons $W^{\pm}$ and Z^0, associated with the weak interaction become massive. The $W^{\pm}$ and Z^0 bosons were discovered at CERN in 1983 [6, 7, 8, 9]. Since then the masses and couplings of these particles have been measured by experimental collaborations at Fermilab and at CERN, providing stringent tests of the SM. To

date, no deviations from SM predictions have been observed [2].

Neutral-current weak interactions such as that shown in figure 1.1c are mediated by the Z^0. Neutral-current processes which change a fermion's "flavour", for example a charm (c) quark to an up (u) quark, are not permitted by the SM. In contrast, the charged-current weak interaction, mediated by the $W^{\pm}$, couples charged leptons (l) to their associated neutrino (ν_l), and u-type quarks to d-type quarks as shown in figure 1.1d. The charged-current weak interaction maximally violates parity conservation [10, 11] by coupling only to left-handed (right-handed) particles (antiparticles). The leptons and quarks are therefore organized into left-handed $SU(2)$ doublets with weak isospin $T = 1/2$ and right-handed $SU(2)$ singlets ($T = 0$) as shown in table 2.1. Because the right-handed neutrino (left-handed antineutrino) state does not interact via the strong, weak or EM forces it is not included in the SM.

Charged-current interactions can also couple quarks from one generation to quarks of another generation, permitting the heavier quarks to decay into quarks of the lighter generations. This "mixing" of quark generations is possible because the quark mass eigenstates are "rotated" relative to the weak interaction eigenstates in a manner that is parameterized in the SM by the CKM matrix [12]. A similar mixing between the lepton generations is not permitted in the SM because the absence or near-absence of neutrino mass guarantees that the weak eigenstates and mass eigenstates are essentially identical. Recent experimental evidence for non-zero neutrino mass suggests that some mixing does occur [13].

2.2 The τ Lepton

The τ lepton provides a unique probe for the investigation of both the electroweak and strong sectors of the SM, and may be sensitive to physics beyond the SM. Due to

its large mass, the τ is the only lepton for which hadronic decay modes are kinematically allowed. The τ lepton may also provide insight into the origin of the recurring generations of fundamental fermions. The τ was discovered by Perl *et al.* [14] at the SPEAR e^+e^- storage ring in 1975 through the observation of acollinear $e^+e^- \to e^+\mu^-$ events below the D-meson production threshold.

The τ is a sequential lepton, that is, a point-like spin 1/2 particle with properties and couplings which are believed to be identical to those of the electron and muon, differing from them only in mass. As such, the left-handed τ is the $T^3 = -1/2$ component of a $SU(2)_L$ weak isospin doublet

$$\begin{pmatrix} \nu_\tau \\ \tau \end{pmatrix}$$

with the tau-neutrino (ν_τ) as its $T^3 = +1/2$ partner. The τ decays via the charged-current weak interaction with a lifetime of $\tau_\tau = (290.0 \pm 1.2)$ fs [2]. The lifetime τ_τ is related to the total τ decay width Γ_τ by $\tau_\tau = 1/\Gamma_\tau$, where Γ_τ is the sum of the *partial decay widths* $\Gamma_{\tau\to X}$ of τ decays into some final state represented by X. The *branching ratio* for the decay $(\tau \to X)$ is defined as the ratio of the partial decay width to the full width

$$\mathrm{B}(\tau \to X) = \frac{\Gamma_{\tau\to X}}{\Gamma_\tau} \tag{2.1}$$

and therefore represents the fraction of τ leptons which decay to this final state.

The permissible final states X can be deduced from figure 1.1d and from the τ mass. The two fully-leptonic decays $\tau^- \to e^-\bar{\nu}_e\nu_\tau$ and $\tau^- \to \mu^-\bar{\nu}_\mu\nu_\tau$ are both kinematically allowed, as well as hadronic final states resulting from the decay of a virtual $W^\pm$ into quark-antiquark pairs composed of u, d or s quarks. Because the form of the weak charged-current coupling is fully specified within the SM, the leptonic partial decay widths can be precisely computed. The total width however depends on the

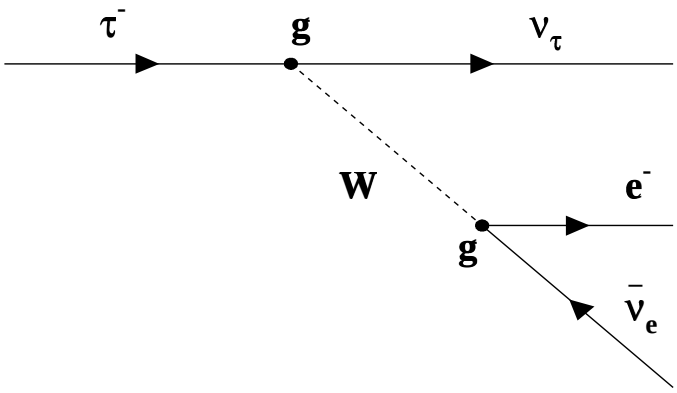

Figure 2.1: Feynman diagram for the decay $\tau^- \rightarrow \mathrm{e}^-\bar{\nu}_\mathrm{e}\nu_\tau$. Lepton universality implies that the couplings at the the two W boson vertices are both g.

contributions from τ decays to hadrons and are sensitive to QCD effects. Since the leptonic branching ratios depend on the total width, they contain information which can be used to extract QCD measurements.

The Feynman diagram for a $\tau^- \rightarrow \mathrm{e}^-\bar{\nu}_\mathrm{e}\nu_\tau$ decay is illustrated in figure 2.1. The initial state τ^- couples with strength g to a (virtual) W-boson and a τ neutrino (ν_τ). The $\mathrm{W}^\pm$ then decays to an electron and an electron antineutrino via a similar vertex. The assumption of lepton universality implies that the coupling strength at the W-boson decay vertex is also g. The partial decay width $\Gamma_{\tau^- \rightarrow \mathrm{e}^-\bar{\nu}_\mathrm{e}\nu_\tau}$ can be computed by integrating the differential width

$$\mathrm{d}\Gamma_{\tau^- \rightarrow \mathrm{e}^-\bar{\nu}_\mathrm{e}\nu_\tau} = \frac{1}{2\mathrm{m}_\tau}\,\overline{|\mathcal{M}|}^2\,\mathrm{d}\mathcal{Q}$$

over the available Lorentz invariant phase space $\mathcal{Q}$. The quantity m_τ represents the τ mass and the *matrix element* $\mathcal{M}$ is given by

$$\mathcal{M} = \left(\frac{g}{\sqrt{2}}\;\bar{\nu}_\tau\;\gamma^\mu\frac{1}{2}(1-\gamma^5)\;\tau\right)\frac{1}{m_\mathrm{W}^2 - q^2}\left(\frac{g}{\sqrt{2}}\;\bar{\mathrm{e}}\;\gamma^\mu\frac{1}{2}(1-\gamma^5)\;\nu_\mathrm{e}\right) \qquad (2.2)$$

where $\bar{\nu}_\tau$, τ, $\bar{\mathrm{e}}$ and ν_e are Dirac spinors and γ^μ and γ^5 are the Dirac γ matrices. In the limit $q^2 \ll m_\mathrm{W}^2$, the $\mathrm{W}^\pm$ propagator reduces to $1/m_\mathrm{W}^2$ and the decay can be treated as a Fermi four-point interaction. Neglecting the masses of the final state leptons, averaging over the initial spin states and summing over the final spin states, gives the partial decay width

$$\Gamma_{\tau^- \to \mathrm{e}^- \bar{\nu}_\mathrm{e} \nu_\tau} = \left(\frac{g^2}{8\, m_\mathrm{W}^2} \right)^2 \frac{m_\tau^5}{96\pi^3} \quad . \tag{2.3}$$

An identical expression is obtained for the $\tau^- \to \mu^- \bar{\nu}_\mu \nu_\tau$ partial decay width.

A more precise prediction for the $\tau^- \to \mathrm{e}^- \bar{\nu}_\mathrm{e} \nu_\tau$ decay width can be obtained by including the final state lepton masses, the full $\mathrm{W}^\pm$ propagator and electroweak radiative corrections. Taking the neutrino masses to be zero and including electroweak radiative corrections of $\mathcal{O}(\alpha)$, the partial decay width is given by [15, 16]

$$\Gamma(\tau^- \to \mathrm{e}^- \bar{\nu}_\mathrm{e} \nu_\tau) = \left(\frac{g^2}{8\, m_\mathrm{W}^2} \right)^2 \frac{m_\tau^5}{96\pi^3}\, f\left(\frac{m_\mathrm{e}^2}{m_\tau^2} \right) \left[1 + \frac{3 m_\tau^2}{5 m_\mathrm{W}^2} \right] \left[1 + \frac{\alpha(m_\tau^2)}{2\pi} \left(\frac{25}{4} - \pi^2 \right) \right] \tag{2.4}$$

where m_W is the mass of the $\mathrm{W}^\pm$ boson, and m_τ and m_e are the τ mass and the electron mass respectively. The two terms in square brackets are corrections for the non-local structure of the $\mathrm{W}^\pm$ propagator, and photon radiative corrections respectively. Some QED corrections are absorbed into the fine structure constant to give an effective $\alpha(m_\tau)$ appropriate to the τ mass scale [16]:

$$\alpha^{-1}(m_\tau) \simeq \alpha^{-1} - \frac{2}{3\pi} \ln\left(\frac{m_\tau}{m_\mathrm{e}} \right) + \frac{1}{6\pi} = 133.29 \quad . \tag{2.5}$$

The function

$$f(x) = 1 - 8x + 8x^3 - x^4 - 12x^2 \ln(x) \tag{2.6}$$

results from the integration over the three body final state phase space, and is effectively equal to unity for $\tau^- \to \mathrm{e}^- \bar{\nu}_\mathrm{e} \nu_\tau$ decays.

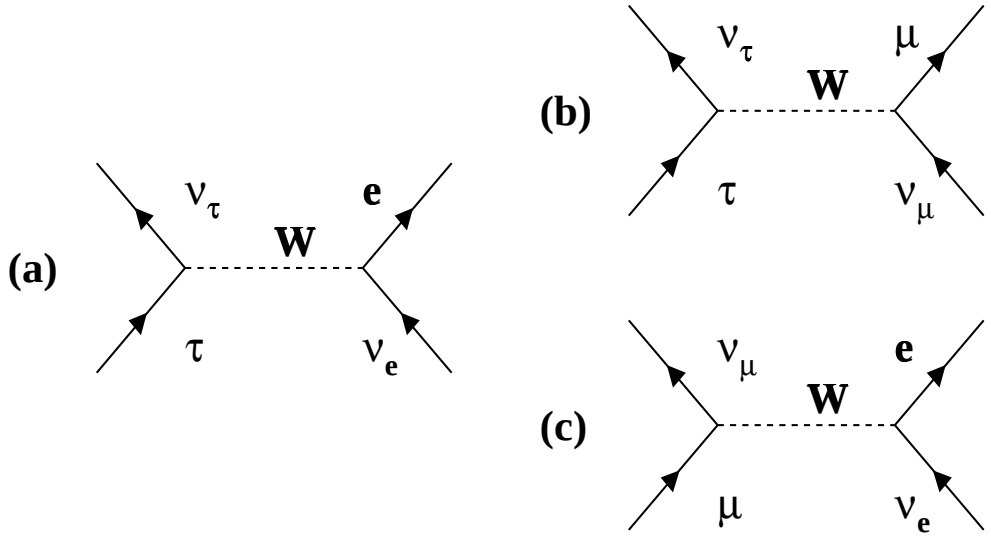

Figure 2.2: Leptonic decays which are used for tests of lepton universality. A comparison of the decays $\tau^- \to \mathrm{e}^-\bar{\nu}_\mathrm{e}\nu_\tau$ (a) and $\tau^- \to \mu^-\bar{\nu}_\mu\nu_\tau$ (b) gives a measure of g_μ/g_e, while a comparison of $\tau^- \to \mathrm{e}^-\bar{\nu}_\mathrm{e}\nu_\tau$ and $\mu^- \to \mathrm{e}^-\bar{\nu}_\mathrm{e}\nu_\mu$ (c) gives a measure of g_τ/g_μ.

2.3 Lepton Universality

If lepton universality does not hold, the charged-current couplings of the τ and the daughter lepton are not necessarily equal, and equation 2.4 becomes

$$\Gamma(\tau^- \to l^-\bar{\nu}_l\nu_\tau) = \frac{g_\tau^2 g_l^2}{(8m_\mathrm{W}^2)^2}\frac{m_\tau^5}{96\pi^3} f\left(\frac{m_l^2}{m_\tau^2}\right)\left[1+\frac{3m_\tau^2}{5m_\mathrm{W}^2}\right]\left[1+\frac{\alpha(m_\tau^2)}{2\pi}\left(\frac{25}{4}-\pi^2\right)\right] \quad (2.7)$$

where l represents either e or μ, and g_τ and g_l are the $\mathrm{W}^\pm$ couplings at the τ - ν_τ and l - ν_l vertices respectively. Taking the ratio of the partial decay widths for τ decays into muons ($\tau^- \to \mu^-\bar{\nu}_\mu\nu_\tau$) and electrons ($\tau^- \to \mathrm{e}^-\bar{\nu}_\mathrm{e}\nu_\tau$) gives

$$\frac{\Gamma(\tau^- \to \mu^-\bar{\nu}_\mu\nu_\tau)}{\Gamma(\tau^- \to \mathrm{e}^-\bar{\nu}_\mathrm{e}\nu_\tau)} = \frac{\mathrm{B}(\tau^- \to \mu^-\bar{\nu}_\mu\nu_\tau)}{\mathrm{B}(\tau^- \to \mathrm{e}^-\bar{\nu}_\mathrm{e}\nu_\tau)} = \frac{g_\mu^2}{g_e^2}\left[\frac{f\left(\frac{m_\mu^2}{m_\tau^2}\right)}{f\left(\frac{m_e^2}{m_\tau^2}\right)}\right] \quad . \quad (2.8)$$

The two leptonic τ decay modes are illustrated in figure 2.2. Since the phase-space factors $f(x)$ are known, the ratio of the coupling constants g_μ/g_e can be determined

from experimental measurements of the two branching ratios $\mathrm{B}(\tau^- \to \mathrm{e}^-\bar{\nu}_\mathrm{e}\nu_\tau)$ and $\mathrm{B}(\tau^- \to \mu^-\bar{\nu}_\mu\nu_\tau)$.

A second test of lepton universality can be made by taking the ratio of the partial decay widths for the decays $\tau^- \to \mathrm{e}^-\bar{\nu}_\mathrm{e}\nu_\tau$ and $\mu^- \to \mathrm{e}^-\bar{\nu}_\mathrm{e}\nu_\mu$ shown in figures 2.2a and 2.2c respectively. The partial decay width $\Gamma(\mu^- \to \mathrm{e}^-\bar{\nu}_\mathrm{e}\nu_\mu)$ can be obtained by substituting the muon mass m_μ for m_τ in equation 2.4, and obtaining $\alpha(m_\mu^2)$ from equation 2.5. The ratio of the partial decay widths is then given by

$$\frac{\Gamma(\tau^- \to \mathrm{e}^-\bar{\nu}_\mathrm{e}\nu_\tau)}{\Gamma(\mu^- \to \mathrm{e}^-\bar{\nu}_\mathrm{e}\nu_\mu)} = \frac{g_\tau^2\, m_\tau^5\, f\,(m_\mathrm{e}^2/m_\tau^2)\,\delta_W^\tau\delta_\gamma^\tau}{g_\mu^2\, m_\mu^5\, f\left(m_\mathrm{e}^2/m_\mu^2\right)\delta_W^\mu\delta_\gamma^\mu} \tag{2.9}$$

where δ_W^τ and δ_W^μ are the $\mathrm{W}^\pm$ propagator corrections and δ_γ^τ and δ_γ^μ are the radiative corrections to $\tau^- \to \mathrm{e}^-\bar{\nu}_\mathrm{e}\nu_\tau$ and $\mu^- \to \mathrm{e}^-\bar{\nu}_\mathrm{e}\nu_\mu$ respectively. Substituting numerical values for the correction factors, the ratio of the coupling constants can be expressed in terms of the $\tau^- \to \mathrm{e}^-\bar{\nu}_\mathrm{e}\nu_\tau$ branching ratio, and the lifetimes τ_τ and τ_μ of the τ and muon respectively:

$$\left(\frac{g_\tau}{g_\mu}\right)^2 = 0.9996\,\frac{\tau_\mu}{\tau_\tau}\frac{m_\mu^5}{m_\tau^5}\,\mathrm{B}(\tau^- \to \mathrm{e}^-\bar{\nu}_\mathrm{e}\nu_\tau) \quad . \tag{2.10}$$

Using experimentally determined values for these quantities, the equality of g_τ and g_μ can be tested.

2.4 Determination of α_s from τ decays

The τ is the only lepton which is sufficiently heavy to be able to decay into hadrons. As a result, it is possible to test the theory of the strong interaction (QCD) at the τ mass scale in an experimentally clean environment [17, 18, 19, 20]. It is believed that τ decay is the lowest energy process for which the strong coupling constant α_s can be obtained without prohibitively large theoretical uncertainties due to non-perturbative

effects [19]. A measurement of α_s is possible because of the inclusive nature of the τ semihadronic decay rate, which is expressed in terms of the τ hadronic decay width $\Gamma(\tau^- \to \text{hadrons } \nu_\tau)$ normalized to the electronic decay width:

$$R_\tau \equiv \frac{\Gamma(\tau^- \to \text{hadrons } \nu_\tau)}{\Gamma(\tau^- \to \mathrm{e}^-\bar{\nu}_\mathrm{e}\nu_\tau)} \quad . \tag{2.11}$$

If final-state particle masses and electroweak radiative corrections are neglected, universality of charged-current couplings to fermions implies that

$$R_\tau \simeq N_c(|V_{\mathrm{ud}}|^2 + |V_{\mathrm{us}}|^2) \simeq 3 \tag{2.12}$$

where N_c is the number of colour degrees of freedom, and V_{ud} and V_{us} are CKM matrix elements. It is worth noting that the approximate agreement between this naive prediction and experiment provides strong evidence for the colour degree of freedom. However, deviations of the order of 20% are observed from this parton level prediction, and these can be accounted for in terms of QCD dynamics. Due to the low energy scale ($q^2 \sim m_\tau^2$), the strong coupling constant α_s is comparatively large in value ($\alpha_s(m_\tau^2) \sim 0.35$ compared to $\alpha_s(m_\mathrm{Z}^2) \sim 0.12$). Consequently, perturbative QCD corrections to R_τ are sufficiently large that a value of α_s can be extracted from a measurement of R_τ. Moreover, the τ mass fortuitously lies in a region where the non-perturbative contributions to R_τ are comparatively small, so that the theoretical uncertainties on this measurement are not overwhelming.

The complete discussion of R_τ is beyond the scope of this work, however the derivation is outlined here for the sake of completeness. This derivation begins with the vector and axial-vector colour singlet quark currents $V_{ij}^\mu = \bar{\psi}_i\gamma^\mu\psi_j$ and $A_{ij}^\mu = \bar{\psi}_i\gamma^\mu\gamma_5\psi_j$, where the indices i, j indicate the light quark flavours (u,d,s). The two point correlation functions

$$\Pi_{ij,V}^{\mu\nu}(q) \equiv i\int d^4x e^{iqx}\langle 0|T(V_{ij}^\mu(x)V_{ij}^\nu(0)^\dagger)|0\rangle \tag{2.13}$$

$$\Pi^{\mu\nu}_{ij,A}(q) \equiv i\int d^4x e^{iqx}\langle 0|T(A^{\mu}_{ij}(x)A^{\nu}_{ij}(0)^{\dagger})|0\rangle$$

can be written as a Lorentz decomposition in terms of the transverse (helicity ± 1) and longitudinal (helicity 0) components

$$\Pi^{\mu\nu}_{ij,V/A}(q) = (-g^{\mu\nu}q^2 + q^{\mu}q^{\nu})\Pi^{(1)}_{ij,V/A}(q^2) + q^{\mu}q^{\nu}\Pi^{(0)}_{ij,V/A}(q^2) \tag{2.14}$$

The imaginary parts of the correlators $\Pi^{(J)}_{ij,V/A}(q^2)$ are proportional to the spectral functions for hadronic final states with angular momentum J. The hadronic decay rate R_τ is an integral with respect to the square of the invariant mass $s = q^2$ of these spectral functions:

$$R_\tau = 12\pi\int_0^{m_\tau^2}\frac{ds}{m_\tau^2}\left(1-\frac{s}{m_\tau^2}\right)^2\left[\left(1+2\frac{s}{m_\tau^2}\right)\cdot \mathrm{Im}\Pi^{(1)}(\mathrm{s}+\mathrm{i}\epsilon) + \mathrm{Im}\Pi^{(0)}(\mathrm{s}+\mathrm{i}\epsilon)\right] \tag{2.15}$$

where the correlators $\Pi^{(1)}(s)$ and $\Pi^{(0)}(s)$ are linear combinations of the correlators for the various light quark flavours:

$$\Pi^{(J)}(s) = |V_{\mathrm{ud}}|^2\left(\Pi^{(J)}_{\mathrm{ud,V}}(s) + \Pi^{(J)}_{\mathrm{ud,A}}(s)\right) + |V_{\mathrm{us}}|^2\left(\Pi^{(J)}_{\mathrm{us,V}}(s) + \Pi^{(J)}_{\mathrm{us,A}}(s)\right) \quad . \tag{2.16}$$

V_{ud} and V_{us} are CKM matrix elements. The hadronic spectral functions in equation 2.15 are analytic functions over the entire complex plane except along the positive real axis. It is possible to use this analyticity to transform the integral of equation 2.15 into a contour integral over the circle $|s| = m_\tau^2$ as shown in figure 2.3

$$R_\tau = 6\pi i\oint_{|s|=m_\tau^2}\frac{ds}{m_\tau^2}\left(1-\frac{s}{m_\tau^2}\right)^2\left[\left(1+2\frac{s}{m_\tau^2}\right)\cdot \mathrm{Im}\Pi^{(1)}(\mathrm{s}) + \mathrm{Im}\Pi^{(0)}(\mathrm{s})\right] \quad . \tag{2.17}$$

The integrand can be evaluated by expressing the correlators in terms of the Operator Product Expansion (OPE) [21] and evaluating the dominant condensates (vacuum expectation values), to estimate the non-perturbative corrections. The OPE is given

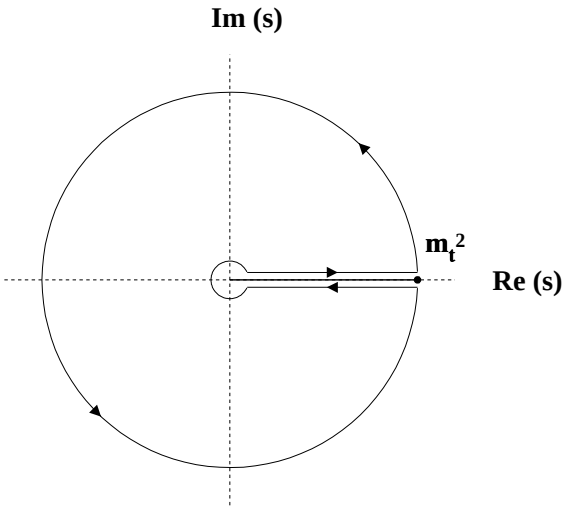

Figure 2.3: The integral 2.15 along the real axis is evaluated by transforming it into an integral in the complex plane over the contour shown.

by

$$\Pi^{(J)}(s) = \sum_{D=2,4,\ldots} \frac{1}{(-s)^{D/2}} \sum_{dim\ \mathcal{O}=D} \mathcal{C}^{(J)}(s,\mu)\langle\mathcal{O}(\mu)\rangle \tag{2.18}$$

where the second sum is over all local gauge invariant scalar operators $\mathcal{O}$ of dimension D. The factorization scale μ separates long distance non-perturbative effects from short-distance effects. The former are then absorbed into the vacuum matrix elements $\langle\mathcal{O}(\mu)\rangle$, while the latter are described by the Wilson coefficients $\mathcal{C}^{(J)}(s,\mu)$.

The ratio R_τ is then conveniently expressed in terms of the fractional corrections $\delta^{(D)}$ of mass dimension D to the "naive" prediction of equation 2.12:

$$R_\tau = 3\left(|V_{\rm ud}|^2 + |V_{\rm us}|^2\right) S_{EW} \left\{1 + \delta_{EW} + \delta^{(0)} + \sum_{D=2,4,\ldots} \delta^{(D)}\right\} \tag{2.19}$$

where $\delta^{(D)}$ are corrections to R_τ resulting from QCD condensates which are suppressed by $1/m_\tau^D$. The factors $S_{EW} = 1.0194 \pm 0.0040$ [16] and $\delta_{EW} = (5/12)\alpha(m_\tau)/\pi \simeq 0.0010$ [22] are electroweak corrections, while the CKM matrix elements have values

$V_{ud} = 0.9753 \pm 0.0008$ and $V_{us} = 0.2205 \pm 0.0018$ [2] and $\alpha(m_\tau) = 1/133.29$ is the running QED coupling constant at the τ mass scale.

Perturbative QCD corrections contribute to equation 2.19 at dimension $D = 0$ and have been calculated to order $({\alpha_s}^3)$ [18] in the limit of massless quarks:

$$\delta^{(0)} = \left(\frac{\alpha_s(m_\tau^2)}{\pi}\right) + 5.2023\left(\frac{\alpha_s(m_\tau^2)}{\pi}\right)^2 + 26.366\left(\frac{\alpha_s(m_\tau^2)}{\pi}\right)^3 + \mathcal{O}({\alpha_s}^4) \quad . \qquad (2.20)$$

The numerical coefficient in front of the term of $\mathcal{O}({\alpha_s}^4)$ is $(78.00 + K_4)$, where the K_4 coefficient has been estimated [20, 23] to be $K_4 \approx 25 \pm 50$.

Assuming the validity of the QCD sum rule formalism, there are no local gauge invariant scalar operators proportional to $1/m_\tau^2$, so the only corrections which contribute at dimension $D = 2$ are due to the leading light quark (u, d, s) masses; $m_i(\mu)m_j(\mu)$. These corrections have been estimated to be $\delta^{(2)} = -0.010 \pm 0.002$ [24, 25].

The non-perturbative corrections are small due to a cancellation of the vector and axial-vector contributions. At dimension $D = 4$ the operators are the (scale invariant) quark and gluon condensates $\langle m_j\bar{\psi}_i\psi_i\rangle$ and $\langle(\alpha_s/\pi)GG\rangle$, while the $D = 6$ corrections are mainly due to four-quark operators. Contributions from dimension $D \geq 8$ condensates are expected to be negligible. The non-perturbative corrections have been estimated [19, 24] to total $\delta^{(D\geq 4)} = -0.010 \pm 0.004$ and are listed in table 2.2. Recent experimental measurements of the moments of the τ hadronic spectral functions have confirmed the approximate sizes of these contributions [26, 27]. The dominant uncertainty in the non-perturbative contribution is from the dimension $D = 6$ condensates.

From an experimental point of view, R_τ can be extracted from a direct or indirect measurement of the inclusive τ hadronic decay width. Using the complete-

Dimension	$\delta^{(D)}$
$D = 2$ (quark mass)	-0.010 ± 0.002
$D = 4$	-0.0033 ± 0.0005
$D = 6$	-0.007 ± 0.004
$D = 8$	≈ 0.00001

Table 2.2: Estimates of the quark mass and non-perturbative contributions to R_τ

ness of the τ decay width, the inclusive τ hadronic branching ratio can be written $\mathrm{B}(\tau^- \to \text{hadrons } \nu_\tau) = 1 - \mathrm{B}(\tau^- \to \mathrm{e}^-\bar{\nu}_\mathrm{e}\nu_\tau) - \mathrm{B}(\tau^- \to \mu^-\bar{\nu}_\mu\nu_\tau)$, permitting R_τ to be expressed in terms of the leptonic branching ratios only:

$$R_\tau = \frac{1 - \mathrm{B}(\tau^- \to \mathrm{e}^-\bar{\nu}_\mathrm{e}\nu_\tau) - \mathrm{B}(\tau^- \to \mu^-\bar{\nu}_\mu\nu_\tau)}{\mathrm{B}(\tau^- \to \mathrm{e}^-\bar{\nu}_\mathrm{e}\nu_\tau)} \quad . \tag{2.21}$$

Universality of charged-current couplings implies that the branching ratios are related by $\mathrm{B}(\tau^- \to \mathrm{e}^-\bar{\nu}_\mathrm{e}\nu_\tau) = f(x) \cdot \mathrm{B}(\tau^- \to \mu^-\bar{\nu}_\mu\nu_\tau)$ where $f(x)$ is the mass correction factor given in equation 2.6. Substituting into equation 2.21 gives R_τ in terms of the τ electronic branching ratio:

$$R_\tau = \frac{1 - 1.9726 \cdot \mathrm{B}(\tau^- \to \mathrm{e}^-\bar{\nu}_\mathrm{e}\nu_\tau)}{\mathrm{B}(\tau^- \to \mathrm{e}^-\bar{\nu}_\mathrm{e}\nu_\tau)} \quad . \tag{2.22}$$

An experimental measurement of $\mathrm{B}(\tau^- \to \mathrm{e}^-\bar{\nu}_\mathrm{e}\nu_\tau)$ can therefore be used to determine α_s at the τ mass scale. This result can then be evolved up to the Z^0 mass scale using renormalization group evolution, to give a value of $\alpha_s(m_\mathrm{Z}^2)$. Details of the evolution procedure are given in Appendix B. During the evolution process, the total uncertainty on $\alpha_s(\mu^2)$ at $q^2 = \mu^2$ scales roughly as ${\alpha_s}^2$, and therefore decreases as the energy scale increases. As a result, a measurement of $\alpha_s(m_\tau^2)$ of modest precision produces a precise determination of $\alpha_s(m_\mathrm{Z}^2)$.

Chapter 3

Experimental environment

The CERN laboratory, located near Geneva Switzerland, is the home of the Large Electron Positron (LEP) [28] collider. Between 1989 and 1995, the LEP collider produced collisions between electron (e^-) and positron (e^+) beams at centre-of-mass energies close to the Z^0 mass (approximately 45 GeV per beam). This permitted Z^0 bosons to be produced essentially at rest with respect to the laboratory reference frame [29]. During this period, approximately 5.1 million Z^0 decays to multihadronic final states were recorded by the OPAL experiment, corresponding to a total integrated luminosity of 173 pb^{-1}. This chapter describes the LEP collider, the OPAL detector and event reconstruction system, and finally the offline analysis tools which were used to produce this work.

3.1 The LEP Collider

The LEP collider is an e^+e^- storage ring with a circumference of approximately 27 km, and is contained in a tunnel located between 100 m and 150 m underground. The ring is composed of eight piecewise circular arcs which connect the eight underground areas where the two counter-rotating beams can be collided. Four of these areas are occupied by general purpose LEP detectors (ALEPH, DELPHI, OPAL and L3) as

shown in figure 3.1. Each arc consists of 31 "standard cells" composed of a sequence of bending dipole magnets, which provide horizontal deflection of the beams, focusing and defocusing quadrapole and sextupole magnets, and horizontal and vertical beam orbit correctors. Superconducting quadrapole magnets positioned near the four experimental areas focus the beam to very small dimensions (10 μm $\times$ 250 μm in the vertical and horizontal planes respectively) at the centre of the four detectors in order to provide a high *luminosity* $\mathcal{L}$ at these points. The rate R at which a physics process occurs is related to the luminosity by the expression $R = \sigma\mathcal{L}$, where σ is the *cross section* of the process of interest. LEP was designed to provide a peak luminosity of 1.6×10^{31} cm^{-2} s^{-1} at an average beam current of 3 mA, corresponding to the production of a Z^0 boson approximately every second.

Radio frequency (RF) copper cavities provide energy to the two beams, initially during the acceleration phase, and to compensate for synchrotron radiation losses once the operating energy has been reached. The 128 five-cell RF cavities are powered by 1 MW klystrons operating at a frequency of 352.21 MHz. This frequency corresponds to 31320 times the beam revolution frequency and hence there are 31320 RF "buckets" per beam into which particle bunches can potentially be injected. The LEP collider initially operated in 4×4 mode, with four equally spaced bunches per beam, giving the potential for collisions in each of eight interaction points. The beams were however prevented from colliding in the four non-instrumented areas by electrostatic separators. After 1992, LEP was upgraded to operate in 8×8 mode, with eight circulating bunches per beam.

The LEP injector chain [30] is shown schematically in figure 3.1. Positrons for LEP are produced by colliding an electron beam from a 200 MeV linac into a converter target. These positrons, along with electrons produced by an electron gun, are then

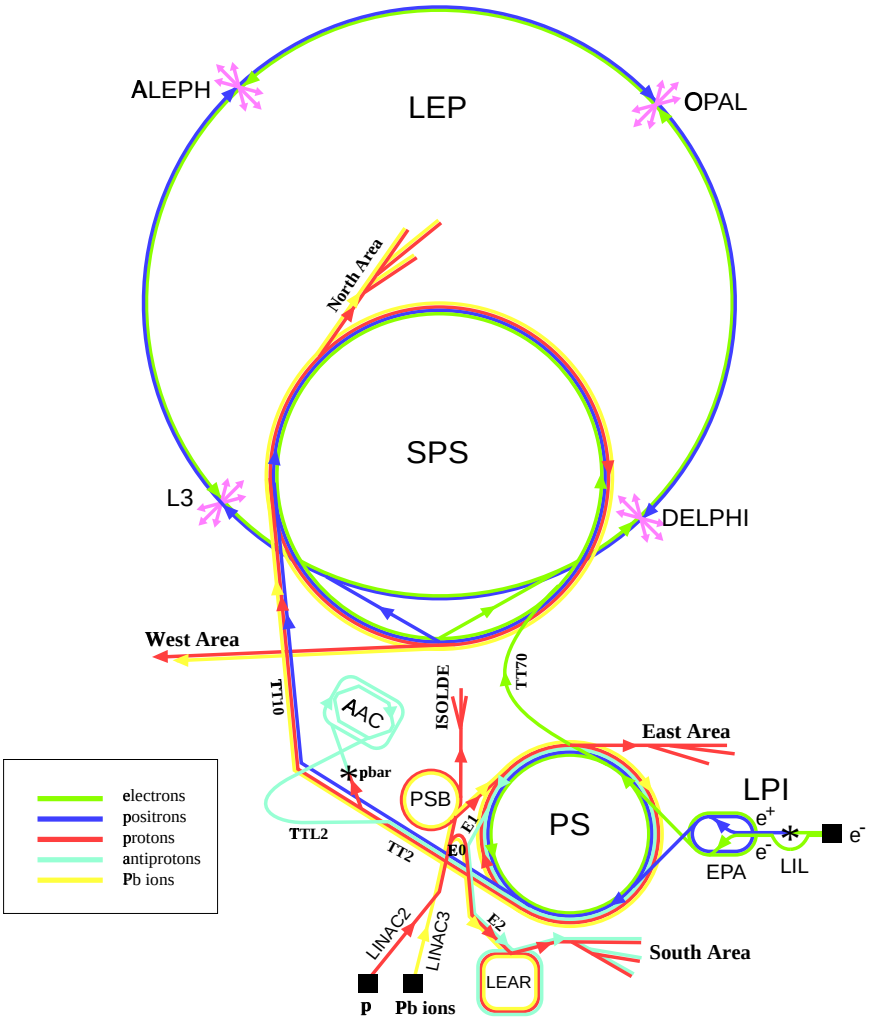

LEP: Large Electron Positron collider
SPS: Super Proton Synchrotron
AAC: Antiproton Accumulator Complex
ISOLDE: Isotope Separator OnLine DEvice
PSB: Proton Synchrotron Booster
PS: Proton Synchrotron

LPI: Lep Pre-Injector
EPA: Electron Positron Accumulator
LIL: Lep Injector Linac
LINAC: LINear ACcelerator
LEAR: Low Energy Antiproton Ring

Rudolf LEY, PS Division, CERN, 02.09.96

Figure 3.1: Schematic diagram of the CERN accelerator complex. The LEP injection chain is shown, as well as the accelerators used for proton/antiproton physics, and heavy ion physics.

accelerated to 600 MeV by a second linac (LIL) before being collected in the Electron-Positron Accumulator (EPA). The EPA stores pulses of electrons and positrons until the next injection cycle of the Proton Synchrotron (PS). Injection into the LEP ring proceeds via the PS and Super Proton Synchrotron (SPS), which accelerate the beams to 3.5 GeV and 20 GeV respectively. The PS and SPS operate in a multi-cycle mode which incorporates LEP injection cycles into the dead-time between proton cycles, thus permitting simultaneous production of e^+e^- and proton beams. Injection into the LEP collider occurs at 20 GeV, and the counter-rotating e^+ and e^- bunches are accelerated to $\sim$ 45 GeV per beam before being brought into collision at the four interaction points which house the four LEP experiments.

3.2 The OPAL Experiment

The OPAL experiment is one of four general purpose experiments for the LEP collider at CERN. It is designed to detect and identify all types of interactions resulting from e^+e^- collisions, and in particular to reconstruct Z^0 decays over the largest possible kinematic range and solid angle. The detector is constructed as a series of nested sub-detectors with a cylindrical geometry surrounding the interaction point and coaxial to the beam direction[1] as shown in figure 3.2. The "barrel" region provides coverage in the angular region $|\cos\theta| < 0.81$, while two circular "endcaps" extend this coverage down to $|\cos\theta| < 0.98$. Collisions between the counter-rotating e^+ and e^- beams occur within a thin-walled 10.7 cm diameter beryllium beam pipe. The products of these collisions travel outwards through the detector, depositing energy in successive subdetector layers until either they exit the detector or are stopped, depending on

[1] In the OPAL coordinate system the e^- beam direction defines the $+z$ axis, and the centre of the LEP ring defines the $+x$ axis. The polar angle θ is measured from the $+z$ axis, and the azimuthal angle ϕ is measured from the $+x$ axis

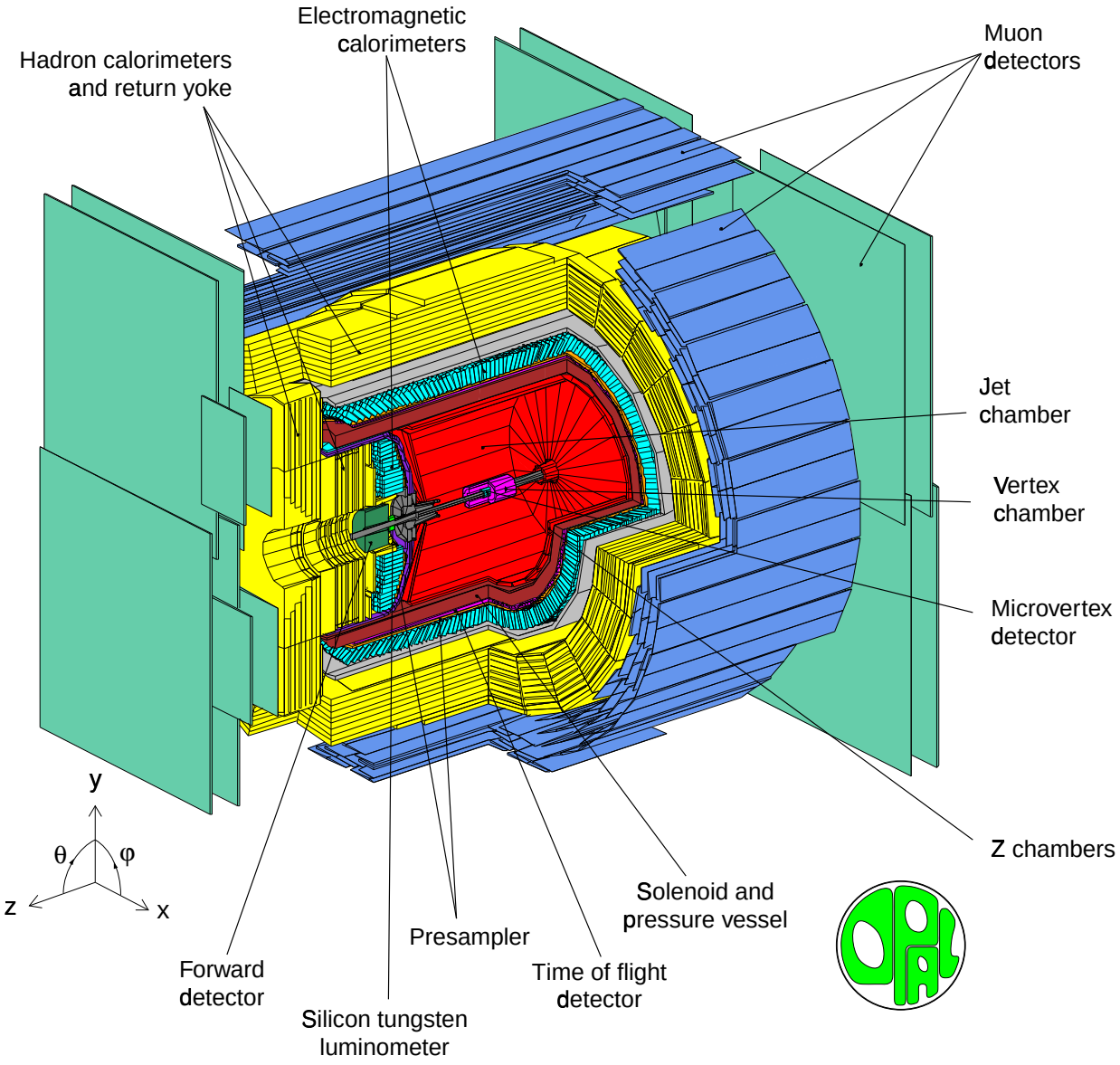

Figure 3.2: Cut-away view of the OPAL detector showing the various subdetector components which are described in the text. The OPAL coordinate system is indicated, and the electron (positron) beam enters the detector from the right (left). The detector dimensions are approximately $(12 \times 12 \times 12)$ m^3.

the particle species. A particle traveling outwards from the interaction point and within the barrel acceptance region first passes through a silicon microvertex detector (SI), followed by three "jet-chamber" type tracking detectors. These subdetectors record the position of charged particles as they traverse the detector volume. The tracking volume is enclosed inside a solenoid which provides a uniform magnetic field parallel to the beam axis. Charged particles traversing the tracking volume are deflected by this field so that the curvature of the resulting track can be used to determine the momentum of the incident particle. Outside of the solenoid is an electromagnetic calorimeter (ECAL), used to measure the energy of electrons, positrons and photons. Surrounding the ECAL is the magnetic flux return for the solenoid. The iron plates of the flux return double as converter material for the hadron calorimeter (HCAL), which is used in combination with the ECAL to determine the energy of hadrons. Any charged particle which manages to penetrate the full depth of the HCAL is presumed to be a muon, so the outer layer of the detector is instrumented with muon chambers designed to detect the passage of minimum ionizing particles. The OPAL subdetectors are described in detail in reference [31], and so only the subdetectors pertinent to this analysis are discussed in the following sections.

3.2.1 The central tracking detectors

The central tracking system consists of the silicon microvertex detector (SI), the central vertex detector (CV), the large-volume central jet chamber (CJ) and the z-chambers (CZ), which together provide a measurement of the track momentum, vertexing, and particle identification via ionization energy loss ($\mathrm{d}E/\mathrm{d}x$). These subdetectors are illustrated in figure 3.3, from which their locations and angular acceptance can be deduced.

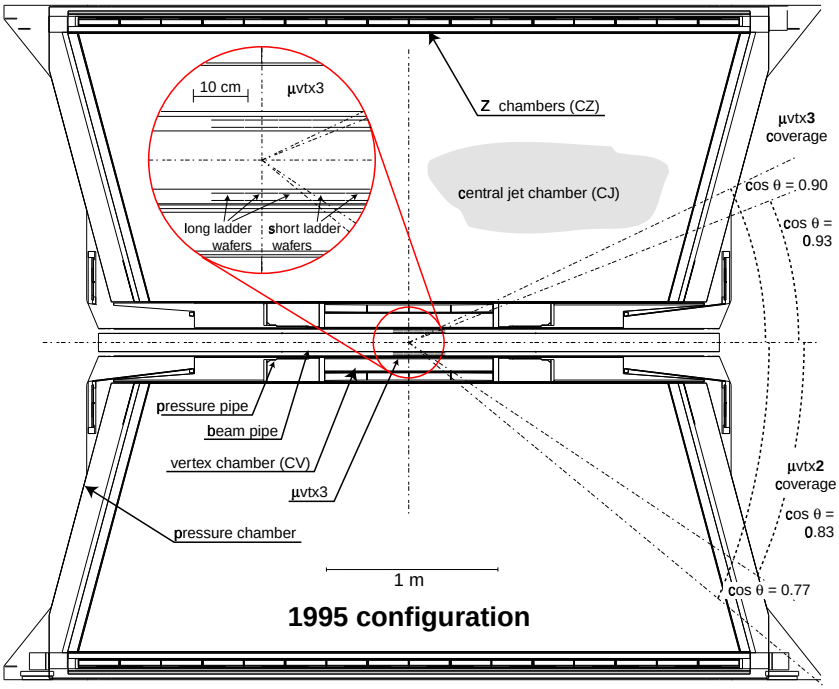

Figure 3.3: Schematic diagram of the OPAL central tracking system in the r-z plane. The relative size and location of the CV, CJ and CZ can be seen relative to the beam pipe and the pressure vessel. The angular coverage of the SI detector is shown for two different configurations labelled μvtx2 and μvtx3, used before and after 1995 respectively. The two LEP beams enter horizontally and collide at the centre of the detector.

The silicon microvertex (SI) detector [32] is used to provide a precise starting point for charged track reconstruction. This is necessary for a determination of the track momentum, and also to allow extrapolation of the track back towards the interaction point in order to identify secondary vertices resulting from the decay of short-lived particles produced in e^+e^- collisions. SI consists of two concentric cylinders each composed of multiple layers of silicon strip detectors. The two cylinders are each composed of "ladders" consisting of three sets of paired silicon wafers ganged together. One wafer from each pair is oriented to provide a measurement of the position in the ϕ direction and one oriented to provide a measurement of z. Eleven such

ladders are arranged azimuthally around the beam pipe to form the inner cylinder, and fourteen similar sets of wafers form the outer cylinder. A charged particle travelling outwards from the interaction region passes through successive layers of silicon dectector. At each layer, a signal is created on a single strip, allowing one coordinate of the particle position to be reconstructed at a known radius. The position resolution of the silicon microvertex detector is 10 μm in the ϕ direction and 15 μm in the z direction.

Three central tracking chambers operate within a common pressure vessel with a gas mixture of 88.2% argon, 9.8% methane and 2.0% isobutane maintained at a pressure of 4 bar. The outer wall of the pressure vessel provides structural support for a thin (96 mm) solenoid which produces a uniform magnetic field of 0.435 T within the central tracking system. The innermost of the tracking chambers is a 1 m long drift chamber called the central vertex detector (CV), which is designed to detect secondary vertices from the decay of short-lived particles. The CV consists of two concentric cylinders each subdivided azimuthally into 36 drift cells, and which together span the radius from 88 mm to 235 mm. Each cell of the inner cylinder contains 12 signal wires running axially, and alternating with potential wires to form a radial anode plane. The signal wires are staggered alternately ± 41 μm to either side of the anode plane to remove left-right ambiguities. The ϕ position is determined from the drift time, while a much less precise measurement of the z coordinate is obtained by comparing the time difference between the two ends of the signal wire. The outer cylinder is of similar design except that each cell contains only six signal wires, and these wires are inclined by 4° in ϕ from an axial orientation to produce "stereo" cells, permitting an improved determination of the z coordinate. The single hit resolution of the CV is 55 μm in ϕ and 1.0 mm in z.

The sensitive volume of CJ is a cylinder of length $\sim$ 4 m extending from an inner radius of 0.25 m to an outer radius of 1.85 m. The chamber is divided into 24 identical sectors each spanning 15° in ϕ, with cathode wire planes forming the boundary between sectors. All wires run parallel to the beam direction and wire planes are radial. A total of 159 signal wires alternating with potential wires define an anode plane in the centre of each sector. Signal wires are separated by from one another by 10 mm radially, and are alternately staggered to either side of the potential wire plane by ± 100 μm in order to resolve left-right ambiguities. Signal wires are held at ground potential, while the gas gain of $\sim 10^4$ is determined by the potential wire voltage of -2.38 kV. Ionization charge produced by the passage of a charged particle through the gas volume drifts under the influence of the electric field produced by the anode and cathode planes and is collected on the signal wires. Because the separation between the anode and cathode planes varies with radius from $\sim$ 3 cm to $\sim$ 25 cm, each cathode wire is maintained at a different potential.

The rate of energy loss due to ionization ($\mathrm{d}E/\mathrm{d}x$) by a charged particle traversing a medium is given by the Bethe-Bloch equation, and is a function of the particle mass and velocity. The $\mathrm{d}E/\mathrm{d}x$ associated with a track is obtained by combining the $\mathrm{d}E/\mathrm{d}x$ measurements from all CJ signal wires with isolated "hits", i.e. no overlap with adjacent tracks. The $\mathrm{d}E/\mathrm{d}x$ measurement resolution therefore improves as $\sim 1/\sqrt{n}$ where n is the number of signal wires used. The $\mathrm{d}E/\mathrm{d}x$ and $\mathrm{d}E/\mathrm{d}x$ resolution are plotted in figure 3.4. A simultaneous determination of $\mathrm{d}E/\mathrm{d}x$ and the track momentum can be used to separate particle species, as discussed further in section 5.1.5.

Surrounding CJ is third layer of jet chambers (CZ) which are used to provide a precise measurement of the z-coordinate of tracks leaving the jet chambers in order to improve the polar angle measurement. The z-chambers cover 94% of the azimuthal

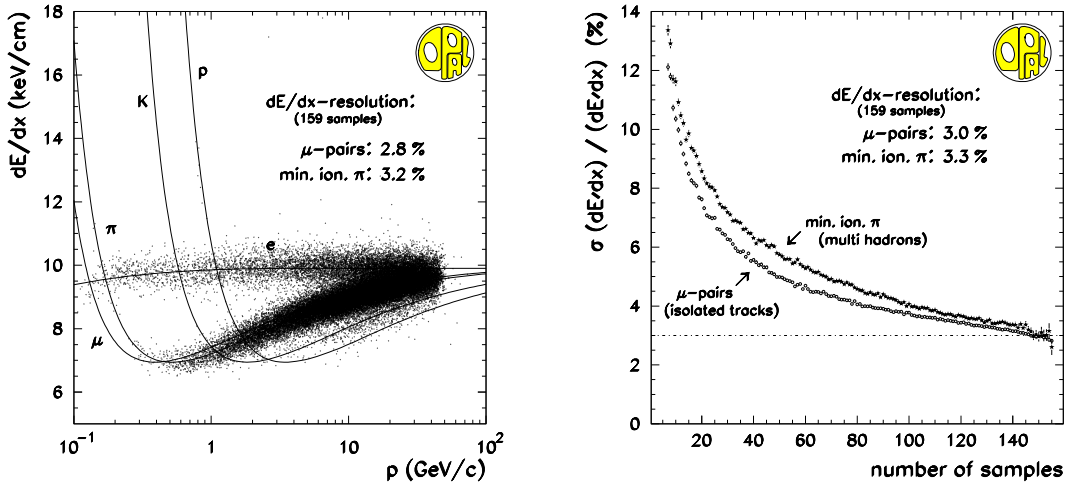

Figure 3.4: The value of $\mathrm{d}E/\mathrm{d}x$ obtained from CJ is plotted as a function of the track momentum for various particle species, along with the theoretical curves obtained from the Bethe-Bloch equation (left). The $\mathrm{d}E/\mathrm{d}x$ resolution of the CJ is plotted as a function of the number wire hits which are used for the $\mathrm{d}E/\mathrm{d}x$ measurement (right) for isolated ($\mu^{\pm}$) tracks and for tracks in a multihadron environment.

angle in the region $|\cos\theta| < 0.72$, and consist of 24 drift chambers of thickness 59 mm and length 4 m. Each chamber is divided into eight cells in z, with wire planes oriented in the r-ϕ direction. The z-position is determined from charge drift time, and has an overall resolution of approximately 300 μm.

The combined position resolution of the central tracking chambers in θ and ϕ are 1.4 mrad and 0.29 mrad respectively. The momentum resolution for charged tracks has been estimated to be $\sigma_p/p^2 = 1.3 \times 10^{-3}$ GeV^{-1} [33].

3.2.2 The time of flight detector

Surrounding the solenoid is a cylindrical array of 160 scintillation counters called the time of flight (TOF) detector. The 6.84 m long scintillators are oriented parallel to the beam axis and scintillation light produced by the passage of charged particles is

read out from both ends. A timing resolution of 360 ps is achieved, allowing the TOF detector to be used for cosmic ray rejection and as a trigger veto for events which are not synchronous with LEP bunch crossings.

3.2.3 The electromagnetic and hadron calorimeters

The barrel electromagnetic calorimeter (EB) is located outside the magnet coil at a radius of 2455 mm, and covers the region $|\cos\theta| < 0.82$. It consists of a cylindrical array of 9440 lead glass blocks with a total thickness of $24.6X_0$.[2] The angular coverage is extended into the region $0.81 < |\cos\theta| < 0.98$ by two endcap calorimeters (EE) of a design similar to the EB. The EB is segmented equally into 59 blocks in the z direction, and 160 blocks in the ϕ direction. Each block is 37 cm long and has dimensions 10×10 cm^2 at the front face, corresponding to an angular coverage of approximately 40×40 mrad^2. The lead glass blocks are oriented so that they point towards the interaction region in order to minimize the probability of a particle traversing more than one block. However, the blocks are tilted slightly from a perfectly pointing geometry to prevent particles from escaping through gaps between the blocks. The orientation of the lead glass blocks and their location relative to other subdetector components is shown in figure 3.5. Energetic charged particles and photons entering the ECAL produce a shower of secondary particles through the processes of bremsstrahlung and pair-production. Charged particles within this shower will produce photons of Čerenkov radiation if their velocity exceeds the speed of light in the medium, given by c/n where c is the speed of light in a vacuum, and $n \simeq 1.847$ is the index of refraction of the lead glass blocks. Čerenkov photons produced by

[2] A *radiation length* X_0 is defined as the average thickness of material that an electron must traverse in order to decrease its energy to a fraction $1/e$ (33.8%) of its original energy by radiation of bremsstrahlung photons. A *conversion length* l_γ is defined as the mean free path of a photon traversing the medium, and is given approximately by $l_\gamma = 9X_0/7$.

charged particles within the electromagnetic shower are detected by photomultiplier tubes located behind the calorimeter, producing a signal proportional to the energy of the incident particle. The lead glass calorimeter has an intrinsic energy resolution of $\sigma_E/E = 0.2\% + 6.3\%/\sqrt{E}$ where E is in GeV, however this resolution is degraded by the approximately $2X_0$ of material in front of the EB, primarily the pressure vessel and the solenoid, which usually initiate early showering.

To compensate for this effect, an electromagnetic presampler is incorporated between the TOF and the EB. The barrel presampler (PB) is a cylinder composed of sixteen wire chambers of length 6623 mm operating in limited streamer mode. Each chamber consists of two layers of limited streamer mode tubes oriented with the wires running axially, and containing a gas mixture of 32% n-pentane and 68% CO_2. The two layers each possess 24 cells, with the two layers offset by half a cell to avoid inefficiencies associated with the cell edges. Readout is obtained from 1 cm wide cathode strips on the top and bottom surface of each layer of tubes. The strips are oriented at 45° to the wire direction, and the strips on the upper and lower surfaces are perpendicular to one another to give complete θ - ϕ information. The position resolution for electromagnetic showers is typically 4 - 6 mm. The effective energy resolution of the ECAL has been estimated to be $\sigma_E/E = 1.8\% + 23\%/\sqrt{E}$ [34].

The hadron calorimeter is located behind the ECAL and is used to measure energy deposited by hadronic showers as well as to aid in the identification of muons. The iron of the magnetic flux return provides over four interaction lengths[3] of absorber material over 97% of the full solid angle. By interleaving active detector elements with these iron slabs, a sampling hadron calorimeter is constructed. The barrel hadron

[3]An *interaction length* $\lambda_{\rm int}$ is defined as the mean free path of a particle traversing a medium before experiencing a nuclear interaction.

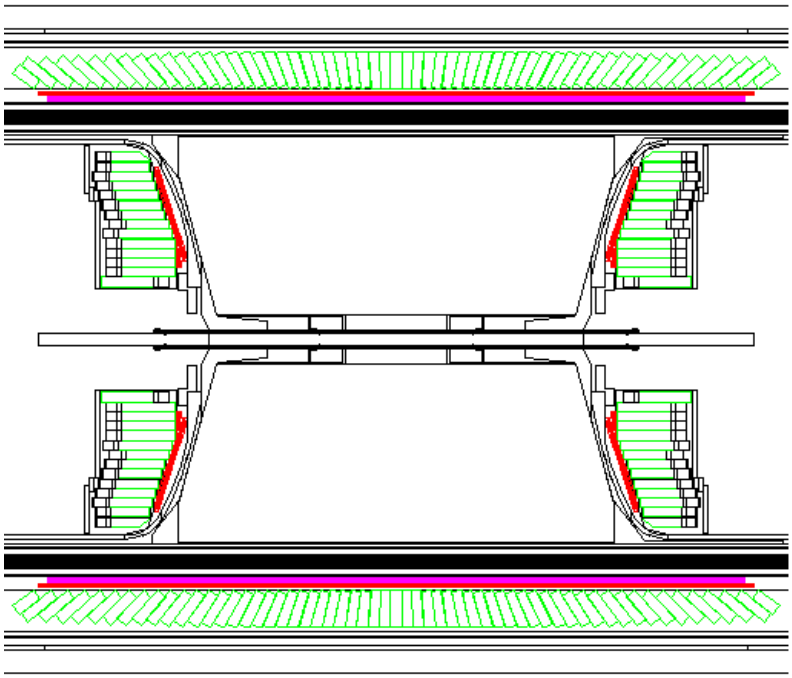

Figure 3.5: Schematic diagram of the barrel and endcap electromagnetic calorimeters. The lead glass blocks of the EB are oriented towards the interaction region and lie immediately behind the presampler (darker grey), TOF (ligher grey) and the magnet coil (black).

calorimeter (HB) covers the angular region $|\cos\theta| < 0.81$, and consists of nine 2.5 cm thick layers of limited-streamer tube chambers alternating with eight 10 cm thick slabs of iron. Because the EB contains an additional 2.2 interaction lengths of material in front of the HB, the energy of hadronic showers must be determined by combining the energy deposition in the EB and HB. The energy resolution for hadronic showers has been estimated to be $\sigma_E/E = 20\% + 63\%/\sqrt{E}$ [35].

3.2.4 The muon chambers

Particles which successfully penetrate the ~ 6 interaction lengths of material of the calorimeters are presumed to be muons. Identification of these muons is achieved by

matching tracks in the inner detector with hits in a multilayer array of large area drift chambers surrounding the HCAL. Approximately 93% of the full solid angle is covered by at least one layer of muon detectors, and within this coverage, the efficiency for detecting isolated muons is essentially 100% for muons with greater than 3 GeV momenta. Within the barrel region of the OPAL detector, the muon detector (MB) consists of 110 large-area drift chambers arranged in four overlapping layers. The spatial resolution of the muon chamber matching with inner detector tracks is approximately 1.5 mm (2 mm) in the ϕ (z) direction.

3.3 Event reconstruction and offline analysis

Particle physics reactions resulting from e^+e^- collisions are identified using a fast, programmable trigger which is synchronized to the LEP bunch crossing frequency. The trigger is designed to have an efficiency approaching 100% for a variety of different physics processes, and in particular it selects all τ decay channels with uniform efficiency. It uses fast information from individual subdetectors to distinguish interesting events from background signals due to noise, cosmic rays, or interactions between beam particles and the beam pipe, or gas within the beam pipe. During normal LEP running, the trigger rate is typically 1-5 Hz, compared to the 45 kHz LEP bunch crossing rate. Raw subdetector information from a triggered event is passed to the *event builder* and *filter* which arrange this information into a single data structure and classify the event into specified types, permitting further online background rejection. Selected events are passed to the online event reconstruction system (ROPE) which performs complete reconstruction of the event using the most up-to-date detector calibrations, and archives the event to optical disk and magnetic tape.

The ROPE system is also used to perform offline event reconstruction ("reROPE") in order to apply new subdetector calibration information or improved event reconstruction algorithms to previously recorded data. The data set used in the present analysis uses a consistent set of calibrations and code, and is based on the PASS 7 or "Grand" reROPE.

Offline analysis of the reconstructed events was performed at the University of Victoria on the High Energy Physics group local area network. This network consists of approximately ten Hewlett Packard UNIX workstations. Analysis code is written in HP-UX FORTRAN 77, and uses standard OPAL and CERN libraries.

3.4 The OPAL data set and event simulation

From 1991 to 1995, the LEP collider operated at centre-of-mass energies close to the Z^0 mass. During this period, the OPAL experiment collected data corresponding to approximately 173 pb^{-1} of integrated luminosity. Approximately 89.7% of the τ-pairs data used in this analysis were collected at the Z^0 peak ($\sim$ 91 GeV), with the remainder collected approximately 2 GeV above (4.4%) and below (5.9%) the Z^0 peak.

Predictions of the distributions of physics quantities used in the analysis of the data are obtained using full detector simulations, based on the Monte Carlo (MC) method, of all e^+e^- processes discussed in this work. The MC generators used to create the four-vectors for these processes are summarized in table 3.1 along with the effective luminosity of each MC sample. These simulated events were then passed through a GEANT [43] simulation of the OPAL detector [44], which created a data structure equivalent to that used with real OPAL events. The simulated events are then processed offline in a manner identical to real data. Comparisons between MC

Source	MC run	Generator	Luminosity (pb^{-1})
$e^+e^- \to \tau^+\tau^-$	1536	KORALZ 4.02 [36]	253.1
	1535 (peak−2 GeV)	KORALZ 4.02	142.0
	1537 (peak+2 GeV)	KORALZ 4.02	138.6
$e^+e^- \to \mu^+\mu^-$	1620	KORALZ 4.0	404.3
	1636	KORALZ 4.02	253.1
$e^+e^- \to e^+e^-$	1320	BABAMC [37]	151
	1335	BHWIDE [38]	72.2
$e^+e^- \to q\bar{q}$	2790 - 2793	JETSET [39]	121.6
	2291 - 2292	JETSET	60.8
$e^+e^- \to (e^+e^-)\tau^+\tau^-$	1744	VERMASEREN [40]	678.0
$e^+e^- \to (e^+e^-)\mu^+\mu^-$	1716	VERMASEREN	461.7
	1745	VERMASEREN	456.0
$e^+e^- \to (e^+e^-)e^+e^-$	1717	VERMASEREN	392.5
	1746	VERMASEREN	392.5
$Z^0e^+e^-$	6613	GRC4F [41]	500
four fermion	6503 - 6511	FERMISV [42]	1000

Table 3.1: Principal Monte Carlo samples which are used in this analysis to model τ decays and non-τ backgrounds in the τ event sample.

and data of the distributions of physics quantities are used to ensure the accuracy of MC modeling, and corrections are applied to the MC distributions where appropriate. These corrections are discussed in the following chapters.

Tau decays were simulated using the τ-pair Monte Carlo run 1536 (375 000 events). Four-vectors for the simulated τ-pair events were generated using KORALZ 4.02 [36] and then decayed using the TAUOLA 2.0 library [45]. The off-peak τ-pair Monte Carlo runs 1535 and 1537 were added to this sample, scaled in proportion to the amount of off-peak data.

Chapter 4

The τ candidate sample

Candidate τ events used in this analysis are selected from the OPAL LEP1 data set using a procedure similar to that presented in previous OPAL publications [46]. The selection crtieria are described in section 4.1 and are summarized in table 4.1. This procedure does not have a uniform selection efficiency for all τ decay channels and the bias introduced to the branching ratio measurement by this selection is described in section 4.2. Residual backgrounds in the τ candidate sample from non-τ sources are discussed in section 4.3.

4.1 Selection of τ jets

At LEP, Z^0 bosons decaying at rest in the laboratory frame produce back-to-back τ pairs. Each highly relativistic τ subsequently decays in flight, via the charged-current weak interaction, producing strongly collimated jets. Events selected as $\tau^+\tau^-$ are required to have exactly two such jets, each with at least one charged track, identified using a cone algorithm [47]. Jets are initially defined in a cone of half-angle 35° centred on the highest energy track or cluster. The next-highest energy track or cluster within the jet-cone is then added and the jet direction is redefined in terms of the combination of the two tracks or clusters. This process continues until all good

tracks and clusters within the jet-cone have been included. Definitions of "good" tracks and clusters can be found in [46]. The average $|\cos\theta|$ of the two jets is required to be in the barrel region ($\overline{|\cos\theta|} < 0.68$) of the OPAL detector in order to to minimize detector-related systematic uncertainties associated with the endcap region and with the overlap region between the barrel and endcaps. The scalar sum of the momenta of good tracks, $p_{\rm tot}$, and the sum of the energies of good electromagnetic calorimeter (ECAL) clusters, $E_{\rm tot}$, are required to satisfy $E_{\rm vis} \equiv E_{\rm tot} + p_{\rm tot} > 0.01 \cdot E_{\rm cm}$, where $E_{\rm cm}$ is the centre-of-mass energy, in order to be considered a good event.

The background from cosmic rays is reduced to a negligible level by imposing requirements on the time-of-flight detector and on the distance of closest approach of charged tracks to the nominal interaction point in the r - ϕ plane ($|d_0|_{\rm min}$) and in z direction ($|z_0|_{\rm min}$). Two-photon mediated four-fermion events, $e^+e^- \rightarrow (e^+e^-)l^+l^-$ where l^+l^- represents lepton pairs, are rejected by requirements on the acollinearity angle $\theta_{\rm acol}$, defined as the supplement of the angle between the two jets, and on the total energy and momentum of tracks and clusters in the event.

Decays of Z^0 bosons into lepton pairs are distinguished from multihadronic events by requiring low multiplicities of tracks and ECAL clusters in the event. Selected τ-pair candidates are required to possess between two and six tracks, and no more than ten ECAL clusters in the event. Events within this low multiplicity sample are assumed to be lepton pairs, and are classified as e^+e^-, $\mu^+\mu^-$ or $\tau^+\tau^-$ based on tracking, calorimetry and muon chamber information.

Bhabha events typically possess two high-momentum tracks and ECAL energy deposition close to the full centre-of-mass energy. Bhabha events are removed from the τ candidate sample by rejecting events with either $E_{\rm tot} + 0.3 \cdot p_{\rm tot} > E_{\rm cm}$ or $E_{\rm vis} > 1.4 \cdot E_{\rm cm}$. It should be noted that this cut differs from the "standard" OPAL

τ-pairs selection cut, and was introduced in order to reduce the systematic uncertainty due to modelling of the Bhabha background as discussed in section 4.3.2.

Muon-pair events ($e^+e^- \to \mu^+\mu^-$) are characterized by two back-to-back high momentum tracks associated with activity in the muon chambers or hadron calorimeter and with little energy deposition in the ECAL. Events with $E_{\rm vis} > 0.6 \cdot E_{\rm cm}$ in combination with a tagged muon in both jets are rejected from the τ-pairs sample. Muon-pair events which survive this cut generally do so because one of the muons has passed through a region of the detector which lacks muon chamber coverage.

Fiducial cuts are imposed on the individual τ candidate jets to avoid regions of the detector associated with small gaps between structural units of the ECAL and to reject tracks which are close to the anode planes of the central jet chamber. Particles associated with these detector regions possess degraded ECAL energy and track momentum resolution respectively, resulting in a reduced ability to distinguish $\tau^- \to e^-\bar{\nu}_e\nu_\tau$ decays from other τ decays. These requirements are summarized below.

4.1.1 EM calorimeter crack regions

Jet cones are rejected from the τ sample if the primary track[1] points to any of the following regions of the EB:

- $1.555 < \phi < 1.575$
- $4.695 < \phi < 4.725$
- $0.213 < |\cos\theta| < 0.216$
- $0.596 < |\cos\theta| < 0.598$

[1] In jet-cones possessing more than one charged track, the track with the highest momentum is taken to be the $\tau^- \to e^-\bar{\nu}_e\nu_\tau$ candidate electron, and is referred to as the *primary track*. Any additional tracks in the jet are ordered by decreasing track momentum.

Selection	Cut value	Description
Good event	$N_{\rm jet} = 2$ $E_{\rm jet} \geq 0.01 E_{\rm beam}$ $\overline{\lvert\cos\theta\rvert} < 0.68$	Number of good jets. Energy of tracks and clusters; $E_{\rm jet} \equiv \sum_{\rm jet} p + \sum_{\rm jet} E$. Average $\lvert\cos\theta\rvert$ of jets.
Cosmic ray rejection	$\lvert d_0\rvert_{\rm min} \leq 0.5$ cm $\lvert z_0\rvert_{\rm min} \leq 20.0$ cm $\lvert z_0\rvert_{\rm average} \leq 20.0$ cm $\lvert t_{\rm meas} - t_{\rm exp}\rvert \leq 10$ ns $\lvert t_{\rm i} - t_{\rm j}\rvert < 10$ ns	Minimum $\lvert d_0\rvert$ for all tracks. Minimum $\lvert z_0\rvert$ for all tracks. Average $\lvert z_0\rvert$ of all tracks. for at least one TOF counter. for some TOF counters i and j with $\lvert\phi_i - \phi_j\rvert \geq 165^\circ$
Two photon rejection	$\theta_{\rm acol} \leq 15^\circ$ $\sum_{\rm jets} {\rm MAX}(E,p) \geq 0.03 \cdot E_{\rm cm}$ $\sum E > 2.0$ GeV or $\sum p > 2.0$ GeV	Acolinearity of jets. Sum of highest energy track or cluster in each jet. For events with; $\sum_{\rm jets} {\rm MAX}(E,p) \leq 0.2 E_{\rm cm}$
$e^+e^- \to q\bar{q}$ rejection	$1 < N_{\rm tracks} \leq 6$ $N_{\rm clus} \leq 10$	Number of good tracks. Number of good clusters.
$e^+e^- \to e^+e^-$ rejection	$\sum E + \sum p \leq 1.4 \cdot E_{\rm cm}$ or $\sum E + 0.3 \cdot \sum p \leq E_{\rm cm}$	$E_{\rm cm} \equiv 2 \cdot E_{\rm beam}$
$e^+e^- \to \mu^+\mu^-$ rejection	$\sum E + \sum p \leq 0.6 \cdot E_{\rm cm}$ Muon tag requires at least one of: $N^{\rm MB}_{\rm layers} \geq 2$; $E < 2.0$ GeV ; $N^{\rm HC}_{\rm layers} \geq 4$, $N^{\rm HC}_{\rm hits/layer} < 2$ and $N^{\rm HC}_{\rm last3} \geq 1$	if both jets have tagged muons. Number of hits in MB. Associated EM cluster energy. Number of HCAL hit layers, average hits per layer, and number of hits in outer layers.

Table 4.1: Selection of τ candidate events.

4.1.2 Anode plane regions

High-momentum tracks passing close to CJ anode planes may have their momentum incorrectly reconstructed, leading to degraded resolution at high momentum. This effect is poorly modelled by the MC simulations, and contributes to systematic uncertainties in the efficiency of the $\tau^- \to e^- \bar{\nu}_e \nu_\tau$ selection. Incorrect momentum reconstruction at high momentum also leads to a significant excess of $e^+e^- \to \mu^+\mu^-$ background entering the τ-pair sample near the CJ anode planes. These events survive the τ selection cuts and are incorrectly identified as double $\tau^- \to \mu^- \bar{\nu}_\mu \nu_\tau$ decays because they possess $E_{\rm vis}/E_{\rm cm} < 0.6 E_{\rm cm}$. The quantity $\phi_{\rm sector}$ measures the position of a track relative to the nearest CJ anode plane. It is defined as the ϕ position of a track at a radial distance corresponding to the front face of the EB, modulo 15° and shifted so that the anode plane lies at 0°, then weighted by the charge q of the track: $\phi_{\rm sector} = q \cdot (\mathrm{mod}(\phi_{\rm track}, 15°) - 7.5°)$. This quantity is plotted in figure 4.1 for a sample of events enhanced in double $\tau^- \to \mu^- \bar{\nu}_\mu \nu_\tau$ decays and a clear excess of $e^+e^- \to \mu^+\mu^-$ background is visible near the anode plane region. To avoid the problems described above, jet cones in which the primary track passes near the CJ anode plane region are excluded from the τ-sample. Tracks crossing the anode plane curve towards negative values of $\phi_{\rm sector}$ and so an asymmetric cut is applied to this quantity. Jet cones in which the primary track lies in the interval $-0.65 < \phi_{\rm sector} < 0.1$ are excluded from the τ candidate sample, resulting in a geometrical efficiency loss of 5%.

4.2 The τ selection bias factor

The τ selection does not affect all τ decay channels equally, and therefore introduces a bias into measured value of $B(\tau^- \to e^- \bar{\nu}_e \nu_\tau)$. The τ selection bias factor F_B measures

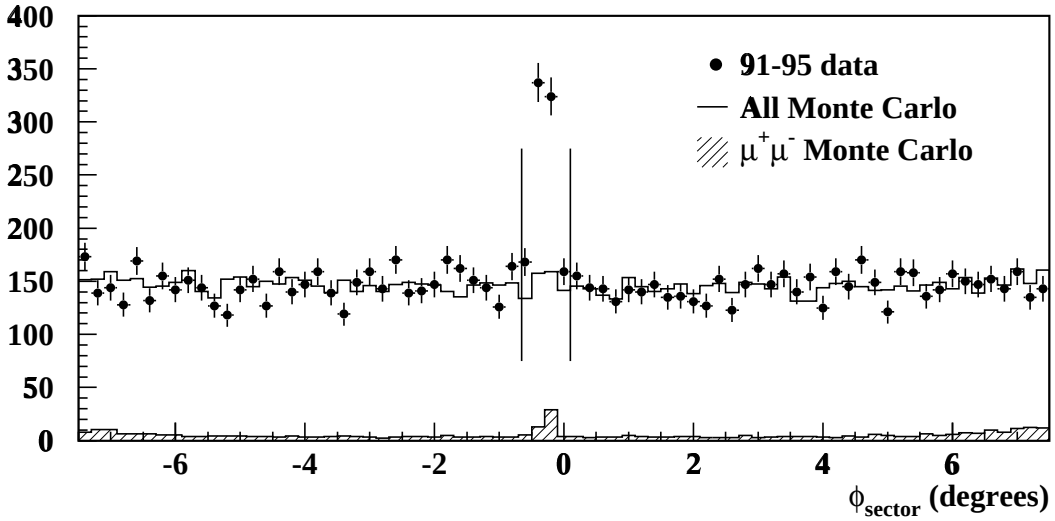

Figure 4.1: $\phi_{\rm sector}$ for τ-pair events possessing exactly one track in each jet and $E_{\rm tot} < 5$ GeV. The excess of $e^+e^- \to \mu^+\mu^-$ background near the CJ anode plane regions ($\phi_{\rm sector}$=0) is significantly underestimated by the $e^+e^- \to \mu^+\mu^-$ MC. The region between the two vertical lines is rejected by the anode plane cut.

the degree to which the τ selection favours or suppresses the decay $\tau^- \to e^-\bar{\nu}_e\nu_\tau$ relative to other τ decay channels. It is defined as the ratio of the fraction of $\tau^- \to e^-\bar{\nu}_e\nu_\tau$ decays in a sample of τ decays after the τ selection is applied to the fraction before the selection:

$$F_{\rm B} = \frac{{\rm B}(\tau^- \to e^-\bar{\nu}_e\nu_\tau)^{\rm after}}{{\rm B}(\tau^- \to e^-\bar{\nu}_e\nu_\tau)^{\rm before}} \tag{4.1}$$

where the two branching ratios are given by

$${\rm B}(\tau^- \to e^-\bar{\nu}_e\nu_\tau)^{\rm after} = \frac{N^{\rm after}_{\tau\to e\nu\bar{\nu}}}{N^{\rm after}_\tau} \quad , \quad {\rm B}(\tau^- \to e^-\bar{\nu}_e\nu_\tau)^{\rm before} = \frac{N^{\rm before}_{\tau\to e\nu\bar{\nu}}}{N^{\rm before}_\tau} \quad . \tag{4.2}$$

$N^{\rm before}_\tau$ and $N^{\rm after}_\tau$ are the number of τ events before and after the τ-selection, and $N^{\rm before}_{\tau\to e\nu\bar{\nu}}$ and $N^{\rm after}_{\tau\to e\nu\bar{\nu}}$ are the number of $\tau^- \to e^-\bar{\nu}_e\nu_\tau$ decays in the respective τ samples.

The $\tau^- \to e^-\bar{\nu}_e\nu_\tau$ bias factor was estimated individually from each of the τ MC runs 1513, 1520 and 1536 and the bias factor estimates obtained from each of these

simulations were found to be consistent within the available statistics. The results from these simulations were then combined with the two off peak simulations 1515 and 1516, weighted according to the proportion of off-peak data collected during LEP1 running, to obtain an improved estimate of F_{B}. Table 4.2 lists the estimated F_{B} for each of these simulations, using the selection desribed in section 4.1

The statistical uncertainty in F_{B} can be estimated by taking the quadratic sum of the binomial errors on $\mathrm{B}(\tau^- \to \mathrm{e}^-\bar{\nu}_{\mathrm{e}}\nu_\tau)^{\mathrm{before}}$ and $\mathrm{B}(\tau^- \to \mathrm{e}^-\bar{\nu}_{\mathrm{e}}\nu_\tau)^{\mathrm{after}}$ from equation 4.1, this neglects the statistical correlation between these two quantities. In practice, a better estimate is obtained by redefining F_{B} in terms of the ratio of the τ selection efficiencies ϵ_{e} and ϵ_τ for selecting $\tau^- \to \mathrm{e}^-\bar{\nu}_{\mathrm{e}}\nu_\tau$ decays and $\tau \to$ anything ν_τ respectively,

$$F_{\mathrm{B}} = \frac{(N^{\mathrm{after}}_{\tau\to \mathrm{e}\nu\bar{\nu}}/N^{\mathrm{before}}_{\tau\to \mathrm{e}\nu\bar{\nu}})}{(N^{\mathrm{after}}_{\tau}/N^{\mathrm{before}}_{\tau})} = \frac{\epsilon_e}{\epsilon_\tau} \tag{4.3}$$

then computing the binomial errors as before. The τ selection efficiency is approximately 54%, with the $\overline{|\cos\theta|}$ requirement imposing the majority of the efficiency loss. This expression still overestimates the true statistical uncertainty since the covariance of ϵ_e and ϵ_τ is neglected. For the combined MC τ-pair sample described above, this method provides an upper bound on the statistical uncertainty of ± 0.0017.

The covariance of ϵ_e and ϵ_τ is purely statistical in nature and does not depend on the details of the τ MC simulation. It was therefore estimated by generating random samples of "τ decays" using a simplified MC procedure, and applying a random selection with efficiency equal to nominal τ selection efficiency. Each sample consisted of between 1×10^2 and 3×10^6 events, with each event labelled as either signal (i.e. a $\tau^- \to \mathrm{e}^-\bar{\nu}_{\mathrm{e}}\nu_\tau$ decay) or background (i.e. not a $\tau^- \to \mathrm{e}^-\bar{\nu}_{\mathrm{e}}\nu_\tau$ decay) with a probability approximating the expected branching ratio. Several hundred samples of each size were generated and the bias factor was determined for each sample. Due to

the nature of the simplified simulation the bias factor is expected to be unity for each sample, but the actual measured value is subject to statistical fluctuations equivalent to those in the full MC sample. The statistical uncertainty in the bias factor estimate including the covariance was then determined as a function of the sample size by measuring the width of the distribution of "bias factor" estimates obtained for each size of sample. For a sample of size equal to that of the full MC simulation discussed above, the expected bias factor statistical uncertainty was estimated to be ± 0.0014.

Systematic uncertainties on F_{B} were evaluated for several potential sources. The uncertainty introduced by the inclusion of the off-peak τ MC run 1515 and 1516, and by the EM calorimeter energy scale uncertainty (at the $\pm 1\%$ level) were found to be negligible compared with the statistical uncertainty. The largest single contribution to the τ-selection inefficiency is due to the $\overline{|\cos\theta|} < 0.68$ (barrel) requirement. The distribution of the reconstructed jet-cone thrust axis was varied by modifying the cone-finding algorithm to exclude either tracks or clusters from the thrust axis reconstruction. This tested the bias factor sensitivity to the modelling of the barrel cut and was found to have a negligible effect. Systematic uncertainties introduced by other τ selection cuts were estimated by comparing data and MC distributions of τ selection variables such as track and ECAL cluster multiplicities. MC variables were then smeared to represent the largest observable discrepancy between data and simulation, and the observed shift in the measured bias factor was used as an estimate of the systematic uncertainty. The ECAL cluster multiplicity associated with τ-pair events was found to be underestimated in the τ MC samples used in this analysis, and introduces the only non-negligible systematic uncertainty to the bias factor estimate. A systematic uncertainty of ± 0.0013 was assigned to the bias factor measurement due to this effect. Combining the MC estimates from table 4.2 with the statistical

MC run	Total τ-pair events	F_{B}
1513	3.0×10^5	1.0014 ± 0.0032
1520	4.45×10^5	1.0011 ± 0.0028
1536	3.75×10^5	1.0008 ± 0.0027
1515 (peak$-$2 GeV)	1.0×10^5	0.9925 ± 0.0054
1516 (peak+2 GeV)	1.0×10^5	1.0047 ± 0.0054

Table 4.2: Bias factor estimates F_{B} obtained from various τ MC samples. All of these samples are based on the KORALZ [36] generator. The quoted errors are the statistical uncertainties obtained using equation 4.1.

and systematic uncertainty estimates discussed above and added in quadrature yields a bias factor estimate of $F_{\mathrm{B}} = 1.0009 \pm 0.0019$.

4.3 Backgrounds in the τ sample

Both the τ and $\tau^- \to \mathrm{e}^-\bar{\nu}_{\mathrm{e}}\nu_\tau$ samples, described in the following chapter, contain backgrounds from sources other than τ decays. Several potential background sources, including $\mathrm{e}^+\mathrm{e}^- \to \mathrm{e}^+\mathrm{e}^-$, $\mathrm{e}^+\mathrm{e}^- \to \mu^+\mu^-$, $\mathrm{e}^+\mathrm{e}^- \to \mathrm{q}\bar{\mathrm{q}}$, the two-photon mediated four-fermion channels $\mathrm{e}^+\mathrm{e}^- \to (\mathrm{e}^+\mathrm{e}^-)\mathrm{l}^+\mathrm{l}^-$, and various s-channel four-fermion final states, were evaluated and are discussed in the following sections. The MC simulations used to model these events are listed in table 3.1.

Estimates of the backgrounds were obtained by comparing the data and MC simulation using samples of data which were enhanced in the background source under consideration. In cases where the data are well-described by the simulation, the uncertainties in the background estimates were obtained from the data and MC statistical uncertainties. Otherwise the uncertainties were estimated from the level of disagreement between the MC prediction and the observed data distributions.

Figure 4.2 plots the total EM calorimeter energy fraction $E_{\rm tot}/E_{\rm cm}$ as a function of the total scalar momentum fraction $p_{\rm tot}/E_{\rm cm}$, for some of the sources contributing to the non-τ background. These backgrounds are described in the following sections.

4.3.1 $e^+e^- \to \mu^+\mu^-$

The dimuon ($e^+e^- \to \mu^+\mu^-$) background in the τ-sample was simulated using MC runs 1620 and 1636 [36]. A total of 5148 jets out of the 875 000 $e^+e^- \to \mu^+\mu^-$ simulated events in these two runs pass the τ selection described above. This background is composed of two distinct parts; a high visible energy component ($E_{\rm vis}/E_{\rm cm} \approx 1$) consisting of events in which one or both jets have failed to be identified as muons, and a small component in which the two muons have been correctly identified, but in which the event has been incorrectly classified as a double $\tau^- \to \mu^-\bar{\nu}_\mu\nu_\tau$ decay because it has $E_{\rm vis}/E_{\rm cm} < 0.6$. These two components are clearly visible in figure 4.2, with the high visible energy component along the diagonal, and the $E_{\rm vis}/E_{\rm cm} < 0.6$ component clustered near $p_{\rm tot}/E_{\rm cm} \approx 0.5$ and $E_{\rm tot}/E_{\rm cm} \approx 0$.

The high visible energy $e^+e^- \to \mu^+\mu^-$ events which enter into the τ sample are normally associated with regions of the detector lacking muon-chamber coverage due to structural support material in the detector. The high visible energy component of the dimuon background was estimated by examining the distribution of low acoplanarity ($\theta_{\rm acoplan} < 0.003$ radians) events with $E_{\rm vis}/E_{\rm cm}$ in the interval $0.8 < E_{\rm vis}/E_{\rm cm} < 1.2$ (see figure 4.3). The acoplanarity angle $\theta_{\rm acoplan}$ is defined as the supplement of the angle between the primary tracks in the two jets in the plane perpendicular to the beam direction. The excess of events in this region is consistent with the dimuon MC prediction. The background contribution was estimated to be $(0.50 \pm 0.02)\%$ where the quoted uncertainty is due to data statistics.

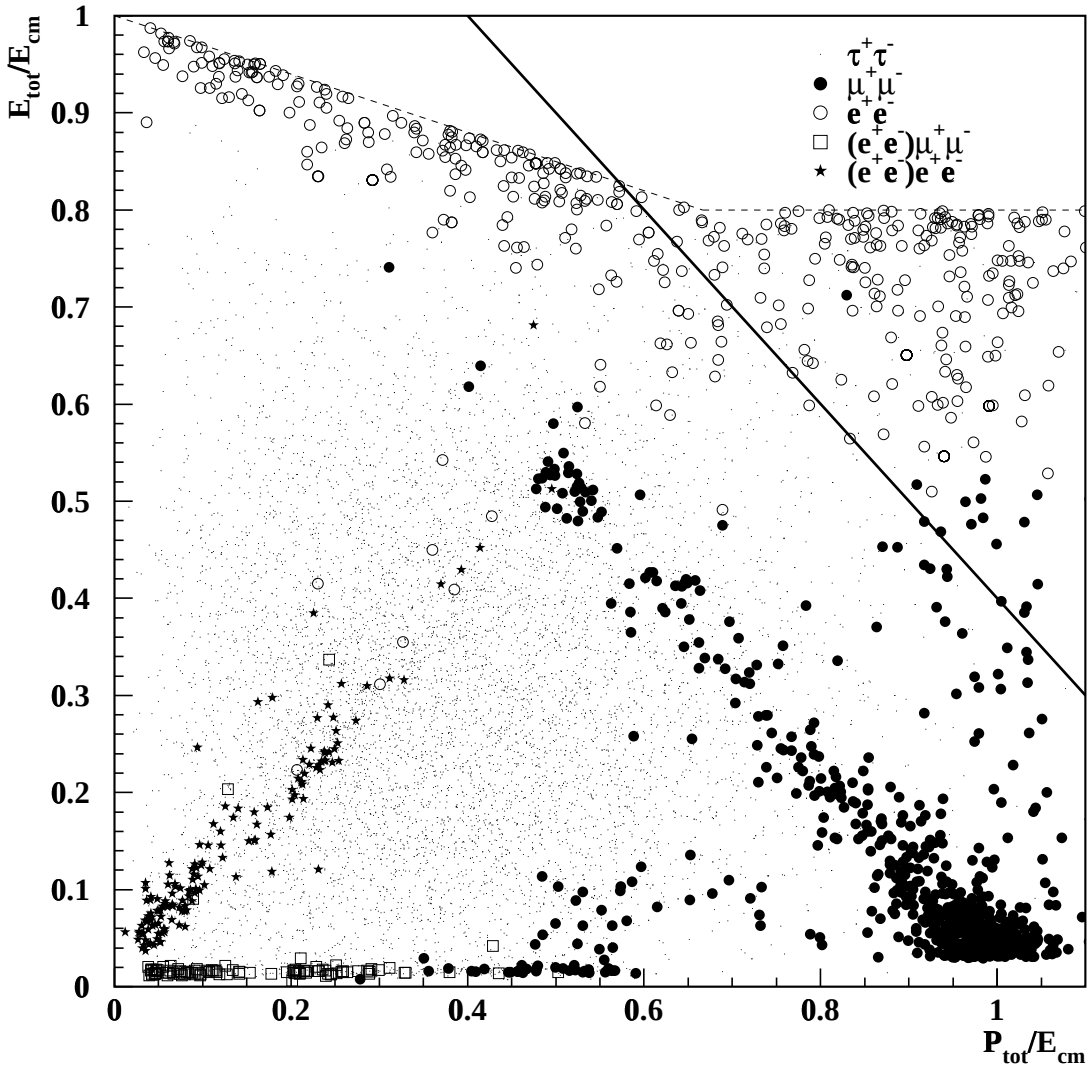

Figure 4.2: The total EM calorimeter energy ($E_{\rm tot}$) is plotted versus the scalar momentum sum ($p_{\rm tot}$), as a fraction of the centre of mass energy, for events passing the standard τ pair selection. MC predictions for various sources contributing to the non-τ background are shown and are described in the text. The standard Bhabha rejection cuts are shown as dashed lines, and Bhabha events failing these cuts have not been plotted. The modified Bhabha rejection cut $E_{\rm vis}/E_{\rm cm} \leq 1.4$ is shown as a solid line.

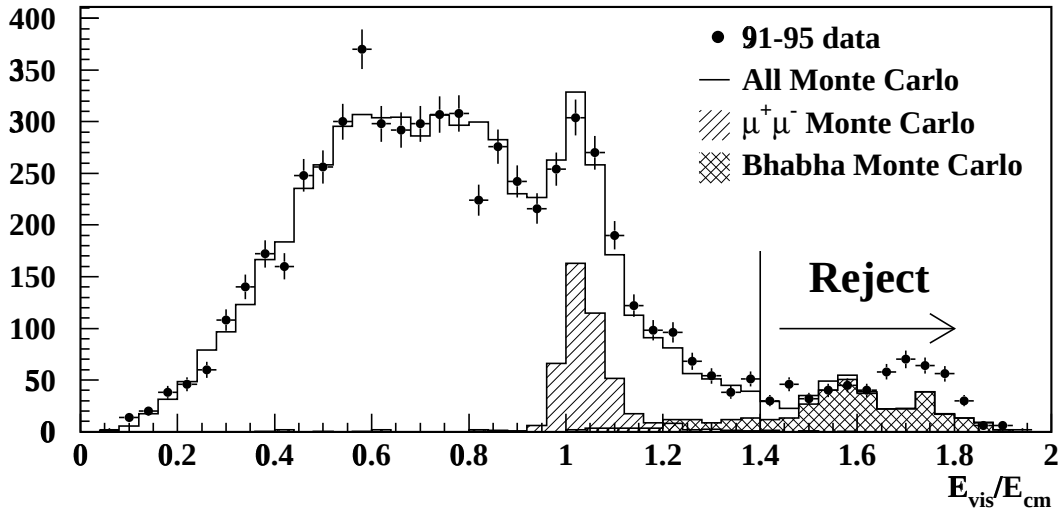

Figure 4.3: The visible energy fraction of standard τ-pair selected events possessing $\theta_{\rm acoplan} < 0.003$ radians is plotted. MC predictions for the $e^+e^- \to \mu^+\mu^-$ and $e^+e^- \to e^+e^-$ backgrounds are shown. The $e^+e^- \to \mu^+\mu^-$ MC can be seen to model the peak at $E_{\rm vis}/E_{\rm cm} = 1.0$ whereas the excess of non-radiative Bhabha events visible above the $E_{\rm vis}/E_{\rm cm} \leq 1.4$ cut is not well modelled by the Bhabha simulations. Note that this cut corresponds to the solid line in figure 4.2.

The $E_{\rm vis}/E_{\rm cm} < 0.6$ component of the $\mu^+\mu^-$ background is composed of events in which the momentum of one or both of the two muon tracks has been poorly reconstructed. This background is mainly attributable to tracks which pass close to CJ anode planes. This background is effectively eliminated in the current work by the geometrical requirements imposed on the anode plane regions (section 4.1.2). After applying these cuts, no excess of double-tagged muon events is observed in the region $0.5 < E_{\rm vis}/E_{\rm cm} < 0.6$. The MC prediction for the residual $\mu^+\mu^-$ background in this region is 0.02%, and this quantity is added to the high visible energy background with an associated systematic uncertainty of equal size ($\pm$0.02%) to give a total $e^+e^- \to \mu^+\mu^-$ background estimate of $0.52 \pm 0.03\%$.

4.3.2 $e^+e^- \to e^+e^-$

The Bhabha background in the τ-pair sample was evaluated using MC runs 1320 and 1335, based on the BABAMC [37] and BHWIDE [38] generators respectively. These two samples differ in that the BHWIDE generator models doubly-radiative Bhabha events while the BABAMC generator only models single-radiative events.

Bhabha events typically have $E_{\rm tot}/E_{\rm cm} \approx 1$ and $p_{\rm tot}/E_{\rm cm} \approx 1$ giving a total visible energy fraction $E_{\rm vis}/E_{\rm cm} \approx 2$, however $E_{\rm tot}$ or $p_{\rm tot}$ can be significantly reduced by either physics (i.e. radiation) or detector resolution effects. The Bhabha background in the standard τ-pairs sample is composed of e^+e^- events possessing comparatively low $E_{\rm tot}$ or $p_{\rm tot}$ measurements, and which have failed to be rejected by the standard preselection cut of $E_{\rm tot} \leq 0.8 \cdot E_{\rm cm}$ or $E_{\rm tot} + 0.3 \cdot p_{\rm tot} \leq E_{\rm cm}$ as shown in figure 4.2. These Bhabhas are considered to be radiative or non-radiative events depending on the scalar sum of the track momentum in the two jets. Events with $p_{\rm tot} > 0.7 \cdot E_{\rm cm}$ are considered to be non-radiative, and are characterized by low acoplanarity. Bhabhas with lower total momentum are considered to be radiative events and are typically much more acoplanar. The non-radiative component generally enters the τ-pair sample as a result of a degraded measurement of EM calorimeter cluster energies, so the MC prediction for this contribution is sensitive to ECAL energy modelling. This component is not well described in the present case (see figure 4.3), leading to a potentially large systematic uncertainty in the Bhabha background measurement, so a cut of $E_{\rm vis}/E_{\rm cm} \leq 1.4$ is applied in order to reject these events.

The radiative component of the Bhabha background survives this cut, and is better modelled by the two MC samples. This component generally clusters near the boundary of the $E_{\rm tot} + 0.3 \cdot p_{\rm tot} \leq E_{\rm cm}$ cut, so the remaining Bhabha background

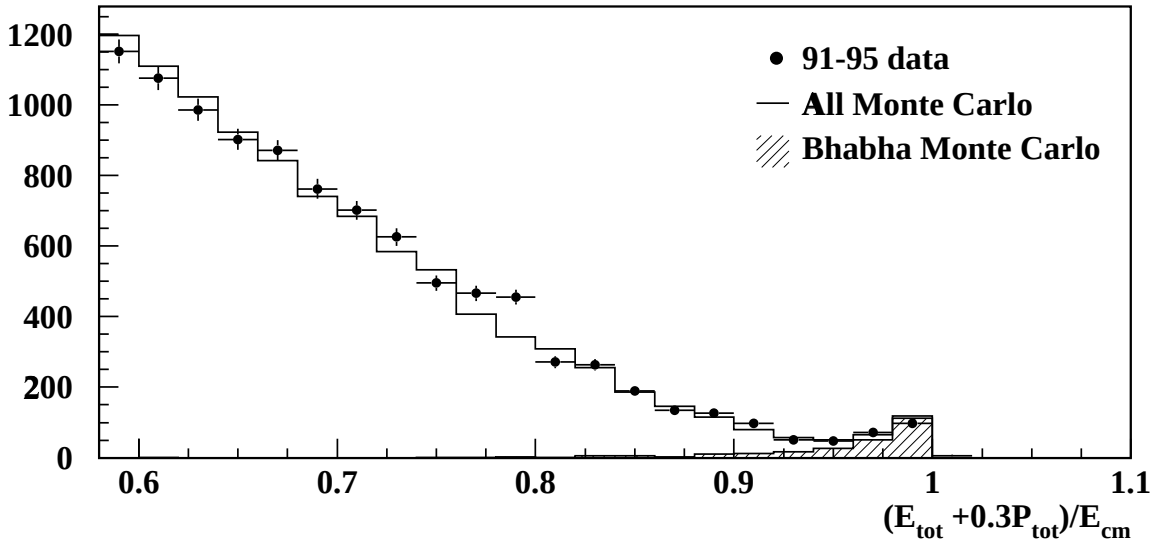

Figure 4.4: The Bhabha background in the τ sample. $(E_{\rm tot} + 0.3 \cdot p_{\rm tot})/E_{\rm cm}$ is plotted for events in which the opposite jet possesses a tagged electron. The Bhabha MC is scaled to correctly describe the excess which is visible towards the τ selection cut of $(E_{\rm tot} + 0.3 \cdot p_{\rm tot})/E_{\rm cm} = 1$.

was evaluated by comparing the distribution of $(E_{\rm tot} + 0.3 \cdot p_{\rm tot})/E_{\rm cm}$ for MC and data. This quantity is well described by the τ MC simulation, and a clear excess attributable to Bhabhas is observable near $(E_{\rm tot} + 0.3 \cdot p_{\rm tot})/E_{\rm cm} \simeq 1$ as shown in figure 4.4. The two Bhabha simulations produce similar background estimates and were therefore combined, and the resulting sample was found to correctly describe the shape but not the extent of the excess of events observed in data. The source of this discrepancy is attributable to ECAL energy modelling. The Bhabha MC background estimate was therefore scaled by a factor of 1.5 to give agreement with the observed excess, giving a background estimate of $(0.15 \pm 0.03)\%$, where the quoted uncertainty is taken as half the difference between the unscaled MC and data.

4.3.3 $e^+e^- \to q\bar{q}$

Jets produced by multihadronic events are typically less collimated than those resulting from τ decays. The $e^+e^- \to q\bar{q}$ background in the τ sample was evaluated by examining the collimation of tracks in the two jets. For this determination, the τ-selection track multiplicity requirement was relaxed to allow up to ten charged tracks per τ-pair event. This sample was then enhanced in $q\bar{q}$ events by requiring a total of at least five charged tracks in the event, and the angular distribution of charged tracks within each jet was examined. Figure 4.5 plots the maximum of the angular differences between charged tracks in a jet and the jet thrust axis. MC modelling of this distribution for τ decays was checked by requiring a tagged electron in the opposite jet in order to produce a clean data sample of $\tau^+\tau^-$ events. Comparison of data and MC were found to be in good agreement. The $q\bar{q}$ background was then reintroduced to the data sample by removing the electron tag requirement.

The $q\bar{q}$ background was simulated using MC runs 2790 - 2793, for a total of 4.0×10^6 multihadrons. These MC runs predict a $q\bar{q}$ background contribution to the τ sample which is approximately a factor of two higher than that which is actually observed in data. This effect is believed to be due to the modelling of the low-multiplicity tails of track and cluster multiplicity distributions. To avoid this problem, the normalization of the multihadron MC was obtained in the present work by a simultaneous fit of the $\tau^+\tau^-$ and $q\bar{q}$ MC simulations to the data rather than using the MC prediction. This gives a $q\bar{q}$ background estimate of 0.38 ± 0.05, where the quoted uncertainty is due to the variation in the fitting parameters. A consistent result was obtained when the track multiplicity requirement was tightened from ten to eight charged tracks and a similar fitting procedure was performed. As a consistency

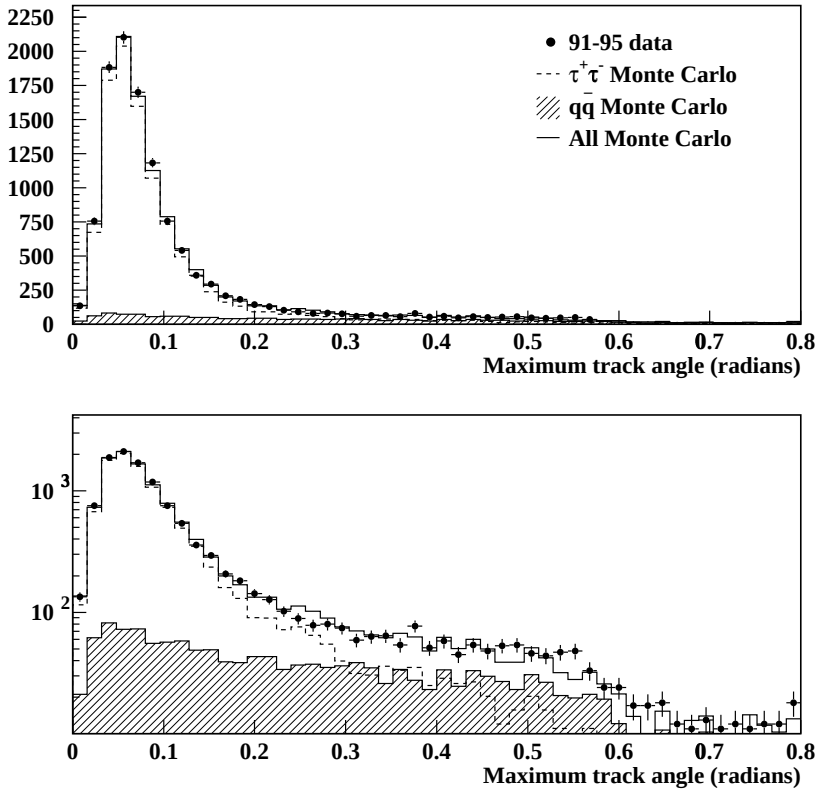

Figure 4.5: Estimation of the $q\bar{q}$ background in the τ sample. The largest angle between any charged track in a jet cone and the thrust axis of the jet is plotted for τ-pair selected events possessing a total of between four and eight tracks in the two jets. The $q\bar{q}$ MC prediction is scaled to correctly describe the excess of data compared to τ MC at high angles.

check, this procedure was repeated using $e^+e^- \rightarrow q\bar{q}$ MC runs 2291 and 2292, which have been found to better model the track and cluster multiplicities in the tails of the multiplicity distributions [48] and therefore give more reliable estimates of the $q\bar{q}$ background. The background estimates obtained with these MC simulations using the correct luminosity scaling were found to be consistent with the estimates obtained with runs 2790 - 2793 using the normalization obtained from fits to the data.

4.3.4 Two-photon mediated four-fermion backgrounds

Two-photon mediated four-fermion final states $e^+e^- \to (e^+e^-)l^+l^-$ are reduced in the τ-candidate sample by rejecting events with high acolinearity ($\theta_{\rm acol} > 15°$). In events which survive the τ selection, the final state (e^+e^-) pair is not usually observed because the two particles pass down the beampipe, and the two leptons from the l^+l^- pair are each reconstructed as a τ jet. The MC estimates of the $e^+e^- \to (e^+e^-)e^+e^-$ and $e^+e^- \to (e^+e^-)\mu^+\mu^-$ backgrounds were verified by examining the distribution of acolinear events possessing electrons or muons. A high-purity sample of $\tau^+\tau^-$ events was first obtained by selecting events possessing a tagged electron in one jet, and a tagged muon in the opposite jet in order to verify that the $\theta_{\rm acol}$ distribution was correctly modelled by the τ MC. Good agreement was found between data and simulation, and in particular the high-acolinearity region was found to be well modelled.

The two-photon $e^+e^- \to (e^+e^-)\mu^+\mu^-$ background was evaluated using a sample of 8.75×10^5 simulated events from MC runs 1716 and 1745, from which a total of 748 jets passed the τ selection. A sample of τ-selected data enhanced in $e^+e^- \to (e^+e^-)\mu^+\mu^-$ events was obtained by applying a muon tag to both jets in each τ-pair event and simultaneously requiring low total EM calorimeter energy deposition. An excess of acolinear events attributable to $e^+e^- \to (e^+e^-)\mu^+\mu^-$ was found in this sample and is shown in figure 4.6 (top). The MC prediction for the $e^+e^- \to (e^+e^-)\mu^+\mu^-$ background was verified by simultaneously fitting the τ MC and two-photon MC to this distribution. The $e^+e^- \to (e^+e^-)\mu^+\mu^-$ background was estimated from MC to be $(0.06 \pm 0.02)\%$, where the uncertainty reflects the level of agreement between the fit results and the MC prediction.

The $e^+e^- \to (e^+e^-)e^+e^-$ background was evaluated in a similar manner using

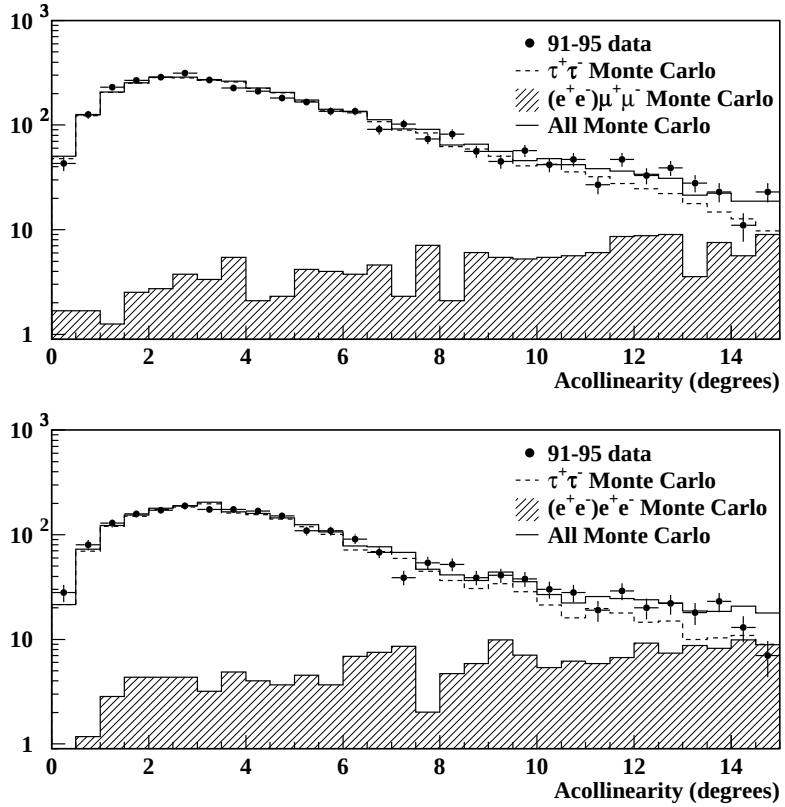

Figure 4.6: Two-photon $e^+e^- \to (e^+e^-)\mu^+\mu^-$ (top) and $e^+e^- \to (e^+e^-)e^+e^-$ (bottom) backgrounds in the τ sample. Events in the top plot have been selected by tagging a muon in both jets, while the lower plot consists of events possessing tagged electrons in both jets.

MC runs 1717 and 1746. A total of 1125 jets out of approximately 7.5×10^5 MC events survive the τ selection. An enhanced sample of $e^+e^- \to (e^+e^-)e^+e^-$ events was obtained by applying an electron tag to both jets in each τ-pair candidate event. The τ and two-photon MC samples were then simultaneously fit to the $\theta_{\rm acol}$ distribution obtained from the data (figure 4.6 bottom), and the best fit was found to be consistent with the MC prediction. The total $e^+e^- \to (e^+e^-)e^+e^-$ background in the τ sample was estimated to be $(0.11 \pm 0.01)\%$, where the uncertainty is due to data statistics.

Source	Background (%)
$e^+e^- \to \mu^+\mu^-$	0.52 ± 0.03
$e^+e^- \to e^+e^-$	0.15 ± 0.03
$e^+e^- \to q\bar{q}$	0.38 ± 0.05
$e^+e^- \to (e^+e^-)l^+l^-$	0.21 ± 0.02
total	1.26 ± 0.07

Table 4.3: Estimates of non-τ backgrounds in the τ candidate sample.

Two-photon $e^+e^- \to (e^+e^-)\tau^+\tau^-$ events were simulated using MC run 1744 [40], and contribute to the backgrounds in both the τ candidate sample and the $\tau^- \to e^-\bar{\nu}_e\nu_\tau$ sample. However, it was found that events of this type which pass the τ selection sufficiently resemble normal $e^+e^- \to \tau^+\tau^-$ events that they contribute equally to the backgrounds in the τ candidate sample and the $\tau^- \to e^-\bar{\nu}_e\nu_\tau$ sample. The total background in the τ sample from this channel was estimated to be $(0.045 \pm 0.005)\%$ where the quoted uncertainty is due to MC statistics, however they can be neglected (i.e. treated as signal rather than background) without introducing any significant systematic uncertainty to the $\tau^- \to e^-\bar{\nu}_e\nu_\tau$ branching ratio measurement.

4.3.5 Four fermion backgrounds

The background due to $e^+e^- \to e^+e^-$ scattering with initial or final state radiation was examined using MC run 6613 [41]. S-channel four fermion $e^+e^-q\bar{q}$, $\mu^+\mu^-q\bar{q}$, $e^+e^-e^+e^-$, $e^+e^-\mu^+\mu^-$, $\mu^+\mu^-\tau^+\tau^-$ and $\mu^+\mu^-\mu^+\mu^-$ final states were examined using MC runs 6503, 6504, 6506, 6507, 6509, 6510 and 6511 [42]. The combined MC prediction for the background in the τ sample from these sources is negligible.

MC run 6508 [42] was used to examine $e^+e^- \to e^+e^-\tau^+\tau^-$ production. The background in the τ candidate sample from this source was estimated from MC to

be $(0.21 \pm 0.01)\%$. However, in these events the two electrons generally possess low momentum and are not reconstructed as the primary track in either of the two τ jets. The $\tau^- \to e^- \bar{\nu}_e \nu_\tau$ selection algorithm described in chapter 5 therefore correctly reconstructs the decays of the two τ in these events. These events therefore sufficiently resemble $\tau^+\tau^-$ events they they can be treated as signal rather than background with a negligible contribution to the $\tau^- \to e^- \bar{\nu}_e \nu_\tau$ branching ratio measurement systematic uncertainty.

4.4 Overview of the τ candidate sample

A total of 186197 jets were selected from the 1991-1995 OPAL PASS 7 data set using the selection described above. The total background in this sample due to non-τ events is estimated to be $(1.26 \pm 0.07)\%$. Contributions to this background are summarized in table 4.3. This sample of τ jets is used as a basis for the $\tau^- \to e^- \bar{\nu}_e \nu_\tau$ branching ratio measurement, as described in the following two chapters.

Chapter 5

Selection of $\tau^- \to e^- \bar{\nu}_e \nu_\tau$ candidates

Candidate $\tau^- \to e^- \bar{\nu}_e \nu_\tau$ decays are identified from the sample of selected τ jets using a cut-based preselection followed by a likelihood selection. The selection variables and related quantities are described in section 5.1, and the $\tau^- \to e^- \bar{\nu}_e \nu_\tau$ selection procedure is presented in the following sections.

5.1 Description of selection variables

The selection variables used in this analysis are improved versions of the kinematic variables used in a previous $B(\tau^- \to e^- \bar{\nu}_e \nu_\tau)$ measurement [49]. Modelling of the selection variables was checked over the entire momentum range using selected samples of τ decays. These variables are mostly uncorrelated for $\tau^- \to e^- \bar{\nu}_e \nu_\tau$ decays, and so data control samples for checks of each variable were obtained by applying selections using the variables described below, excluding the variable under consideration. Corrections to the MC simulation were applied where appropriate, and are described in the text. Additional verification of variable distributions was performed at high and low momentum using Bhabha and $e^+e^- \to (e^+e^-)e^+e^-$ data samples respectively.

5.1.1 Clustering and jet finding algorithms

This analysis uses the UVic fine clustering algorithm developed for τ decays [50]. Clusters in the barrel electromagnetic calorimeter are limited to a maximum size of 2×2 EB blocks and are formed around blocks which possess a local energy maximum. Blocks forming the cluster centroid must have energy greater than 250 MeV. Clusters are then formed around these blocks using the combination of 2×2 blocks which yields the maximum total cluster energy.

Once a cluster has been identified in this manner the position centroid of the cluster is determined using a cube-root energy weighting scheme for blocks in the cluster. The uncertainty in the position of the cluster is reduced when the energy is distributed over several blocks rather than mostly concentrated in a single block. Fluctuations in ECAL energy deposition by hadrons result in large variations in the reconstructed cluster position compared with that produced by electrons or photons. The cluster centroid position typically has a resolution of $1 - 2$ mrad for electrons and photons and ~ 9 mrad for hadrons.

A jet finding algorithm is re-applied to τ-pair events using the ECAL clusters defined by the fine clustering algorithm. Jets are initially defined in a cone of half-angle 35° centred about the highest energy track or cluster. The next-highest energy track or cluster in the jet-cone is then added, and the jet direction is redefined by the sum. This process continues until all good tracks and clusters within the jet-cone have been added. Once the jet direction has been defined in this manner, the cone half-angle is reduced to 500 mrad and all tracks and clusters outside of the new cone are dropped. The sum of the total ECAL energy and track momenta is required to be greater than $0.01 \cdot E_\mathrm{beam}$ for a jet to be accepted.

5.1.2 Track-cluster matching

Charged tracks in CJ are associated to EB clusters using a χ^2 variable describing the match between the θ and ϕ positions of the track and cluster. The track is extrapolated to the ECAL inner face, and the two quantities

$$\chi^2_\theta \equiv \frac{(\theta_{\mathrm{clus}} - \theta_{\mathrm{track}})^2}{(\sigma^\theta_{\mathrm{clus}})^2 + (\sigma^\theta_{\mathrm{track}})^2} \quad , \quad \chi^2_\phi \equiv \frac{(\phi_{\mathrm{clus}} - \phi_{\mathrm{track}})^2}{(\sigma^\phi_{\mathrm{clus}})^2 + (\sigma^\phi_{\mathrm{track}})^2} \tag{5.1}$$

are computed for each track-cluster combination, where $(\theta_{\mathrm{track}} \pm \sigma^\theta_{\mathrm{track}})$ and $(\phi_{\mathrm{track}} \pm \sigma^\phi_{\mathrm{track}})$ are the value and uncertainty of the extrapolated track position in θ and ϕ, and $(\theta_{\mathrm{clus}} \pm \sigma^\theta_{\mathrm{clus}})$ and $(\phi_{\mathrm{clus}} \pm \sigma^\phi_{\mathrm{clus}})$ are the positions reconstructed from the ECAL cluster centroid. The uncertainties in the cluster position are fixed to 9 mrad in both θ and ϕ. A cluster is considered to be associated with a track if both $\chi^2_\theta < 16$ and $\chi^2_\phi < 16$. If more than one cluster is associated to a track, then the cluster with smallest $\chi^2_{\mathrm{total}} \equiv \sqrt{(\chi^2_\theta)^2 + (\chi^2_\phi)^2}$ is taken to be the best match. The number of clusters, N_{ACl}, associated to the highest momentum track in the jet is shown in figure 5.1 for data and MC. $\tau^- \to \mathrm{e}^-\bar{\nu}_\mathrm{e}\nu_\tau$ decays typically have only a single associated cluster, and at low track momentum may have no associated cluster. Clusters which are not associated to any charged track, or which are associated to the track but are not the best match, are considered as *neutral cluster* candidates.

5.1.3 $N(\Delta\theta)$ and $N(\Delta\phi)$

The difference in the resolution of the position measurements, θ_{clus} and ϕ_{clus}, can be used to discriminate $\tau^- \to \mathrm{e}^-\bar{\nu}_\mathrm{e}\nu_\tau$ decays from hadronic τ decays. The quantities $\Delta\theta \equiv \theta_{\mathrm{clus}} - \theta_{\mathrm{track}}$ and $\Delta\phi \equiv \phi_{\mathrm{clus}} - \phi_{\mathrm{track}}$ give a measure of agreement between the position of the highest momentum track and position of the best-matched ECAL cluster. Because the resolution of $\Delta\theta$ and $\Delta\phi$ are dependent on the track momen-

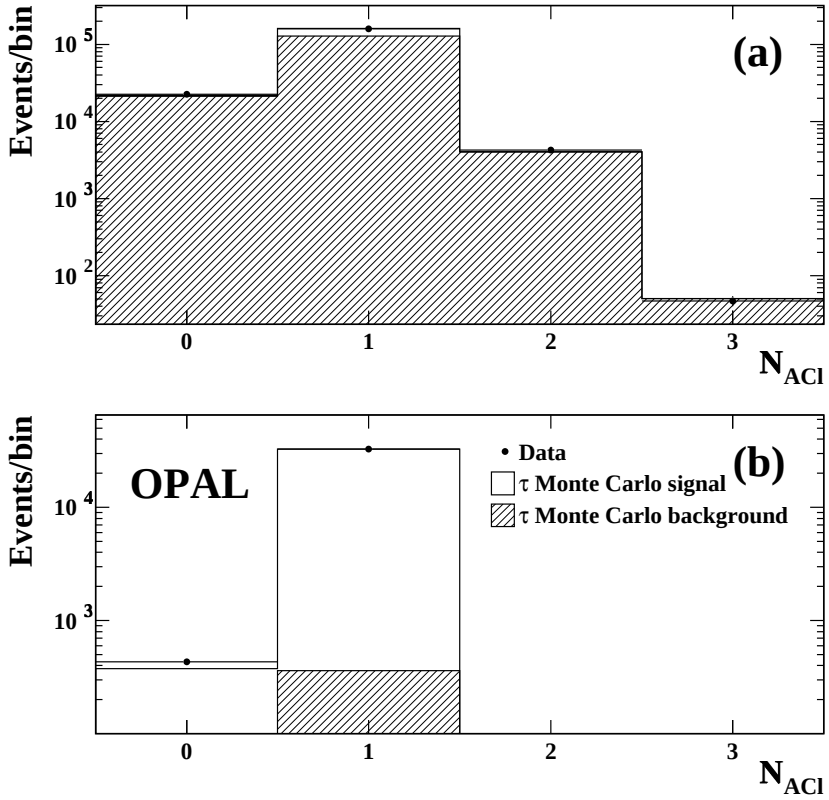

Figure 5.1: The number of ECAL clusters associated to the highest momentum track, N_{ACl}, is plotted for (a) all τ decays, and for (b) a sample which is enhanced in $\tau^- \to \mathrm{e}^-\bar{\nu}_\mathrm{e}\nu_\tau$ decays.

tum, these quantities are "normalized" under an electron hypothesis using a similar parameterization as is first proposed in reference [49]. Normalization of these variables is accomplished by parameterizing the mean $\mu(p)$ and width $\sigma(p)$ of the $\Delta\theta$ and $\Delta\phi$ distributions for $\tau^- \to \mathrm{e}^-\bar{\nu}_\mathrm{e}\nu_\tau$ events as a function of track momentum, and then defining the normalized quantity (e.g.. $\Delta\theta$);

$$N(\Delta\theta) \equiv \frac{(\Delta\theta - \mu_{\Delta\theta}(p))}{\sigma_{\Delta\theta}(p)} \quad . \tag{5.2}$$

The resulting normalized variable is centred at zero, has a width of unity and is independent of momentum for $\tau^- \to \mathrm{e}^-\bar{\nu}_\mathrm{e}\nu_\tau$ events. The two normalized track-cluster

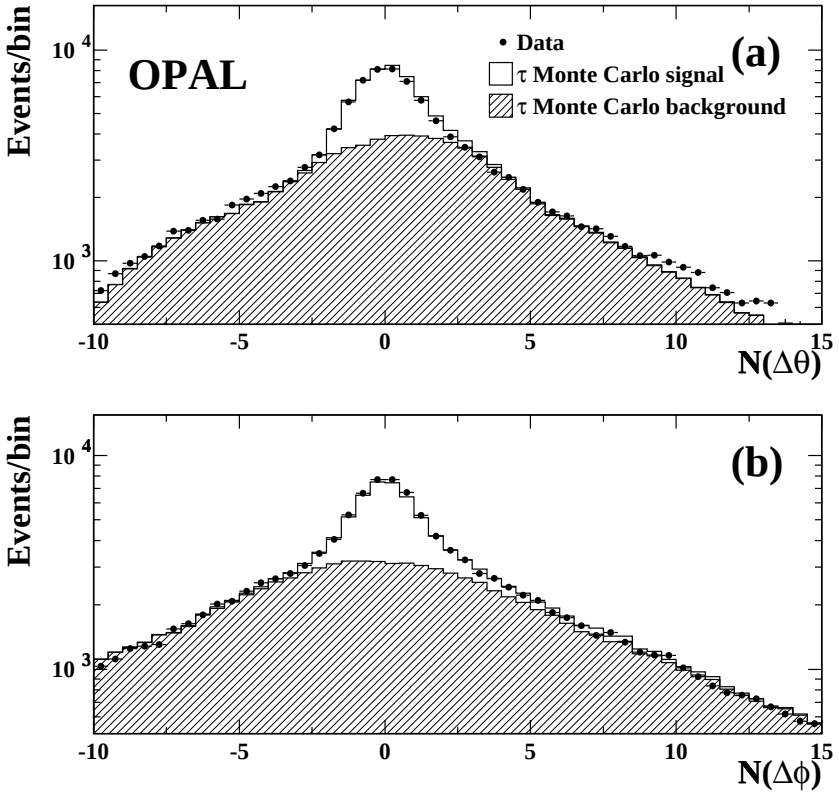

Figure 5.2: Data and MC simulation of the two normalized track-cluster matching variables (a) $N(\Delta\theta)$ and (b) $N(\Delta\phi)$ for all jets in the τ sample.

matching variables are plotted in figure 5.2. At low momentum these two variables are not well modelled and their resolving power of is limited. $N(\Delta\theta)$ and $N(\Delta\phi)$ are therefore only defined for events in which the highest momentum track has momentum $p \geq 5.0$ GeV. Because θ_{track} relies strongly on CZ information, $N(\Delta\theta)$ is not defined for τ events with less than three CZ hits.

5.1.4 Energy calibration and smearing

A comparison of ECAL calibration between data and simulation was performed by comparing the E/p distribution for a control sample of $\tau^- \to \mathrm{e}^-\bar{\nu}_\mathrm{e}\nu_\tau$ events. These

events deposit approximately 99% of their energy in the ECAL, so the ratio of the ECAL cluster energy (E) to the track momentum (p) should be approximately unity. MC run 1536 was found to consistently underestimate E/p compared with data over the full available momentum range. MC cluster energies were scaled up by a factor 1.005 to correct for this discrepancy. The corrected E/p is plotted as a function of the track momentum in figure 5.3a. The ECAL energy resolution was extracted from the E/p distributions for data and MC in bins of track momentum. The mean $\mu_{E/p}(p)$ and width $\sigma_{E/p}(p)$ were obtained from a Gaussian fit to the E/p distribution for each momentum bin. The two results were compared by taking the quadratic difference of the measured data and MC E/p resolutions and the MC was found to underestimate the data resolution at low momentum as shown in figure 5.3b. The difference was attributed to the ECAL energy resolution and parameterized by the function

$$\left(\frac{\sigma_E}{E}\right)_{\mathrm{smear}} = 0.001 + \frac{0.065}{\sqrt{E}} \quad . \tag{5.3}$$

The MC ECAL cluster energies were then smeared by this amount, resulting in good agreement between data and MC (figure 5.3c).

The momentum dependence of the mean and width of the E/p distribution were extracted from data and parameterized by the functions

$$\mu_{E/p}(p) = 1.035 - 0.20/\sqrt{p} \quad , \quad \sigma_{E/p}(p) = 0.029 + 0.115/\sqrt{p} \quad . \tag{5.4}$$

Using these parameterizations a normalized E/p variable was constructed, defined by

$$N(E/p) \equiv \frac{(E/p - \mu_{E/p}(p))}{\sigma_{E/p}(p)} \quad . \tag{5.5}$$

The $N(E/p)$ distribution is plotted for data and MC in figure 5.3d.

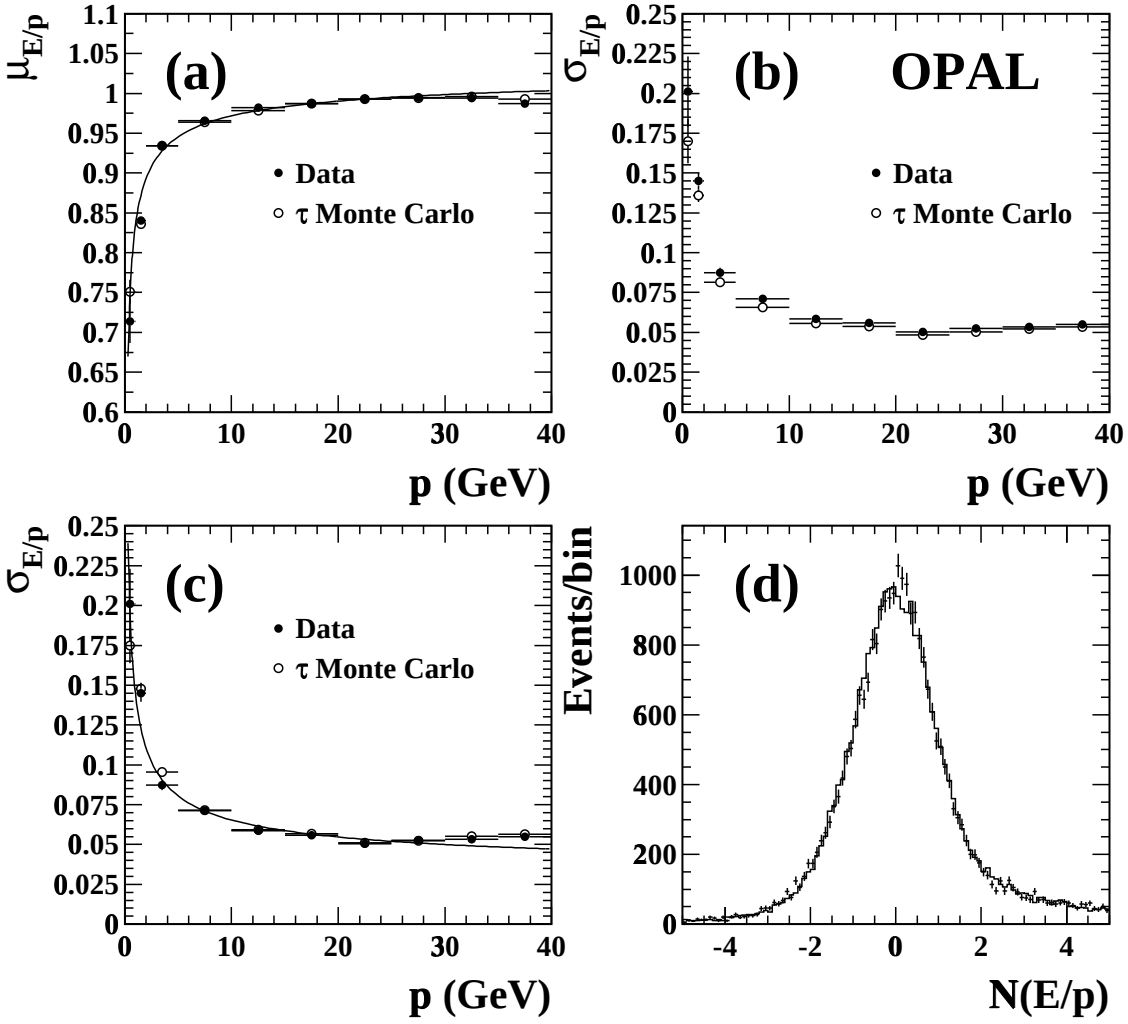

Figure 5.3: Parameterization of the ECAL energy resolution and E/p normalization: (a) The mean value $\mu_{E/p}$ of the ratio of E/p as a function of the track momentum p for $\tau^- \to \mathrm{e}^-\bar{\nu}_\mathrm{e}\nu_\tau$ events, showing the fit to equation 5.4. The width $\sigma_{E/p}$ as a function of p before (b) and after (c) applying the MC energy resolution correction from equation 5.3. The $\sigma_{E/p}(p)$ parameterization function from equation 5.4 is shown in (d). The distribution of $N(E/p)$ is plotted for data (points) and MC (solid histogram) for jets within the $\tau^- \to \mathrm{e}^-\bar{\nu}_\mathrm{e}\nu_\tau$ control sample.

Sample	μ	S
91 data	10.11	1.0
92 data	10.01	1.0
93 data	10.02	1.0
94 data	9.96	1.0
95 data	9.98	1.0
MC 1536 $\tau^- \to \mathrm{e}^-\bar{\nu}_\mathrm{e}\nu_\tau$	9.94	1.05
MC 1536 $\tau^- \to$ hadrons ν_τ	9.94	1.0

Table 5.1: Parameters used for $\mathrm{d}E/\mathrm{d}x$ normalization. μ represents the mean value used, and S is the width correction factor. Width corrections are applied only to MC simulation.

5.1.5 $\mathrm{d}E/\mathrm{d}x$

Ionization energy deposition ($\mathrm{d}E/\mathrm{d}x$) in the jet chambers is illustrated in figure 3.4. Because the $\mathrm{d}E/\mathrm{d}x$ resolution is dependent on the number of CJ wires used for the measurement, at least 20 CJ hits are required for $\mathrm{d}E/\mathrm{d}x$ to be considered well-measured. The $\mathrm{d}E/\mathrm{d}x$ is normalized under an electron hypothesis in order to maximize the rejection power of this variable. The normalized $\mathrm{d}E/\mathrm{d}x$ is defined as:

$$N(\mathrm{d}E/\mathrm{d}x) \equiv \frac{(\mathrm{d}E/\mathrm{d}x - \mu_{\mathrm{d}E/\mathrm{d}x})}{S \cdot \sigma_{\mathrm{d}E/\mathrm{d}x}} \tag{5.6}$$

where $\mu_{\mathrm{d}E/\mathrm{d}x}$ is the central value of the electron peak, σ is the electron $\mathrm{d}E/\mathrm{d}x$ width, as shown in the right-hand plot in figure 3.4, and S is a width correction factor for MC. The central value $\mu_{\mathrm{d}E/\mathrm{d}x}$ was extracted from data on a year-by-year basis, and from MC, by fitting a Gaussian distribution to a control sample of $\tau^- \to \mathrm{e}^-\bar{\nu}_\mathrm{e}\nu_\tau$ decays and are listed in table 5.1. After correcting the data and MC $\mathrm{d}E/\mathrm{d}x$ central values, the MC $N(\mathrm{d}E/\mathrm{d}x)$ width was compared with data and a correction factor of $S = 1.05$ was applied to simulated $\tau^- \to \mathrm{e}^-\bar{\nu}_\mathrm{e}\nu_\tau$ decays. No width correction was applied to simulated hadronic decays or to data.

Momentum bin (GeV)	$\tau^- \to \mathrm{e}^-\bar{\nu}_\mathrm{e}\nu_\tau$ fraction	$\tau^- \to$ hadrons ν_τ fraction
0 - 10	0.005	0.135
10 - 20	0.035	0.27
20 - 30	0.035	0.40
30 - 40	0.055	0.30

Table 5.2: The fraction of MC $\tau^- \to \mathrm{e}^-\bar{\nu}_\mathrm{e}\nu_\tau$ and $\tau^- \to$ hadrons ν_τ events which have N_{HCAL} corrected in each of the four momentum bins.

5.1.6 HCAL penetration

The depth of penetration of a particle or shower in the hadron calorimeter (HCAL) is measured in terms of the number of layers of the HB which have activity associated with the jet. N_{HCAL} is defined to be the depth in layers of the first HB layer which is followed by two successive layers which have no hits. Hadrons and muons typically penetrate much deeper into the HCAL than electrons so N_{HCAL} can be used to discriminate τ decay modes. MC modelling of this variable has been shown to underestimate the fraction of both electrons and hadrons that penetrate into the HCAL. The electron modelling was corrected by increasing N_{HCAL} by one layer for a momentum-dependent fraction of simulated $\tau^- \to \mathrm{e}^-\bar{\nu}_\mathrm{e}\nu_\tau$ decays in a manner identical to [49]. HCAL penetration was corrected for hadrons by adding between 1 - 3 layers, randomly and with equal probability, to a fraction of hadronic events which formerly had $N_{\mathrm{HCAL}} = 0$. Hadronic events which had $N_{\mathrm{HCAL}} > 0$ were not corrected. The HCAL correction factors for electrons and hadrons are taken from reference [49] and listed in table 5.2.

$N_{\mathrm{tracks}} \leq 3$	
$N_{\mathrm{neut}} \leq 2$	
$N_{\mathrm{HCAL}} \leq 3$	
$N_{\mathrm{ACl}} = \begin{cases} 1 & p \geq 5.0 \text{ GeV} \\ 0 \text{ or } 1 & p < 5.0 \text{ GeV} \end{cases}$	
$N(\mathrm{d}E/\mathrm{d}x) > -3.5$ or $N^{\mathrm{hits}}_{dE/dx} \leq 20$	(primary track)
$N(E/p) > -6.0$ or $N_{\mathrm{ACl}} = 0$	(primary track)

Photon conversion cuts:

$p_2 < 4.0$ GeV
$p_2 + p_3 < 6.0$ GeV
$\lvert N(\mathrm{d}E/\mathrm{d}x)_2 \rvert < 2.5$
$N(\mathrm{d}E/\mathrm{d}x)_2 \oplus N(\mathrm{d}E/\mathrm{d}x)_3 < 2.5$

Table 5.3: A summary of $\tau^- \to \mathrm{e}^-\bar{\nu}_\mathrm{e}\nu_\tau$ preselection cuts.

5.2 $\tau^- \to \mathrm{e}^-\bar{\nu}_\mathrm{e}\nu_\tau$ preselection

A $\tau^- \to \mathrm{e}^-\bar{\nu}_\mathrm{e}\nu_\tau$ decay in the OPAL detector typically consists of a single track in the jet chamber, associated with a single ECAL cluster possessing essentially the full energy of the incident electron, and little or no activity in the HCAL. Because the track is produced by the decay electron, it will have $\mathrm{d}E/\mathrm{d}x$ consistent with an electron. The preselection consists of a collection of loose selection cuts that reject τ jets which are clearly inconsistent with $\tau^- \to \mathrm{e}^-\bar{\nu}_\mathrm{e}\nu_\tau$ decays. These cuts also serve to create a sample of events with well-defined kinematic variables to which the likelihood selection can be applied. The preselection reduces the background from hadronic τ decays to approximately 16% and from $\tau^- \to \mu^-\bar{\nu}_\mu\nu_\tau$ decays to a negligible level while retaining over 99% of $\tau^- \to \mathrm{e}^-\bar{\nu}_\mathrm{e}\nu_\tau$ decays. The preselection requirements are described below and are summarized in table 5.3.

In the majority of $\tau^- \to \mathrm{e}^-\bar{\nu}_\mathrm{e}\nu_\tau$ decays, the decay electron produces the only charged track reconstructed by the detector. However, in approximately 2% of these

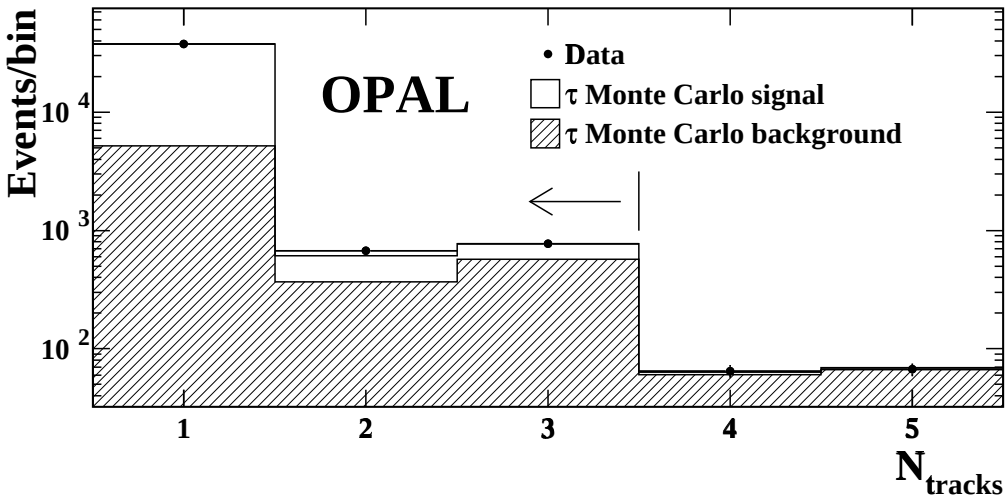

Figure 5.4: Comparison of data and MC simulation of the number of tracks N_{tracks} in the τ jet cone for τ jets which have passed all other preselection cuts. The region selected by the cut on N_{tracks} is indicated by the arrow.

decays a radiated photon converts to an $\mathrm{e}^+\mathrm{e}^-$ pair, producing additional tracks in the jet chamber which may or may not be associated with distinct ECAL clusters. If more than one track is present in a jet, the highest momentum track is assumed to be the $\tau^- \to \mathrm{e}^-\bar{\nu}_\mathrm{e}\nu_\tau$ electron candidate track and is referred to as the *primary track*. Additional tracks are numbered in order of decreasing momentum. The number of tracks in the jet (N_{tracks}) is plotted in figure 5.4 for τ jets which pass all other preselection requirements. In order to accept $\tau^- \to \mathrm{e}^-\bar{\nu}_\mathrm{e}\nu_\tau$ decays possessing tracks from photon conversions, jets with up to three tracks are accepted by the preselection.

All $\tau^- \to \mathrm{e}^-\bar{\nu}_\mathrm{e}\nu_\tau$ candidate jets which have primary track momentum $p \geq 5$ GeV are required to have exactly one ECAL cluster associated to the track. Figure 5.5 plots the momentum of events in a control sample of $\tau^- \to \mathrm{e}^-\bar{\nu}_\mathrm{e}\nu_\tau$ events which possess no associated cluster. The τ MC underestimates the fraction of $\tau^- \to \mathrm{e}^-\bar{\nu}_\mathrm{e}\nu_\tau$ events which possess no associated cluster by approximately 20%, so the simulation

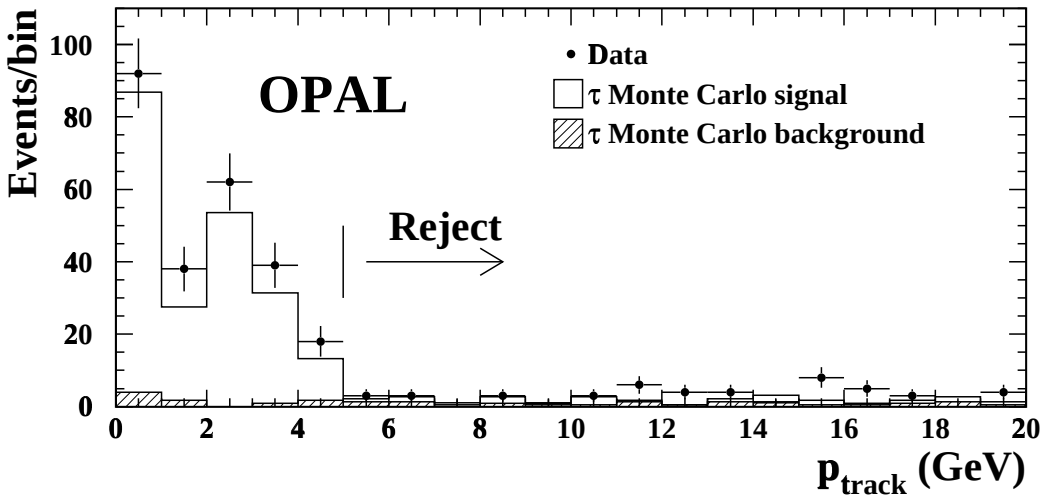

Figure 5.5: Comparison of data and MC simulation, before scaling, of the momenta of charged tracks possessing no associated cluster in a control sample of $\tau^- \to \mathrm{e}^-\bar{\nu}_\mathrm{e}\nu_\tau$ events. An excess of data over the MC prediction is apparent at low momentum. The preselection cut is indicated by the arrow.

is corrected accordingly. Jets with $p < 5$ GeV are accepted even if the primary track has no associated cluster.

ECAL clusters which are not associated to tracks are referred to as neutral clusters. Neutral clusters in the EB are produced by either photons or π^0 mesons. In $\tau^- \to \mathrm{e}^-\bar{\nu}_\mathrm{e}\nu_\tau$ decays, additional ECAL clusters may be produced by final state radiation or bremsstrahlung photons, however these clusters tend to lie in a narrow band $|\theta_\mathrm{clus} - \theta_\mathrm{track}| < 0.01$ radians, with $q \cdot (\phi_\mathrm{clus} - \phi_\mathrm{track}) > 0$ for tracks with charge q [49]. Clusters which lie within this region are not considered to be neutral clusters. Jets containing up to two neutral clusters are accepted by the preselection. The number of neutral clusters (N_neut) is plotted in figure 5.6a.

The electromagnetic shower produced by the electron from a $\tau^- \to \mathrm{e}^-\bar{\nu}_\mathrm{e}\nu_\tau$ decay is normally fully contained in the ECAL, so little or no activity is expected in

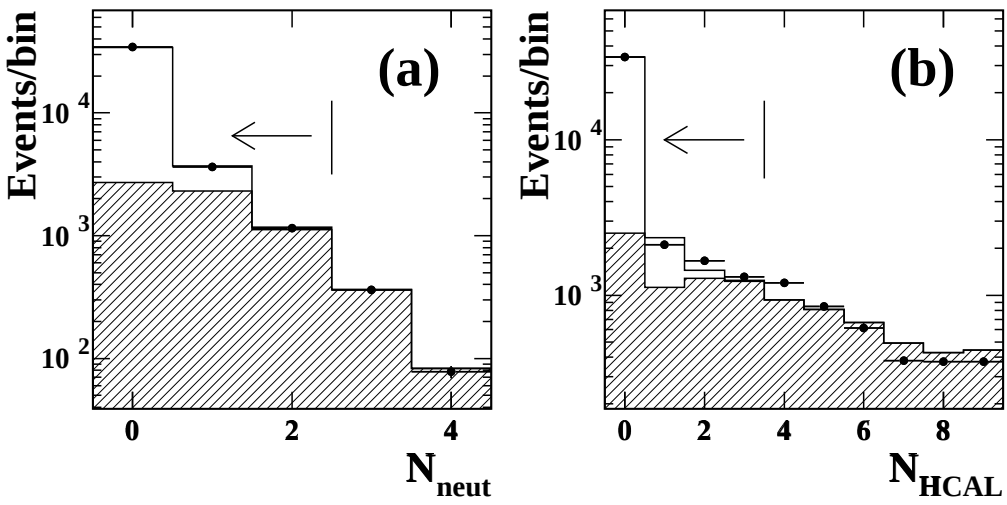

Figure 5.6: Comparison of data and MC simulation of (a) the number of neutral clusters N_{neut} and (b) the depth of penetration (in layers) into the HCAL N_{HCAL} for τ jets which have passed all preselection cuts other than the cut on the plotted variable. The points represent data, the solid histogram is MC, the hatched region is MC background prediction and preselection cuts are indicated by the arrows.

the hadron calorimeter (HCAL). The depth of penetration of τ-decay products into the HCAL is measured using the number of sequential HCAL layers with activity associated with the jet (N_{HCAL}). The number of penetrated HCAL layers is plotted in figure 5.6b. Jets with HCAL activity beyond the third layer are rejected. The discrepancy between data and Monte Carlo in this plot is due to the modelling of τ hadronic decays rather than $\tau^- \to \mathrm{e}^-\bar{\nu}_\mathrm{e}\nu_\tau$ decays, and its effect on the estimated background is understood.

The ratio of the energy of the associated ECAL cluster (E) to the momentum of the primary track (p) is typically near unity for $\tau^- \to \mathrm{e}^-\bar{\nu}_\mathrm{e}\nu_\tau$ decays, and less than one for other τ decays. This ratio is normalized as described above to create the selection variable $N(E/p)$ shown in figure 5.7a. A preselection cut of $N(E/p) > -6.0$ is applied to all jets in which an ECAL cluster is associated to the primary track.

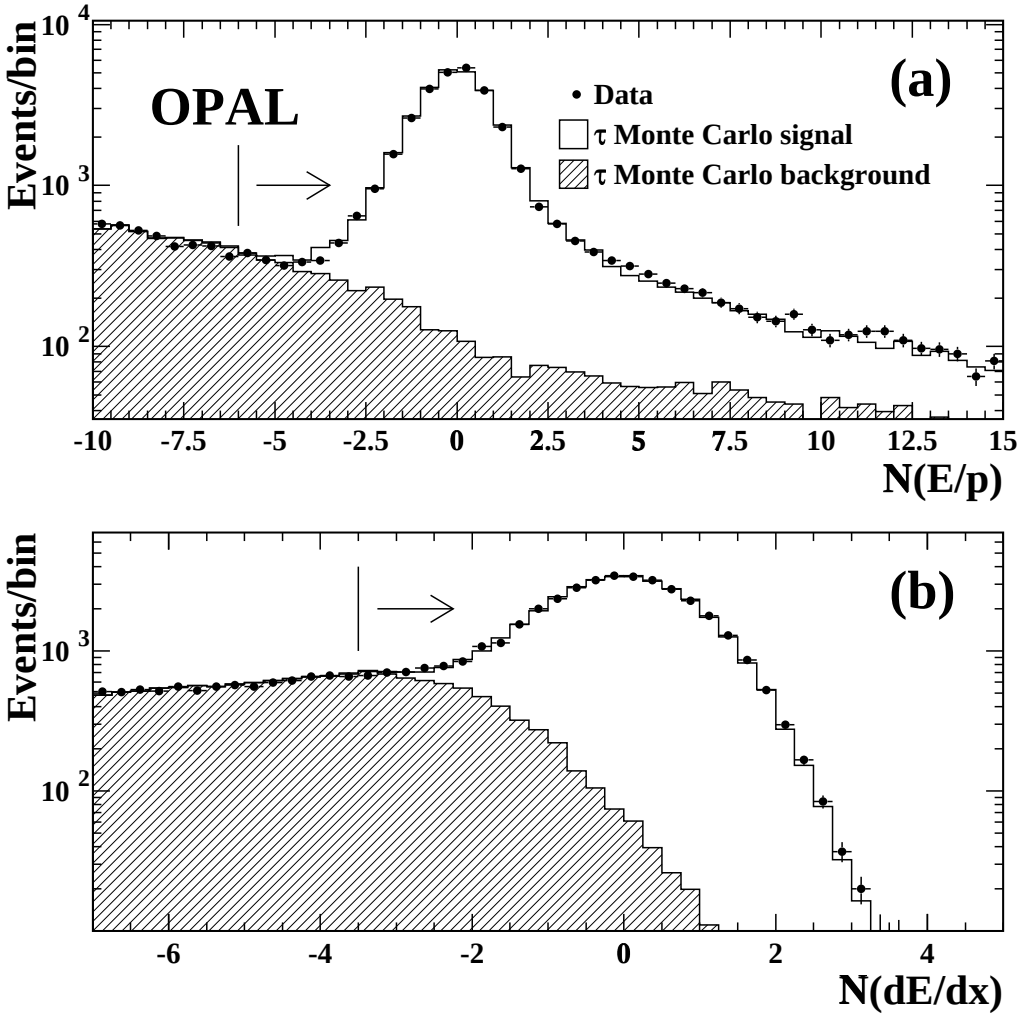

Figure 5.7: Comparison of data and MC simulation of the (a) $N(E/p)$ and (b) $N(\mathrm{d}E/\mathrm{d}x)$ distributions for τ jets which have passed all other preselection cuts. The arrows indicate the regions accepted by the preselection cuts on $N(E/p)$ and $N(\mathrm{d}E/\mathrm{d}x)$.

The ionization energy deposition ($\mathrm{d}E/\mathrm{d}x$) of a charged particle traversing the central jet chamber is considered to be well-measured if more than 20 out of a possible 159 signal wires collect a measurable charge that can be used for the $\mathrm{d}E/\mathrm{d}x$ determination. This criterion is satisfied for approximately 99.7% of electrons produced by $\tau^- \to \mathrm{e}^-\bar{\nu}_\mathrm{e}\nu_\tau$ decays. The normalized quantity $N(\mathrm{d}E/\mathrm{d}x)$ is constructed for all tracks with a well-measured $\mathrm{d}E/\mathrm{d}x$. Jets in which the primary track possesses a well-measured $\mathrm{d}E/\mathrm{d}x$ with $N(\mathrm{d}E/\mathrm{d}x) \leq -3.5$ are rejected (see figure 5.7b).

Because the preselection accepts jets with up to three tracks, additional restrictions must be applied to tracks other than the primary track in order to reduce the background due to hadronic τ decays. This background is composed primarily of $\tau^- \to 2\pi^-\pi^+\nu_\tau$ and $\tau^- \to \pi^-(\geq 1\pi^0)\nu_\tau$ decays in which an electron from a photon conversion has higher momentum than the the pion track. Cuts are therefore applied in order to ensure that the second and third track in the jet have properties which are consistent with electrons produced by a photon conversion. The second track is required to have momentum less than 4.0 GeV, and if the jet contains three tracks, then the scalar sum of the momenta of the second and third tracks must be less than 6.0 GeV. The quadratic sum of the $N(\mathrm{d}E/\mathrm{d}x)$ of conversion-candidate tracks with well-measured $\mathrm{d}E/\mathrm{d}x$ is required to be less than 2.5. These cuts are shown in figure 5.8.

The fraction of simulated $\tau^- \to \mathrm{e}^-\bar{\nu}_\mathrm{e}\nu_\tau$ events which possess one or more conversion tracks was found to be underestimated by the MC. Because the efficiency for identifying $\tau^- \to \mathrm{e}^-\bar{\nu}_\mathrm{e}\nu_\tau$ decays accompanied by a photon conversion is significantly lower than for events possessing only a single charged track, this deficit of photon conversions in MC compared to data would cause a systematic shift to the branching ratio estimate. The MC prediction for the number of $\tau^- \to \mathrm{e}^-\bar{\nu}_\mathrm{e}\nu_\tau$ decays possessing

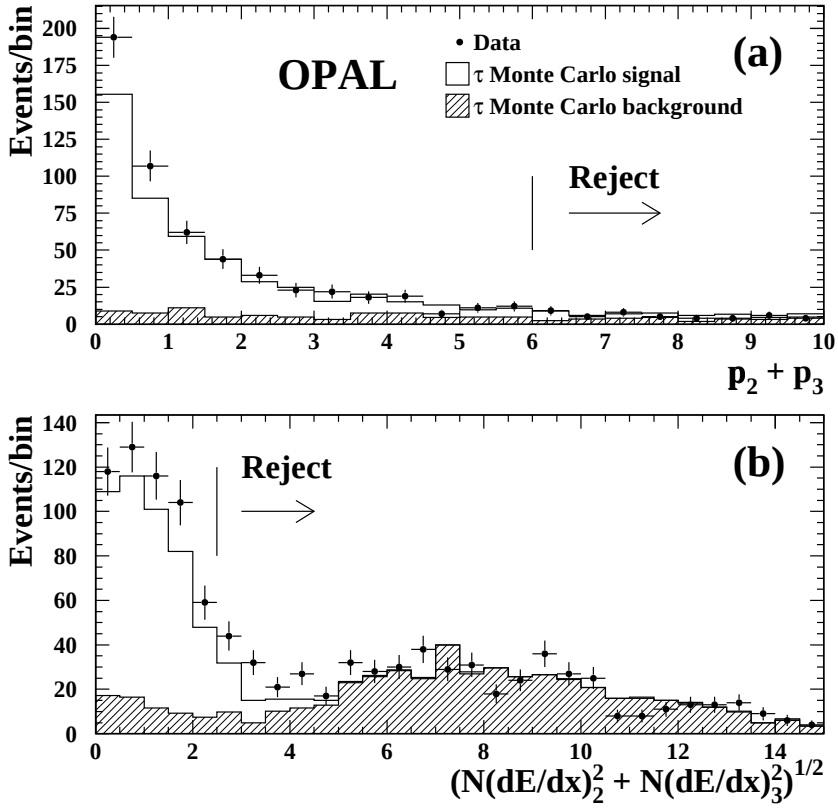

Figure 5.8: Scalar sum of the momenta of tracks other than the primary track (a), and the quadratic sum of the $N(\mathrm{d}E/\mathrm{d}x)$ of the second and third tracks (b), in decays which pass the nominal $\tau^- \to \mathrm{e}^-\bar{\nu}_\mathrm{e}\nu_\tau$ selection (see section 5.3). The excess of data over MC is consistent with photon conversions rather than to hadronic background, as discussed in the text.

$N_\mathrm{tracks} = 2$ ($N_\mathrm{tracks} = 3$) is therefore scaled by a factor of 1.3 (1.1) to give agreement with the data.

5.3 Likelihood selection

The sample of τ decays passing the preselection requirements described above is used as the basis for the $\tau^- \to \mathrm{e}^-\bar{\nu}_\mathrm{e}\nu_\tau$ likelihood selection. This sample consists of approximately 16% hadronic τ decays, with the remainder being $\tau^- \to \mathrm{e}^-\bar{\nu}_\mathrm{e}\nu_\tau$

events. The contamination in this sample from $\tau^- \to \mu^-\bar{\nu}_\mu\nu_\tau$ decays is negligible. The likelihood selection uses MC simulated τ decays to estimate the Bayesian posterior probability $P(t|X)$ that a real τ jet represents a particular τ decay mode t given measurements of a set of n uncorrelated kinematic variables $X \equiv \{x_1, x_2, ..., x_n\}$. This probability is given by

$$P(t|X) = \frac{P(X|t)P(t)}{P(X)} \tag{5.7}$$

where $P(t)$ is the prior probability and $P(X|t) = \prod_{i=1}^{n} P(x_i|t)$ is the likelihood function. The dependence on the quantity $P(X)$ can be removed by dividing this expression by $\sum_t P(t|X) = 1$ using the completeness property, as described in Appendix A. Because the primary track of background events in this sample is almost exclusively produced by a $\pi^\pm$, the likelihood selection does not need to discriminate between various hadronic τ decay channels. All jets which pass the preselection can therefore be classified generically as either $\tau^- \to \mathrm{e}^-\bar{\nu}_\mathrm{e}\nu_\tau$ decays or $\tau^- \to \pi^-(\geq 0\pi^0)\nu_\tau$ decays, so that only two decay "types" need to be considered. In this case the posterior probability $P(e|X)$ can be expressed as

$$P(e|X) \equiv 1 - P(\bar{e}|X) = \frac{P(e) \cdot P(X|e)}{P(e) \cdot P(X|e) + [1 - P(e)] \cdot P(X|\bar{e})} \quad . \tag{5.8}$$

The $\tau^- \to \mathrm{e}^-\bar{\nu}_\mathrm{e}\nu_\tau$ selection is therefore accomplished by constructing the posterior probability estimator $P(e|X)$ that a preselected event represents a $\tau^- \to \mathrm{e}^-\bar{\nu}_\mathrm{e}\nu_\tau$ decay, and then rejecting all events which possess $P(e|X)$ less than some value.

The likelihood distributions $P(X|e)$ and $P(X|\bar{e})$ are constructed using reference histograms obtained from MC simulation of the six selection variables N_{neut}, N_{HCAL}, $N(\mathrm{d}E/\mathrm{d}x)$, $N(E/p)$, $N(\Delta\theta)$ and $N(\Delta\phi)$. The two track-cluster matching variables $N(\Delta\theta)$ and $N(\Delta\phi)$ are plotted in figure 5.9 for τ decays which pass the preselection

requirements. The use of normalized variables implies that the selection variable reference distributions for $\tau^- \to \mathrm{e}^-\bar{\nu}_\mathrm{e}\nu_\tau$ decays are effectively independent of the track momentum, however the background $\tau^- \to \pi^-(\geq 0\pi^0)\nu_\tau$ reference distributions remain momentum dependent. Reference histograms are therefore constructed in the three momentum bins $p \leq 5$ GeV, $5 < p \leq 20$ GeV and $p > 20$ GeV. The full set of reference histograms used in this analysis is plotted in Appendix A.

The probability that a preselected jet represents a $\tau^- \to \mathrm{e}^-\bar{\nu}_\mathrm{e}\nu_\tau$ decay is computed using equation 5.8. Jets which fail any of the preselection or photon conversion requirements are assigned a probability $P(X|e) = 0$, that is, a zero probability of being a $\tau^- \to \mathrm{e}^-\bar{\nu}_\mathrm{e}\nu_\tau$ decay. If a jet does not possess well-measured values of all likelihood selection variables, it is not automatically rejected. Instead, the posterior probability is computed using the remaining variables. This can occur in the following situations:

- if the track possesses less than 20 isolated CJ hits (no $N(\mathrm{d}E/\mathrm{d}x)$ measurement)
- if there is no cluster associated to the primary track (no $N(E/p)$ measurement)
- if there is no CZ measurement for the track, leading to poor track position reconstruction in the θ direction (no $N(\Delta\theta)$ measurement)
- if $p < 5.0$ GeV (no $N(\Delta\theta)$ and $N(\Delta\phi)$ measurements)

Jets are required to possess a measurement of at least one of $N(E/p)$ or $N(\mathrm{d}E/\mathrm{d}x)$ to ensure that there is sufficient information for the selection.

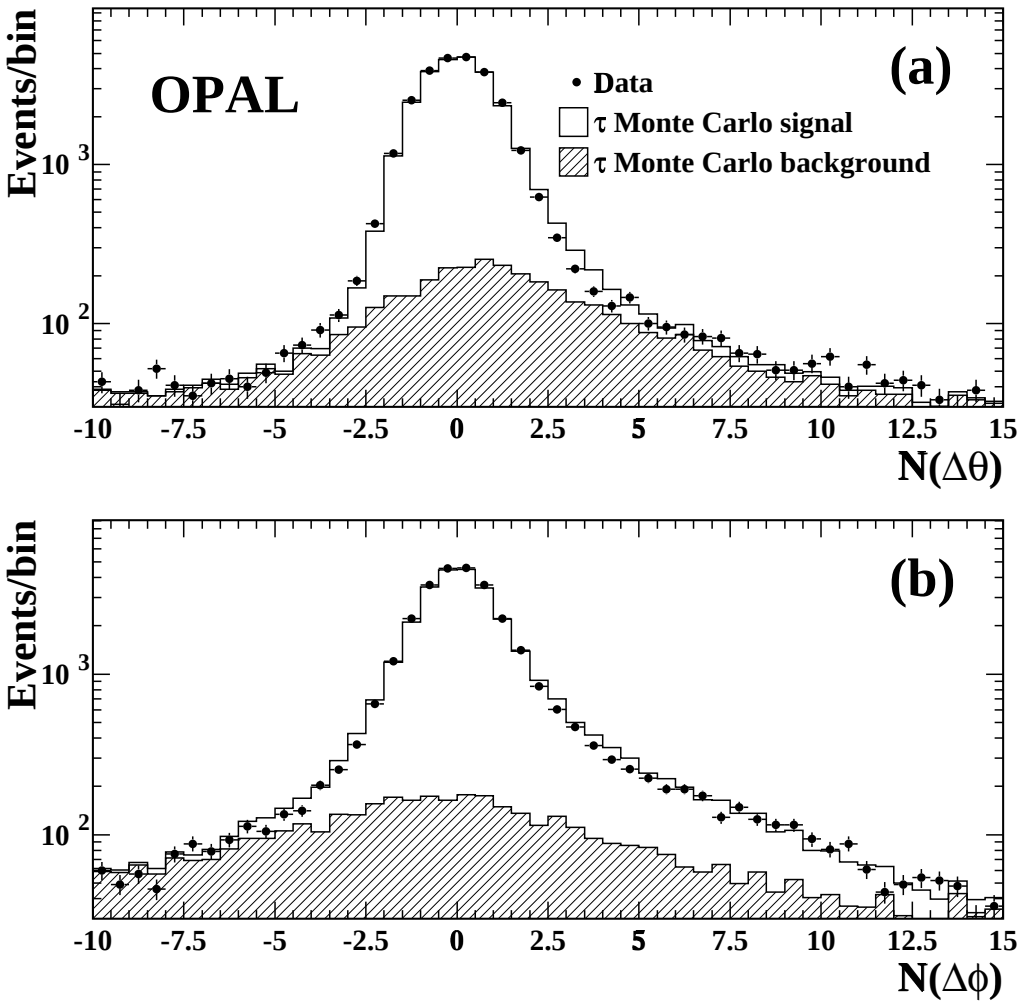

Figure 5.9: Data and MC simulation of the two normalized track-cluster matching variables (a) $N(\Delta\theta)$ and (b) $N(\Delta\phi)$ for jets passing the preselection.

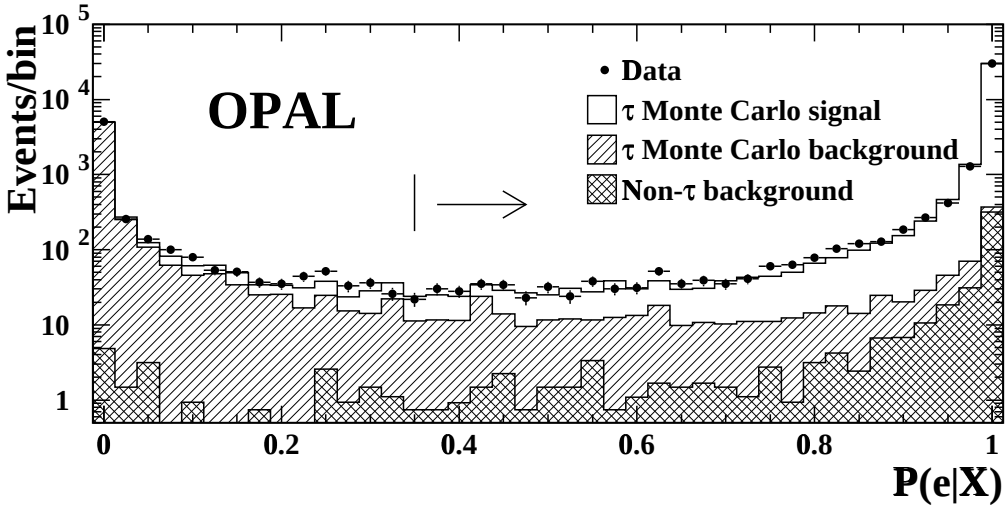

Figure 5.10: The likelihood selection variable $P(e|X)$ is plotted for all jets in the τ sample which pass the preselection. The $\tau^- \to \mathrm{e}^-\bar{\nu}_\mathrm{e}\nu_\tau$ candidate sample is composed of all jets in this plot with $P(e|X) > 0.35$ as indicated by the arrow. The MC predictions for the backgrounds in this sample from τ and non-τ sources are indicated.

5.4 The $\tau^- \to \mathrm{e}^-\bar{\nu}_\mathrm{e}\nu_\tau$ candidate sample

The posterior probability estimator $P(e|X)$ is plotted in figure 5.10 for all jets in the τ sample which survive the preselection requirements. The contributions to this sample from τ hadronic decays and from non-τ events, described in the following section, are also shown. The likelihood selection is accomplished by applying a cut on $P(e|X)$, however, because the uncertainty associated with the MC modelling of the selection efficiency and the backgrounds in the $\tau^- \to \mathrm{e}^-\bar{\nu}_\mathrm{e}\nu_\tau$ candidate sample have a small dependence on the value of this cut. Its value was therefore optimized in order to minimize the total measurement uncertainty. Rejecting jets which have $P(e|X) \leq 0.35$ results in the selection of 33073 $\tau^- \to \mathrm{e}^-\bar{\nu}_\mathrm{e}\nu_\tau$ candidates from the τ jet sample. This sample is referred to as the $\tau^- \to \mathrm{e}^-\bar{\nu}_\mathrm{e}\nu_\tau$ candidate sample.

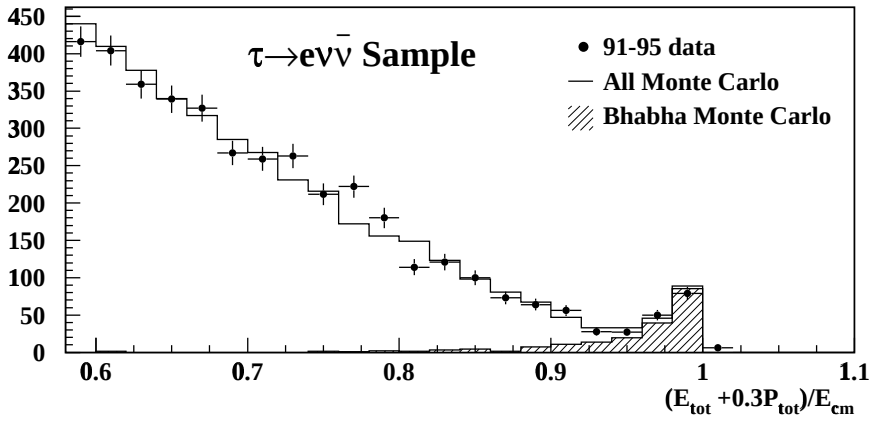

Figure 5.11: $(E_{\mathrm{tot}} + 0.3 \cdot p_{\mathrm{tot}})/E_{\mathrm{cm}}$ for events in which one jet has passed the $\tau^- \to \mathrm{e}^-\bar{\nu}_\mathrm{e}\nu_\tau$ likelihood selection and the opposite jet has passed an electron tag.

5.5 Non-τ backgrounds

Non-τ events with electrons in the final state, such as $\mathrm{e}^+\mathrm{e}^- \to (\mathrm{e}^+\mathrm{e}^-)\mathrm{e}^+\mathrm{e}^-$ and Bhabha events, sufficiently resemble $\tau^- \to \mathrm{e}^-\bar{\nu}_\mathrm{e}\nu_\tau$ decays that they constitute a significant background in the $\tau^- \to \mathrm{e}^-\bar{\nu}_\mathrm{e}\nu_\tau$ candidate sample. These background contributions to the $\tau^- \to \mathrm{e}^-\bar{\nu}_\mathrm{e}\nu_\tau$ candidate sample were evaluated using similar methods as were used for the corresponding backgrounds in the τ sample (see section 4.3). Two-photon mediated $\mathrm{e}^+\mathrm{e}^- \to (\mathrm{e}^+\mathrm{e}^-)\mathrm{e}^+\mathrm{e}^-$ events which pass the τ selection are accepted with effectively 100% efficiency by the $\tau^- \to \mathrm{e}^-\bar{\nu}_\mathrm{e}\nu_\tau$ selection The background in the $\tau^- \to \mathrm{e}^-\bar{\nu}_\mathrm{e}\nu_\tau$ sample from these events was evaluated by examining the acollinearity distribution of events in which both jets pass the $\tau^- \to \mathrm{e}^-\bar{\nu}_\mathrm{e}\nu_\tau$ selection, as shown in figure 4.6, and was estimated to to be $(0.59 \pm 0.07)\%$. The background from the two-photon mediated $\mathrm{e}^+\mathrm{e}^- \to (\mathrm{e}^+\mathrm{e}^-)\tau^+\tau^-$ channel is estimated from MC to contribute at the level of $\sim 0.03\%$, with a negligible uncertainty. The background contribution due to Bhabha events was evaluated by requiring a single track in the

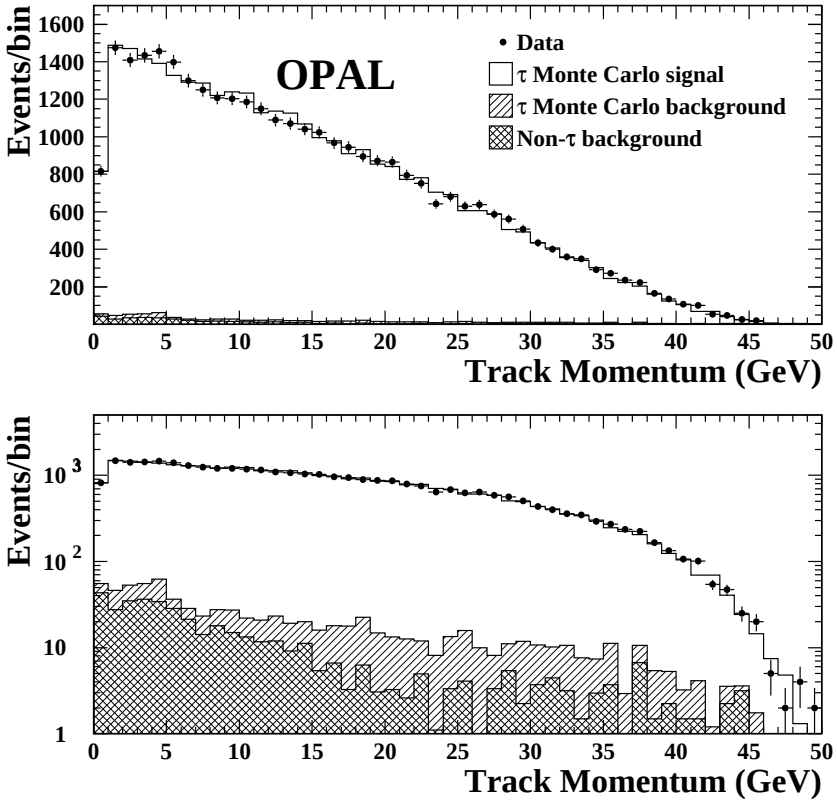

Figure 5.12: The momentum of the primary track is plotted for jets which pass the $\tau^- \to \mathrm{e}^-\bar{\nu}_\mathrm{e}\nu_\tau$ selection. The MC predictions for the backgrounds in this sample from τ and non-τ sources are indicated.

opposite jet which is tagged as an electron using $\mathrm{d}E/\mathrm{d}x$. The likelihood selection was then applied to the first jet, and the background was estimated from the distribution of $(E_\mathrm{tot} + 0.3p_\mathrm{tot})/E_\mathrm{cm}$ as shown in figure 5.11, to give $(0.67 \pm 0.10)\%$. Combining these estimates gives a total background in the $\tau^- \to \mathrm{e}^-\bar{\nu}_\mathrm{e}\nu_\tau$ sample of $f^{\mathrm{non}-\tau}_{\tau\to\mathrm{e}\bar{\nu}\nu} = (1.29 \pm 0.12)\%$. The contribution from all other non-τ sources discussed in section 4.3 is negligible. The momentum distribution of $\tau^- \to \mathrm{e}^-\bar{\nu}_\mathrm{e}\nu_\tau$ candidate jets is plotted in figure 5.12, and can be seen to be in good agreement with the Monte Carlo estimates of the τ and non-τ backgrounds in this sample.

Chapter 6

Branching ratio measurement

The $\tau^- \to e^- \bar{\nu}_e \nu_\tau$ branching ratio is evaluated using the expression

$$B(\tau^- \to e^- \bar{\nu}_e \nu_\tau) = \left(\frac{N_e}{N_\tau}\right) \cdot \left(\frac{1 - f^{\tau}_{\tau \to e\bar{\nu}\nu} - f^{non-\tau}_{\tau \to e\bar{\nu}\nu}}{(1 - f_\tau) \cdot \epsilon_e \cdot F_B}\right) \tag{6.1}$$

where N_e and N_τ are the number of selected $\tau^- \to e^- \bar{\nu}_e \nu_\tau$ candidates and the number of τ candidate jets respectively, ϵ_e is the efficiency for selecting $\tau^- \to e^- \bar{\nu}_e \nu_\tau$ decays from the τ candidate sample and $f^{\tau}_{\tau \to e\bar{\nu}\nu}$ is the fraction of the background in the $\tau^- \to e^- \bar{\nu}_e \nu_\tau$ sample from τ decays. The fractional non-τ backgrounds in the τ candidate sample and the $\tau^- \to e^- \bar{\nu}_e \nu_\tau$ candidate sample are given by f_τ and $f^{non-\tau}_{\tau \to e\bar{\nu}\nu}$ respectively, and F_B is the τ selection bias factor. The values of these quantities are summarized in table 6.1. The estimates of ϵ_e and $f^{\tau}_{\tau \to e\bar{\nu}\nu}$ are discussed in the following section. Substituting these values into equation 6.1 gives the result $B(\tau^- \to e^- \bar{\nu}_e \nu_\tau) = (17.806 \pm 0.089)\%$, where the quoted uncertainty is the statistical uncertainty given by the binomial error on the ratio (N_e/N_τ). Systematic uncertainties on this measurement are discussed below.

Quantity	Value
N_{e}	33073
N_{τ}	186197
F_{B}	1.0009 ± 0.0019
f_{τ}	$(1.26 \pm 0.07)\%$
$f^{\mathrm{non}-\tau}_{\tau\to \mathrm{e}\bar{\nu}\nu}$	$(1.29 \pm 0.12)\%$
ϵ_{e}	$(98.40 \pm 0.05)\%$
$f^{\tau}_{\tau\to \mathrm{e}\bar{\nu}\nu}$	$(1.21 \pm 0.04)\%$

Table 6.1: Values of quantities used in the calculation of $\mathrm{B}(\tau^- \to \mathrm{e}^-\bar{\nu}_{\mathrm{e}}\nu_{\tau})$. Note that the quoted uncertainties on ϵ_{e} and $f^{\tau}_{\tau\to \mathrm{e}\bar{\nu}\nu}$ are due only to Monte Carlo statistics.

6.1 Systematic Uncertainties

For the purposes of estimating systematic uncertainties it is appropriate to write equation 6.1 in a slightly different form. The background in the $\tau^- \to \mathrm{e}^-\bar{\nu}_{\mathrm{e}}\nu_{\tau}$ sample can be factored into components due to τ decays and to non-τ events, $(1 - f^{\tau}_{\tau\to \mathrm{e}\bar{\nu}\nu} - f^{\mathrm{non}-\tau}_{\tau\to \mathrm{e}\bar{\nu}\nu}) \simeq (1 - f^{\tau}_{\tau\to \mathrm{e}\bar{\nu}\nu}) \cdot (1 - f^{\mathrm{non}-\tau}_{\tau\to \mathrm{e}\bar{\nu}\nu})$, and equation 6.1 can be rewritten

$$\mathrm{B}(\tau^- \to \mathrm{e}^-\bar{\nu}_{\mathrm{e}}\nu_{\tau}) \simeq \left(\frac{N_{\mathrm{e}}}{N_{\tau}}\right) \cdot \left(\frac{1}{F_{\mathrm{B}}}\right) \cdot \left(\frac{1 - f^{\mathrm{non}-\tau}_{\tau\to \mathrm{e}\bar{\nu}\nu}}{(1 - f_{\tau})}\right) \cdot \left(\frac{1 - f^{\tau}_{\tau\to \mathrm{e}\bar{\nu}\nu}}{\epsilon_{\mathrm{e}}}\right) \quad . \tag{6.2}$$

This permits the expression for the branching ratio to be separated into components representing separate and uncorrelated contributions to the total measurement uncertainty. The first term in brackets contributes an uncertainty due only to data statistics as mentioned previously. The remaining three terms contribute systematic uncertainties which are ultimately due to MC modelling of different aspects of the selection procedure. The second term reflects the uncertainty in the τ MC modelling of the τ selection, the third term contains correlated uncertainties due to MC modelling of the non-τ backgrounds, and the final term reflects the correlated nature of the $\tau^- \to \mathrm{e}^-\bar{\nu}_{\mathrm{e}}\nu_{\tau}$ selection efficiency and background estimates.

The systematic uncertainty introduced by the bias factor estimate of $F_{\mathrm{B}} = 1.0009 \pm 0.0019$ from section 4.2 is obtained by propagation of errors, and contributes an uncertainty of 0.034% of the branching ratio measurement. Propagating the uncertainties given in table 6.1 for the two non-τ background estimates $f^{\mathrm{non}-\tau}_{\tau\to \mathrm{e}\bar{\nu}\nu}$ and f_τ gives a combined systematic uncertainty of 0.025% from these two sources. The non-τ backgrounds $f^{\mathrm{non}-\tau}_{\tau\to \mathrm{e}\bar{\nu}\nu}$ and f_τ are partially correlated since all non-τ backgrounds in the $\tau^- \to \mathrm{e}^-\bar{\nu}_\mathrm{e}\nu_\tau$ sample also contribute to the background in the τ sample, however this correlation turns out to have only a slight effect on the total systematic uncertainty.

The final term on the right hand side of equation 6.2 represents the systematic uncertainty due to MC modelling of the $\tau^- \to \mathrm{e}^-\bar{\nu}_\mathrm{e}\nu_\tau$ selection efficiency and the τ background in the $\tau^- \to \mathrm{e}^-\bar{\nu}_\mathrm{e}\nu_\tau$ sample. Since any change in MC modelling ultimately results in changes to the likelihood selection reference histograms, both the MC efficiency and background estimates will also change. If a change in MC modelling induces changes in ϵ_e and $f^{\tau}_{\tau\to \mathrm{e}\bar{\nu}\nu}$ in such a way that the branching ratio measurement is not affected, then no systematic uncertainty is introduced by this change. The quantity of interest for studies of systematic uncertainties is therefore the MC correction factor $(1 - f^{\tau}_{\tau\to \mathrm{e}\bar{\nu}\nu})/\epsilon_\mathrm{e}$ rather than the separate background and efficiency estimates. In the following section, the $\tau^- \to \mathrm{e}^-\bar{\nu}_\mathrm{e}\nu_\tau$ selection efficiency and τ background are estimated, and checks of MC modelling of these quantities are performed. Contributions to the branching ratio systematic uncertainty, however, are obtained only for the combined effect of modelling of $(1 - f^{\tau}_{\tau\to \mathrm{e}\bar{\nu}\nu})/\epsilon_\mathrm{e}$.

6.1.1 Background and efficiency estimates

The $\tau^- \to \mathrm{e}^-\bar{\nu}_\mathrm{e}\nu_\tau$ selection efficiency and the background due to τ decays were estimated from τ MC simulation to be $(98.40 \pm 0.05)\%$ and $(1.21 \pm 0.04)\%$ respec-

tively, where the quoted uncertainties are due to MC statistics only. The contributions to this background from various τ decays are $(0.48 \pm 0.03)\%$ from $\tau^- \to \pi^- \nu_\tau$, $(0.69 \pm 0.03)\%$ from $\tau^- \to \pi^- (\geq 1\pi^0)\nu_\tau$ and $(0.04 \pm 0.01)\%$ from other τ decays. The combined MC statistical uncertainties on these efficiency and τ-background estimates contribute an uncertainty of 0.015% to the branching ratio measurement. The branching ratio values used in the MC simulation for various τ decay modes are reweighted to the world average values [2] for the purpose of determining the τ background. This reweighting was found to have a negligible ($\sim$ 0.002%) effect on the resulting branching ratio measurement and no systematic uncertainty is assigned due to this effect. Similarly, the uncertainties in the measured values of the world average τ hadronic branching ratios for decay modes contributing to this background were found to introduce a neglegible uncertainty to the τ background estimate.

Monte Carlo modelling of the $\tau^- \to e^- \bar{\nu}_e \nu_\tau$ selection efficiency was checked in the high and low momentum range using control samples of Bhabha and two-photon $e^+e^- \to (e^+e^-)e^+e^-$ events. A pure sample of electron jets was obtained from Bhabha events by selecting low-multiplicity events with $E_{\rm tot} > 80$ GeV, $\theta_{\rm acol} < 0.75^\circ$ and requiring a tagged electron in the opposing jet. The full $\tau^- \to e^- \bar{\nu}_e \nu_\tau$ selection was then applied to this sample of jets and the efficiency was compared with that found using the Bhabha MC simulation. A similar check was performed at low momentum using two-photon $e^+e^- \to (e^+e^-)e^+e^-$ events selected by requiring $\theta_{\rm acol} > 20^\circ$ and a tagged electron in the opposite jet. The ratio of the data and MC efficiencies is plotted as a function of momentum in figure 6.1. The slightly lower efficiency seen in Bhabha data compared with MC at momenta $p < 40$ GeV is not of particular concern since these events represent electrons with significant radiation, and therefore possess E/p measurements which are extremely unlikely for $\tau^- \to e^- \bar{\nu}_e \nu_\tau$ decays and represent

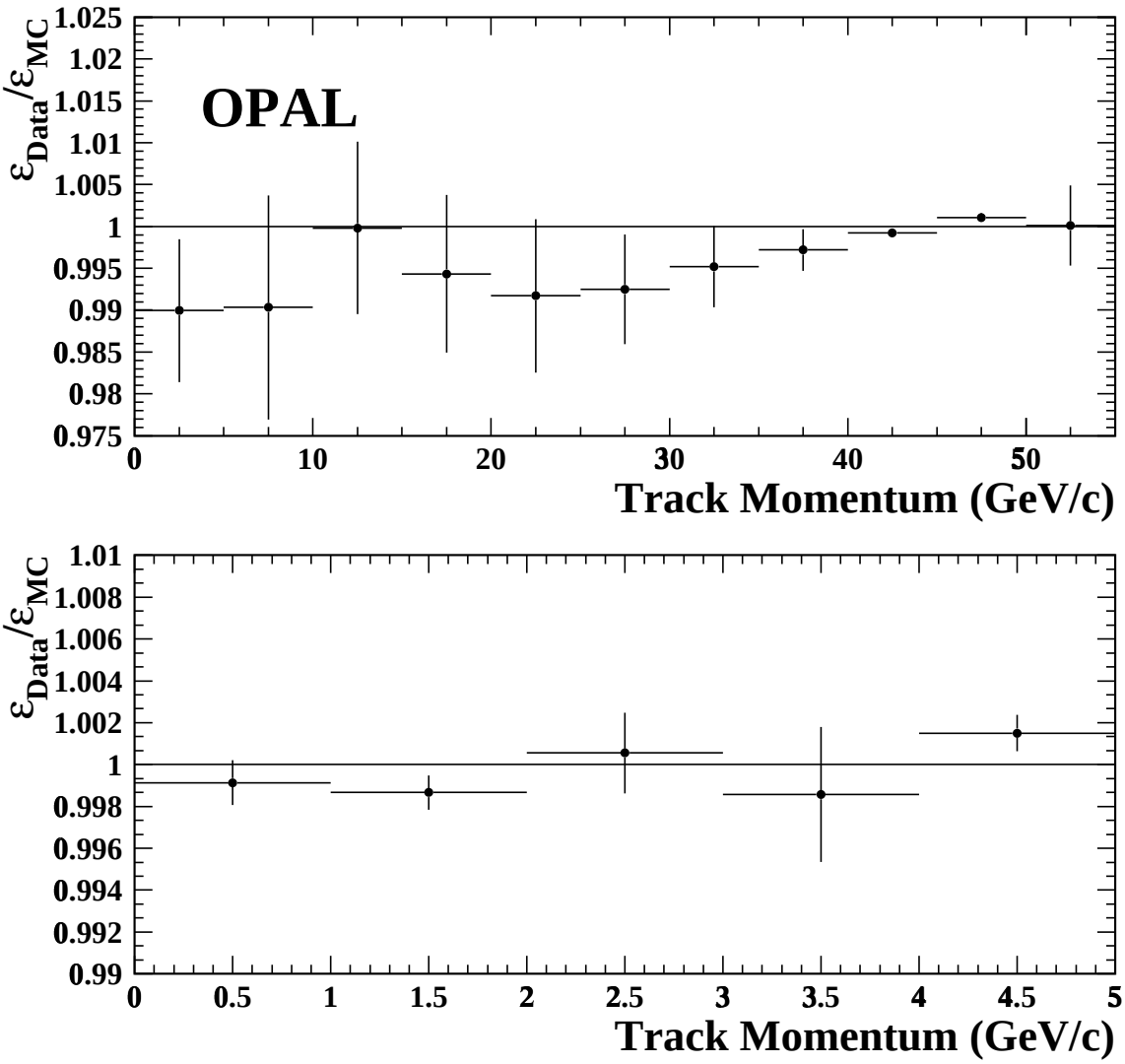

Figure 6.1: Comparison of the data and MC electron selection efficiency for control samples of Bhabha (top) and two-photon $e^+e^- \to (e^+e^-)e^+e^-$ (bottom) events. The ratio of the efficiencies is plotted as a function of the track momentum, and is consistent with unity over the entire momentum range.

only a small fraction of Bhabha decays. In both the Bhabha and two-photon data samples the overall efficiencies were found to be consistent with the MC simulation at the level of 0.06%.

The systematic uncertainty associated with the estimates of $\epsilon_{\rm e}$ and $f^{\tau}_{\tau\to {\rm e}\bar{\nu}\nu}$ due to MC modelling of the selection variables was evaluated by varying the means and widths of the four normalized variables $N({\rm d}E/{\rm d}x)$, $N(E/p)$, $N(\Delta\theta)$ and $N(\Delta\phi)$ around their central values, and measuring the corresponding variation in the branching ratio measurement. The appropriate ranges of variation for each variable were independently determined for $\tau^- \to {\rm e}^-\bar{\nu}_{\rm e}\nu_\tau$ decays and for background τ decays by comparison of MC and data distributions. The range of variation was chosen to reflect the largest observed discrepancy between data and simulation, or between distributions for the data collected in different years. The preselection and likelihood selection were applied to the MC samples with the mean and width parameters individually varied, and the selection efficiency and τ background were evaluated in each instance. The resulting shift in the measured branching ratio was determined independently for each varied parameter, and the quadratic sum of these shifts was used as an estimate of the systematic uncertainty. The effect of the modelling of the remaining two likelihood selection variables ($N_{\rm neut}$ and $N_{\rm HCAL}$) was estimated by varying the preselection cuts on these quantities. The systematic uncertainty due to MC modelling of the likelihood selection was estimated to be 0.031%.

An independent check of this systematic uncertainty associated with the likelihood selection was obtained by dropping each of the six selection variables in turn from the likelihood selection. The six probability estimators $P(e|X_{\bar{i}})$ were constructed, where $X_{\bar{i}}$ is the set of variables X used in the nominal likelihood selection but with the variable i excluded. The branching ratio was then evaluated for these

Selection	ΔB (%)
No $N_{\rm neut}$	-0.011
No $N_{\rm HCAL}$	$+0.037$
No $N(\mathrm{d}E/\mathrm{d}x)$	-0.002
No $N(E/p)$	-0.006
No $N(\Delta\theta)$	$+0.012$
No $N(\Delta\phi)$	-0.031

Table 6.2: Branching ratio shift $\Delta B \equiv B_{\bar{i}} - B_{\rm nominal}$ obtained using modified likelihood selections in which one of the six selection variables has been excluded.

six selections by applying the cut $P(e|X_{\bar{i}}) \geq 0.35$ to each of these estimators. The variation $\Delta B \equiv B_{\bar{i}} - B_{\rm nominal}$ of each of the six measurements from the branching ratio obtained with the nominal likelihood selection provides a measure of the MC modelling of the variable which has been dropped from the selection as well as of the remaining variables. The branching ratio shifts induced in this manner are given in table 6.2. It can be argued that the variance of these six values is a measure of the systematic uncertainty due to selection variable modelling [51], giving an uncertainty estimate of 0.023%. However, a more conservative estimate can be obtained by taking half the difference between the largest and smallest values in table 6.2. This gives an uncertainty estimate of 0.034% which is comparable to the value obtained by variation of the MC modelling parameters discussed above.

The systematic uncertainty introduced by MC modelling of photon conversions was evaluated by modifying the preselection cuts to reject jets possessing more than one track. This was found to introduce a shift of 0.005% to the measured branching ratio. Jets with up to three tracks were then re-admitted to the $\tau^- \to \mathrm{e}^-\bar{\nu}_\mathrm{e}\nu_\tau$ candidate sample but the momentum and $N(\mathrm{d}E/\mathrm{d}x)$ cuts on the second and third tracks were not applied. A significantly higher background and a slightly increased

Selection	ΔB (%)
$N_{\text{tracks}} = 1$	+0.005
No photon conversion id	+0.007
$N_{\text{ACl}} = 1$	+0.003
$N_{\text{HCAL}} = 0$	+0.011
$N_{\text{neut}} = 0$	+0.024

Table 6.3: The shift in the branching ratio measurement $\Delta B \equiv B_{\text{sel}} - B_{\text{nominal}}$ resulting from modifications to the $\tau^- \to e^- \bar{\nu}_e \nu_\tau$ preselection and photon conversion requirements.

$\tau^- \to e^- \bar{\nu}_e \nu_\tau$ selection efficiency were obtained, and the reconstructed branching ratio was found to shift by 0.007%. A systematic uncertainty of 0.010% is assigned to the branching ratio measurement as a result of these tests. The branching ratio shifts induced by checks on the preselection and photon conversion modelling are listed in table 6.3.

The preselection contributes to the systematic uncertainty through MC modelling of the preselection efficiency for $\tau^- \to e^- \bar{\nu}_e \nu_\tau$ decays. Modelling of the τ hadronic background in the sample of preselected events is of lesser importance since the likelihood selection tends to compensate for modelling of these cuts, and any residual effect is included in the systematic uncertainty associated with the likelihood selection. MC modelling of preselection variables was verified with data by comparing the variable distributions of selected and rejected jets in samples in which all preselection cuts were applied other than the cut under consideration. MC distributions of all preselection variables were found to agree with the equivalent distributions of data at the level of the available data statistics. Additional verification of modelling of the selection variables at high and low momentum was accomplished using Bhabha and two photon $e^+e^- \to (e^+e^-)e^+e^-$ events.

The N_{ACl} preselection cut produces the single largest loss of preselection efficiency ($\sim 0.2\%$). The number of tracks possessing no associated cluster is underestimated by the MC (see section 5.1.2) and a correction is applied to compensate for this deficit. The effect of this cut was examined for a possible systematic bias. The branching ratio was evaluated for a selection in which the requirement $N_{\mathrm{ACl}} = 1$ was added to the preselection so that the MC was forced to estimate the loss of efficiency due to tracks with no associated cluster. The branching ratio was found to shift by 0.003%, indicating that tracks with $p < 5$ GeV are well modelled. However, this test is not sensitive to tracks with $p \geq 5$ GeV and so these jets are included in the combined efficiency systematic uncertainty estimate below.

The high efficiency of the remaining preselection cuts (typically $> 99.9\%$) makes it difficult to individually check the efficiency of these cuts with data. The combined efficiency of all preselection cuts, other than those which are implicitly included in the selection variable modelling uncertainty and photon conversion cuts discussed above, was therefore evaluated and the uncertainty on the combined inefficiency was estimated. The combined efficiency of these cuts was estimated from MC to be $99.77 \pm 0.08\%$, where the dominant contribution is from the associated cluster requirement for tracks with $p > 5$ GeV. Propagating this uncertainty through the branching ratio calculation results in a contribution to the branching ratio systematic uncertainty of 0.015%.

6.1.2 Additional checks

Potential detector-related systematic biases to the branching ratio were evaluated by comparing the branching ratio measurements obtained in different regions of the detector or with different detector configurations. The parity invariance of the detector

Selection	ΔB (%)
Charge conjugation	± 0.023
Parity	± 0.045
$N_{\mathrm{dE/dxhits}} > 40$	$+0.002$
CZ acceptance	$+0.003$
Beam energy dependence	-0.007

Table 6.4: The shift in the branching ratio measurement $\Delta B \equiv B_{\mathrm{sel}} - B_{\mathrm{nominal}}$ resulting from modifications to the $\tau^- \to \mathrm{e}^- \bar{\nu}_\mathrm{e} \nu_\tau$ selection procedure.

was tested by comparing the branching ratio measurements obtained in the two hemispheres ($\cos\theta > 0$) and ($\cos\theta < 0$) of the detector. The charge dependence, and hence the assumption of invariance under charge conjugation, was checked by comparing the branching ratio measurement for $\tau^- \to \mathrm{e}^- \bar{\nu}_\mathrm{e} \nu_\tau$ decays and $\tau^+ \to \mathrm{e}^+ \nu_\mathrm{e} \bar{\nu}_\tau$ decays. In both of these cases the branching ratio variation was well within the expected data statistical uncertainty of $\pm 0.12\%$. These results are listed in table 6.4. The effect of the $\mathrm{d}E/\mathrm{d}x$ quality requirement of $N_{\mathrm{dE/dxhits}} > 20$ was tested by increasing the threshold to require > 40 $\mathrm{d}E/\mathrm{d}x$ hits for the $\mathrm{d}E/\mathrm{d}x$ to be considered well measured. This was found to have negligible effect on the branching ratio measurement.

The CZ detector has two small regions, corresponding to approximately 7% of the geometrical acceptance, which were inoperative for part of the data collection period. The τ MC modelled these regions as if they were inoperative for the entire data collection period, leading to a slight difference in CZ acceptance between data and MC. Since a CZ measurement is required for the likelihood selection variable $N(\Delta\theta)$ to be used, it was necessary to determine if the CZ acceptance introduces a measurement bias. The sensitivity of the branching ratio determination to the MC modelling of this effect was evaluated by reconstructing the branching ratio excluding

data with tracks which pass through the geometrical regions possessing an inoperative CZ detector. The shift induced in the branching ratio measurement was found to be 0.003%, which is neglegible.

The selection efficiency and background estimates obtained from MC simulation were found to have a slight dependence on the modelled centre-of-mass energy. The distribution of beam energies around the Z^0 peak was approximated in the data simulation by including appropriately scaled contributions from the off-peak MC runs 1535 and 1537. The systematic uncertainty introduced by the beam energy dependence was estimated by the size of the resulting shift in the measured branching ratio when the off-peak MC runs were dropped from the simulation. The observed shifts were ~ 0.01 and are consistent with the MC statistical uncertainty. Therefore, no additional systematic uncertainty is assigned to the branching ratio measurement due to this effect.

As a final cross check of the uncertainty estimates discussed above, the likelihood selection cut was varied over the range $0. < P(e|X) < 1.0$ and the branching ratio result was evaluated at each value of this cut. The branching ratio is plotted as a function of the $P(e|X)$ value in figure 6.2. After correcting for the contribution from non-τ backgrounds, the branching ratio was found to be consistent with the systematic uncertainty from MC modelling and non-τ backgrounds over most of the range of possible cuts. Significant deviations from the nominal branching ratio are observed only for $P(e|X)$ cuts greater than 0.8, and are explainable since the MC correction factor $(1 - f^{\tau}_{\tau\to e\bar{\nu}\nu})/\epsilon_e$ varies rapidly with $P(e|X)$ in this region, and therefore the selection is very sensitive to MC modelling in this region. The lack of sensitivity to the selection cut value in the vicinity of the nominal cut is an indication that the $P(e|X)$ cut is well modelled by MC.

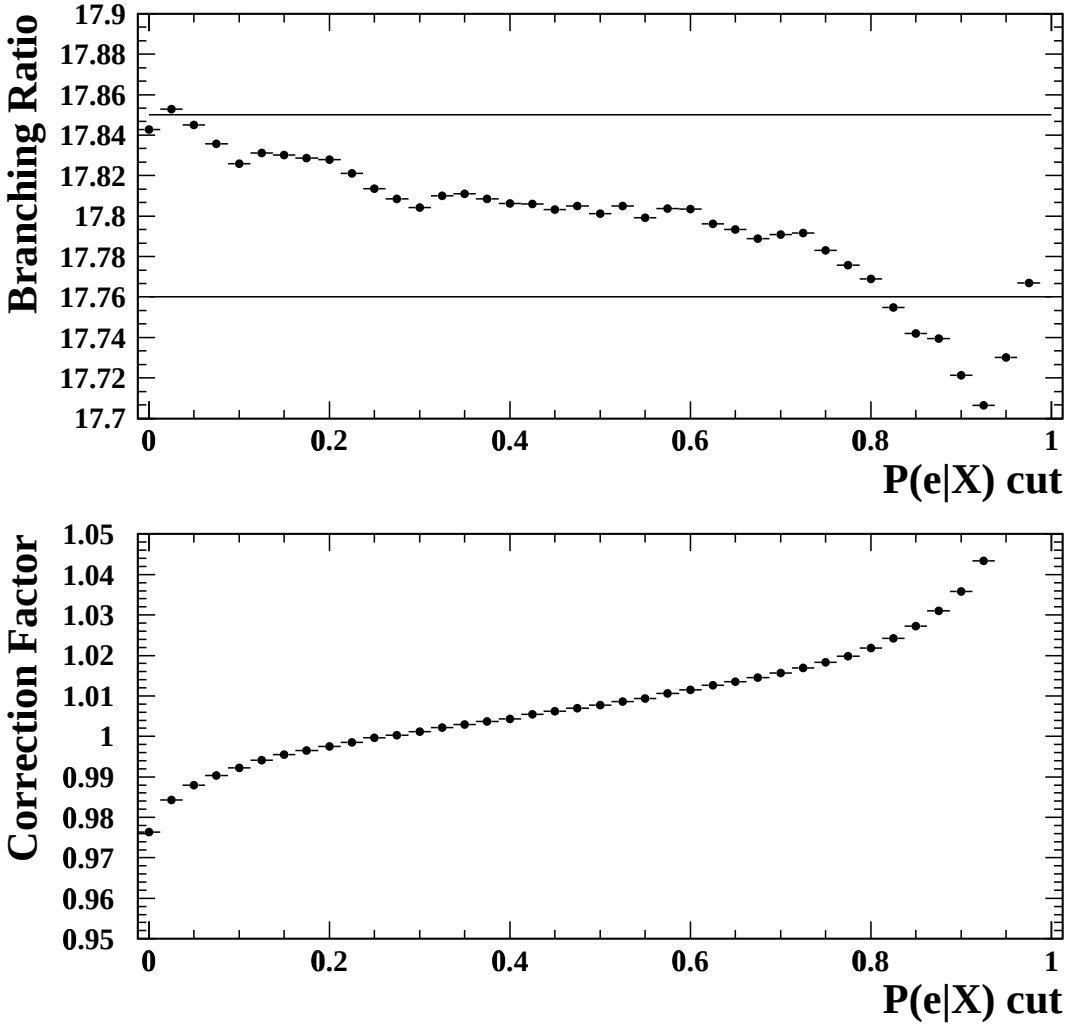

Figure 6.2: The $\tau^- \to e^- \bar{\nu}_e \nu_\tau$ branching ratio measurement is plotted as a function of the $P(e|X)$ likelihood selection cut (top). The lines represent the MC modelling and non-τ background uncertainties evaluated with a likelihood cut of $P(e|X) \leq 0.35$. The MC efficiency and background correction factor $(1 - f^{\tau}_{\tau \to e\bar{\nu}\nu})/\epsilon_e$ is plotted as a function of the $P(e|X)$ cut (bottom). The large slope of this function at large $P(e|X)$ cut values results in a large sensitivity to MC modelling for these cut values.

Source	Uncertainty (%)
Bias factor	0.034
Non-τ backgrounds	0.025
Selection variable modelling	0.031
MC statistics	0.015
Photon conversions	0.010
Preselection	0.015
Total systematic uncertainty	0.057

Table 6.5: Contributions to the total branching ratio systematic uncertainty.

6.2 Branching ratio results

The systematic uncertainty estimates from the effects discussed above are summarized in table 6.5, and total 0.057%. Combining this uncertainty estimate with the branching ratio result from above gives the measurement

$$\mathrm{B}(\tau^- \to \mathrm{e}^- \bar{\nu}_\mathrm{e} \nu_\tau) = (17.81 \pm 0.09\ (\mathrm{stat}) \pm 0.06\ (\mathrm{syst}))\ \% \quad . \tag{6.3}$$

This result is the most precise measurement of $\mathrm{B}(\tau^- \to \mathrm{e}^- \bar{\nu}_\mathrm{e} \nu_\tau)$ to date, and is in good agreement with previous measurements of this quantity both by OPAL and by other experiments, as is shown in figure 6.3. In the following sections this branching ratio measurement is used to test the universality of electroweak charged-current couplings to leptons and to obtain a value of the strong coupling constant α_s.

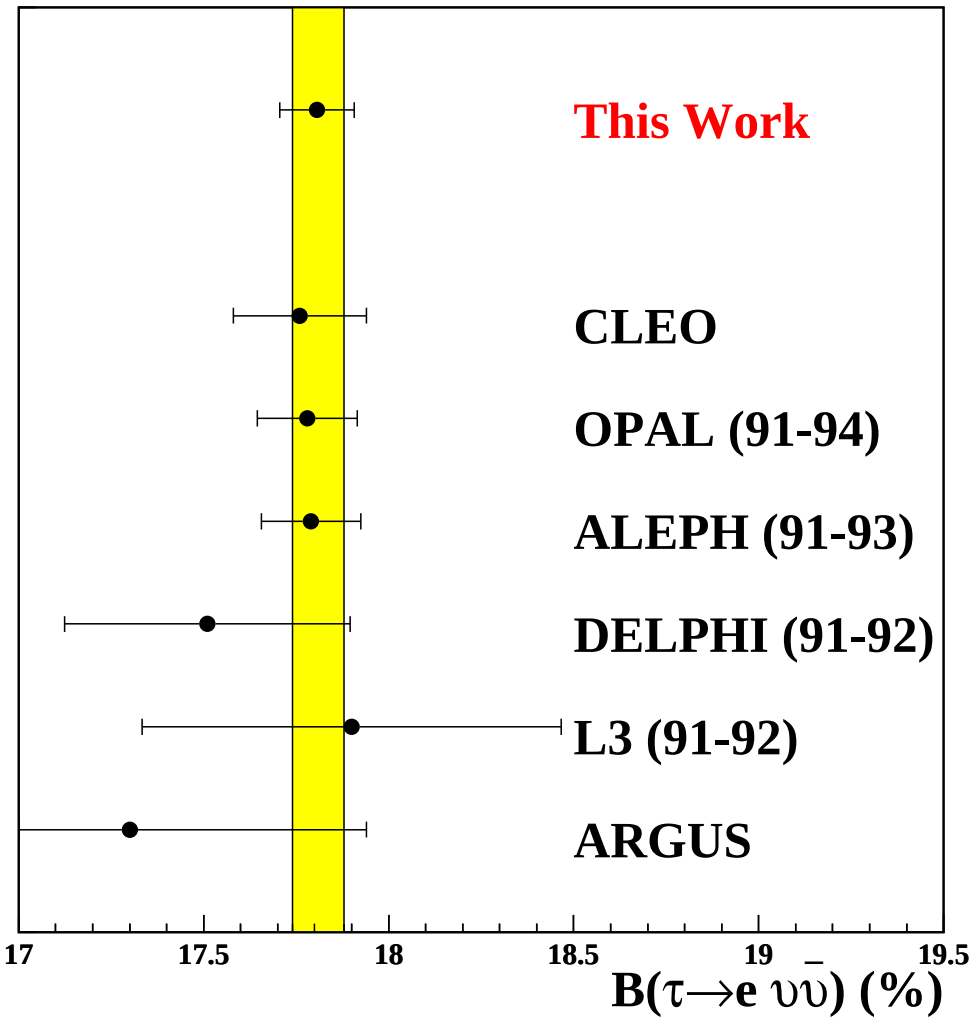

Figure 6.3: The $B(\tau^- \to e^- \bar{\nu}_e \nu_\tau)$ measurement from this analysis is compared with other measurements of this quantity. The band represents the PDG fit [2] to these measurements excluding the new result.

Chapter 7

Testing the Standard Model

Because the electroweak decays of leptons can be precisely calculated within the framework of the SM, leptonic τ decays can be used to test the SM assumption of the universality of the $W^{\pm}$ couplings to the three lepton generations. Furthermore, since the τ lepton is sufficiently massive to decay hadronically, it can also be used to probe the strong interaction. The decay $\tau^- \rightarrow e^- \bar{\nu}_e \nu_\tau$ can be used to test QCD predictions at the comparatively low energy scale of the τ mass, in an experimentally clean environment. These tests are presented in the following sections.

7.1 Lepton universality

The SM assumption of lepton universality implies that the weak gauge bosons Z^0 and $W^{\pm}$ couple to the three lepton generations with the same strength. Leptonic decays proceed via the $W^{\pm}$ in a manner which is precisely calculable within the SM, thus permitting this assumption to be tested in the charged-current sector. Two tests of lepton universality can be made using the $\tau^- \rightarrow e^- \bar{\nu}_e \nu_\tau$ branching ratio measurement presented in this work, by comparing this result with measurements of other leptonic branching ratios and lifetimes. These tests are described in section 2.3, and the experimental results are presented in the following sections.

7.1.1 μ - e universality

The ratio of g_μ/g_e can be evaluated by comparing the τ leptonic partial widths to electrons and muons from equation 2.7. Expressed in terms of the leptonic branching ratios, this gives

$$\left(\frac{g_\mu}{g_\mathrm{e}}\right)^2 = \frac{\mathrm{B}(\tau^- \to \mu^- \bar{\nu}_\mu \nu_\tau)}{\mathrm{B}(\tau^- \to \mathrm{e}^- \bar{\nu}_\mathrm{e} \nu_\tau)} \cdot \frac{f(m_\mathrm{e}^2/m_\tau^2)}{f(m_\mu^2/m_\tau^2)} \quad . \tag{7.1}$$

The phase space correction factors for the masses of the electron and muon have the values $f(m_\mathrm{e}^2/m_\tau^2) \simeq 1$ and $f(m_\mu^2/m_\tau^2) = 0.9726$. By substituting the preliminary OPAL measurement of the $\tau^- \to \mu^- \bar{\nu}_\mu \nu_\tau$ branching ratio of $(17.48 \pm 0.12 \pm 0.08)\%$ [52] and the $\mathrm{B}(\tau^- \to \mathrm{e}^- \bar{\nu}_\mathrm{e} \nu_\tau)$ measurement from this analysis into equation 7.1, the ratio of the coupling constants is found to be $g_\mu/g_\mathrm{e} = 1.0046 \pm 0.0051$. Alternatively, using the published OPAL $\tau^- \to \mu^- \bar{\nu}_\mu \nu_\tau$ branching ratio measurement $(17.36 \pm 0.27)\%$ [53], one obtains $g_\mu/g_\mathrm{e} = 1.0011 \pm 0.0083$. In both cases the result is in good agreement with the hypothesis of μ - e universality.

Although the most precise measurements of g_μ/g_e are from $\pi \to l\bar{\nu}$ decays (where $l = \mathrm{e}, \mu$) [54, 55], the results using leptonic τ decays are complimentary, since the semileptonic measurements are only sensitive to the longitudinal (helicity 0) couplings of the $\mathrm{W}^\pm$, while the tests from τ decays are also sensitive to the transverse (helicity ± 1) couplings.

7.1.2 τ - μ universality

A test of τ - μ universality can be made by comparing the partial widths for $\tau^- \to \mathrm{e}^- \bar{\nu}_\mathrm{e} \nu_\tau$ and $\mu^- \to \mathrm{e}^- \bar{\nu}_\mathrm{e} \nu_\mu$ decays. The ratio of the couplings g_τ and g_μ is obtained from equation 2.9 using the fact that the $\mu^- \to \mathrm{e}^- \bar{\nu}_\mathrm{e} \nu_\mu$ branching ratio is effectively 100%. Substituting numerical values for the $\mathrm{W}^\pm$ propagator and radiative correction factors

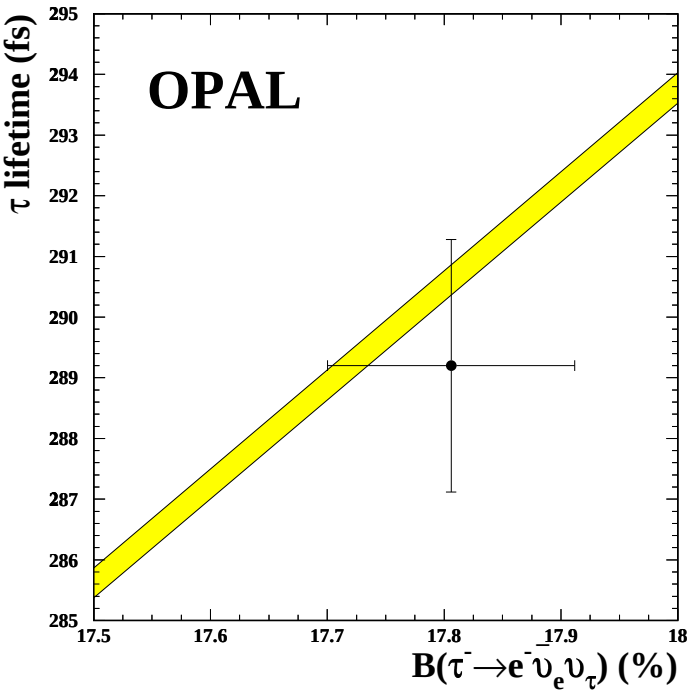

Figure 7.1: The OPAL τ lifetime is plotted against the $\tau^- \to \mathrm{e}^-\bar{\nu}_\mathrm{e}\nu_\tau$ branching ratio. The band is the Standard Model prediction under the assumption of lepton universality, and its width is represents the uncertainty due to the measured τ mass. Note that the range of the plotted y-axis is only 10 fs, of the x-axis is 0.5%, and that both measurements have a precision of $\sim 0.7\%$.

gives

$$\left(\frac{g_\tau}{g_\mu}\right)^2 = 0.9996 \, \frac{\tau_\mu}{\tau_\tau}\frac{m_\mu^5}{m_\tau^5} \, \mathrm{B}(\tau^- \to \mathrm{e}^-\bar{\nu}_\mathrm{e}\nu_\tau) \quad . \tag{7.2}$$

Using the most recent OPAL measurement of the τ lifetime ($289.2 \pm 1.7 \pm 1.2$ fs) [56], the BES Collaboration value for the τ mass (1777.0 ± 0.3 MeV/c^2) [57], and Particle Data Group values for the muon mass and lifetime [2], gives the result $g_\tau/g_\mu = 1.0025 \pm 0.0047$. Alternatively, this measurement can be presented in terms of the SM prediction for the τ lifetime given the measured $\tau^- \to \mathrm{e}^-\bar{\nu}_\mathrm{e}\nu_\tau$ branching ratio as shown in figure 7.1. This result is consistent with the SM assumption of τ - μ universality, and represents one of the most precise determinations of g_τ/g_μ to date.

7.2 Measurement of α_s

It was shown in section 2.4 that the strong coupling constant α_s can be measured using τ decays with comparatively small theoretical uncertainties due to non-perturbative effects [17, 18, 19, 20]. The experimental observable is the ratio R_τ of the hadronic width to the electronic width:

$$R_\tau \equiv \frac{\Gamma(\tau^- \to \text{hadrons } \nu_\tau)}{\Gamma(\tau^- \to \mathrm{e}^-\bar{\nu}_\mathrm{e}\nu_\tau)} \quad . \tag{7.3}$$

QCD corrections to the parton level prediction $R_\tau \simeq 3$ make an experimental measurement of R_τ sensitive to the value of the strong coupling constant $\alpha_s(m_\tau^2)$ at the τ mass scale (1.77 GeV). The perturbative and non-perturbative corrections are expressed by the Operator Product Expansion (OPE) [21] given by equations 2.19 and 2.20, and table 2.2.

Under the assumption of lepton universality, R_τ can be expressed in terms of the $\tau^- \to \mathrm{e}^-\bar{\nu}_\mathrm{e}\nu_\tau$ branching ratio only. Substituting the branching ratio result from section 6.2 into equation 2.22 gives an experimental measurement of R_τ:

$$R_\tau = \frac{1 - \mathrm{B}(\tau^- \to \mathrm{e}^-\bar{\nu}_\mathrm{e}\nu_\tau) \cdot (1.9726)}{\mathrm{B}(\tau^- \to \mathrm{e}^-\bar{\nu}_\mathrm{e}\nu_\tau)} = 3.642 \pm 0.033 \quad . \tag{7.4}$$

A value of $\alpha_s(m_\tau^2)$ is extracted using equations 2.19 and 2.20, yielding $\alpha_s(m_\tau^2) = 0.334 \pm 0.010$ (exp) ± 0.016 (theory). The QCD prediction for R_τ as a function of $\alpha_s(m_\tau^2)$ is plotted in figure 7.2, along with the theoretical uncertainties from the perturbative expansion and non-perturbative contributions, demonstrating the sensitivity of this measurement to $\alpha_s(m_\tau^2)$.

The experimental uncertainty on $\alpha_s(m_\tau^2)$ is obtained by varying R_τ within the quoted uncertainty range in equation 7.4. Contributions to the theoretical uncertainty are listed in table 7.1. The uncertainties introduced by the K_4 coefficient, the non-

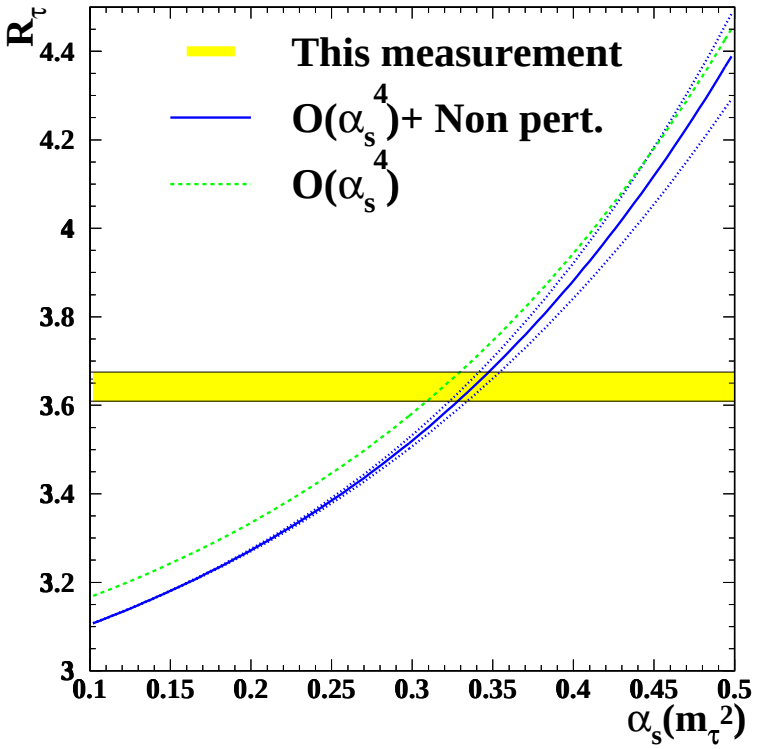

Figure 7.2: The QCD prediction from equation 2.19 for R_τ is plotted as a function of $\alpha_s(m_\tau^2)$ for the $D \geq 0$ terms quoted in the text (solid line). The uncertainty introduced by the perturbative $\mathcal{O}({\alpha_s}^4)$ coefficient (K_4) is indicated by the two dotted lines. The dashed line is the perturbative corrections only, illustrating the relative size of the non-perturbative corrections. The experimental value for R_τ is shown, giving an indication of the sensitivity of this method to $\alpha_s(m_\tau^2)$.

perturbative condensates and electroweak corrections were evaluated by varying the values of these terms in the OPE for R_τ and assessing the effect on the extracted value of $\alpha_s(m_\tau^2)$. The renormalization scheme (RS) dependence was estimated in [58] by evaluating the effect of changing from the $\overline{\text{MS}}$ scheme to a scheme using the principle of minimal sensitivity (PMS), while the renormalization scale dependence is taken from [27] and reflects a variation of the energy scale parameter μ in the range $\mu^2/m_\tau^2 \to 0.4 - 2.0$. The theoretical uncertainty on $\alpha_s(m_\tau^2)$ is dominated by the renormalization scheme and scale dependence.

Source	Uncertainty	$\Delta\alpha_s(m_\tau^2)$	$\Delta\alpha_s(m_{\rm Z}^2)$
Scale dependence	$\mu^2/m_\tau^2 \to 0.4 - 2.0$	0.009	0.0009
RS dependence	$\overline{\rm MS} \to$ PMS	0.010	0.0011
K_4 dependence	$K_4 = 25 \pm 50$	0.006	0.0007
$\delta^{(D)}$ corrections ($D \geq 2$)	-0.020 ± 0.004	0.004	0.0005
Electroweak corrections	1.0194 ± 0.0040	0.004	0.0005
Running $\alpha_s(m_\tau^2) \to \alpha_s(m_{\rm Z}^2)$	-	-	0.0003
Total theory uncertainty	-	0.016	0.0019

Table 7.1: Theoretical uncertainties on $\alpha_s(m_\tau^2)$ and $\alpha_s(m_{\rm Z}^2)$.

The value of $\alpha_s(m_\tau^2)$ is evolved to the Z^0 mass scale in order to compare it with other experimental results. Evolution of α_s is governed by the QCD β functions of the renormalization group (RG) equations:

$$\frac{da}{d\ln\mu^2} = \beta(a) = -a^2(\beta_0 + \beta_1 a + \beta_2 a^2 + \beta_3 a^3) + \mathcal{O}(a^6) \tag{7.5}$$

where $a \equiv \alpha_s/\pi$. The coefficients of $\beta(a)$ have recently been calculated up to four loops in the $\overline{\rm MS}$ scheme [59], resulting in a significant reduction in the theoretical uncertainties associated with this method.

Because effective field theories describing the dynamics of τ decays are usually constructed with $n_f = 3$ quark flavours, it is necessary to apply matching conditions which connect the parameters of the effective theory with the parameters of the theory with $n_f = 5$ appropriate at the Z^0 mass scale. Matching is performed at a scale $\mu_{\rm match} \sim \mathcal{O}(m_{\rm q})$ where $m_{\rm q}$ is a renormalization group invariant heavy quark mass. When appropriate matching conditions are taken into account, the evolution of α_s to higher energy scales is essentially independent of the choice of energy scale used to pass heavy quark thresholds. Details of the running and matching procedures

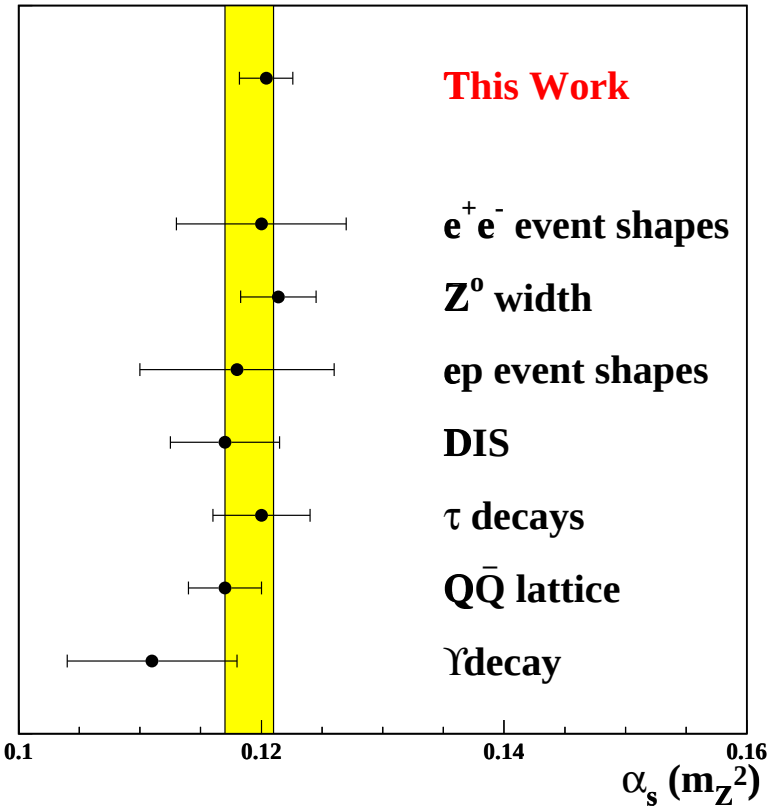

Figure 7.3: A comparison of various experimental measurements of $\alpha_s(m_Z^2)$ [2]. The shaded band represents the PDG world average value for $\alpha_s(m_Z^2)$. Note that the value of $\alpha_s(m_Z^2)$ from τ decays does not include the result from this analysis, or other recent τ measurements [26, 27].

can be found in Appendix B.

Following the procedure described in [60], running is performed at four-loops, with three-loop matching conditions used to pass the heavy quark mass thresholds. This procedure has been shown to introduce an uncertainty of 0.0003 to the extracted value of $\alpha_s(m_Z^2)$ [60], and can be summarized as follows. The measured value of $\alpha_s(m_\tau^2) \equiv \alpha_s^{(3)}(m_\tau^2)$ is evolved to a matching point $\mu_c \simeq m_c$ near the c quark mass (1.31 ± 0.06 GeV) using the renormalization group with $n_f = 3$ quark flavours.

$\alpha_s^{(4)}(\mu_c^2)$ is then obtained from $\alpha_s^{(3)}(\mu_c^2)$ using matching conditions at three loops. This result is then evolved with $n_f = 4$ to a new matching point $\mu_b \simeq m_b$ near the b quark mass (4.13 ± 0.06 GeV), where $\alpha_s^{(5)}(\mu_b^2)$ is evaluated from $\alpha_s^{(4)}(\mu_b^2)$. Finally, $\alpha_s(m_Z^2) \equiv \alpha_s^{(5)}(m_Z^2)$ is obtained from $\alpha_s^{(5)}(\mu_b^2)$ using the renormalization group with $n_f = 5$. Evolving the value of $\alpha_s(m_\tau^2)$ obtained above in this manner gives

$$\alpha_s(m_Z^2) = 0.1204 \pm 0.0011 \text{ (exp)} \ \pm 0.0019 \text{ (theory)} . \tag{7.6}$$

This result is in good agreement with other recent determinations [26, 27] of $\alpha_s(m_Z^2)$ based on exclusive measurements of τ hadronic spectral functions, and is one of the most precise measurements of this quantity to date. A comparison of this result with measurements of $\alpha_s(m_Z^2)$ using other methods is shown in figure 7.3. The consistency of this result with measurements of α_s obtained at other energy scales provides strong evidence for the applicability of perturbative QCD at the τ mass scale, and for the running of α_s through renormalization group evolution.

Chapter 8

Conclusions

Data collected by the OPAL experiment at LEP have been used to evaluate the branching ratio for the decay $\tau^- \to e^- \bar{\nu}_e \nu_\tau$. A selection procedure consisting of a cut-based preselection followed by a likelihood selection has been used to distinguish $\tau^- \to e^- \bar{\nu}_e \nu_\tau$ decays from other τ decay modes, based on measurements of kinematic variables in $Z^0 \to \tau^+ \tau^-$ events. A total of 33073 $\tau^- \to e^- \bar{\nu}_e \nu_\tau$ candidates were selected from a sample of 186197 τ jets, to give a branching ratio measurement of $B(\tau^- \to e^- \bar{\nu}_e \nu_\tau) = (17.81 \pm 0.09\ (\text{stat}) \pm 0.06\ (\text{syst}))\%$. This measurement has higher statistics and a significantly reduced systematic uncertainty compared with a previous OPAL measurement [49], and represents the most precise determination of this quantity to date.

Comparison of this measurement with other leptonic branching ratio and lifetime measurements allows the universality of the leptonic charged-current couplings, mediated by the $W^\pm$, to be tested at the level of 0.5%. The ratio of the coupling constants for muons and electrons was found to be $g_\mu/g_e = 1.0046 \pm 0.0051$, and for τ leptons and muons the ratio is $g_\tau/g_\mu = 1.0025 \pm 0.0047$. Both of these results are consistent with SM assumption of lepton universality, and show no evidence for non-SM physics.

The $\tau^- \to e^- \bar{\nu}_e \nu_\tau$ branching ratio can be used to deduce the inclusive τ hadronic

width, and hence the ratio $R_\tau = 3.642 \pm 0.033$. This result has been used to extract a measurement of the strong coupling constant α_s at the τ mass scale $\alpha_s(m_\tau^2) = 0.334 \pm 0.010$ (exp) ± 0.016 (theory). Evolving this measurement to the mass of the Z^0 boson gives $\alpha_s(m_Z^2) = 0.1204 \pm 0.0011$ (exp) ± 0.0019 (theory), which is one of the most precise determinations of this quantity which has been made at any energy scale.

Appendix A

Likelihood selection reference histograms

Likelihood selection reference histograms are constructed using MC τ jets which survive the τ selection (section 4.1) and the $\tau^- \to e^- \bar{\nu}_e \nu_\tau$ preselection cuts (section 5.2). This sample consists of approximately $\sim 84\%$ $\tau^- \to e^- \bar{\nu}_e \nu_\tau$ decays, with the remainder being background from τ hadronic decays. Reference histograms do not include contributions from non-τ events.

Dividing equation 5.7 by $\sum_t P(t|X) = 1$ and substituting equation 5.7 into the denominator gives

$$P(t|X) = \frac{\left(\frac{P(X|t)P(t)}{P(X)}\right)}{\sum_{t'}\left(\frac{P(X|t')P(t')}{P(X)}\right)} = \frac{P(X|t)P(t)}{\sum_{t'} P(X|t')P(t')} \quad . \tag{A.1}$$

Given a set of measurements $x_1, x_2, ..., x_n$, the likelihood $P(X|t)$ is given by the product of the conditional probabilities

$$P(X|t) = \prod_{i=1}^{n} P(x_i|t) \tag{A.2}$$

if and only if $P(x_i|t)$ are all mutually independent. The measurements $x_1, x_2, ..., x_n$ must therefore be uncorrelated for any given decay type t (note that $P(X) \neq \prod_{i=1}^{n} P(x_i)$ since the $P(x_i)$'s depend implicitly on the decay type t). Substituting into equa-

tion A.1 gives

$$P(t|X) = \frac{P(t)\prod_{i=1}^{n} P(x_i|t)}{\sum_{t'} P(t')\prod_{j=1}^{n} P(x_j|t')} \quad . \tag{A.3}$$

In the case of binned likelihood distributions, the quantities $P(x_i|t)$ depend explicitly on the bin width. Applying Bayes Law to the conditional probabilities on the RHS of equation A.3 and cancelling the "evidence" terms $P(x_i)$, allows this expression to be rewritten in a form that is independent of the binning used (see figure A.1):

$$P(t|X) = \frac{P(t)\prod_{i=1}^{n} \left(\frac{P(t|x_i)}{P(t)}\right)}{\sum_{t'} P(t')\prod_{j=1}^{n} \left(\frac{P(t'|x_j)}{P(t)}\right)} \quad . \tag{A.4}$$

The posterior probability $P(t|X)$ of an event representing a decay of type t is estimated for each τ jet based on a a set of measurements X. The likelihood is estimated from a set of reference histograms of the quantities $P(t|x_i)/P(t)$ which are obtained from Monte Carlo simulation of the decay types under consideration. In the present case, the only possible decay types are $\tau^- \to \mathrm{e}^-\bar{\nu}_\mathrm{e}\nu_\tau$ or τ background, labelled e and $\bar{e}$ respectively, and satisfying the relationships $P(e) = 1 - P(\bar{e})$, $P(e|x_i) = 1 - P(\bar{e}|x_i)$ and $P(e|X) = 1 - P(\bar{e}|X)$. The "prior" probability $P(e)$ is the fraction of $\tau^- \to \mathrm{e}^-\bar{\nu}_\mathrm{e}\nu_\tau$ decays within the preselected sample of τ decays, in the momentum bin under consideration, and is estimated from MC. Reference histograms are constructed from MC simulation of the distributions of the six selection variables N_{neut}, N_{HCAL}, $N(\mathrm{d}E/\mathrm{d}x)$, $N(E/p)$, $N(\Delta\theta)$ and $N(\Delta\phi)$ in the three momentum bins $P \leq 5.0$ GeV, $5.0 < P \leq 20.0$ GeV, and $P > 20.0$ GeV. The construction of these histograms is illustrated in figure A.1, the full set of reference histograms are plotted for signal and background in figures A.2 through A.7. The error bars on these histograms reflect MC statistics.

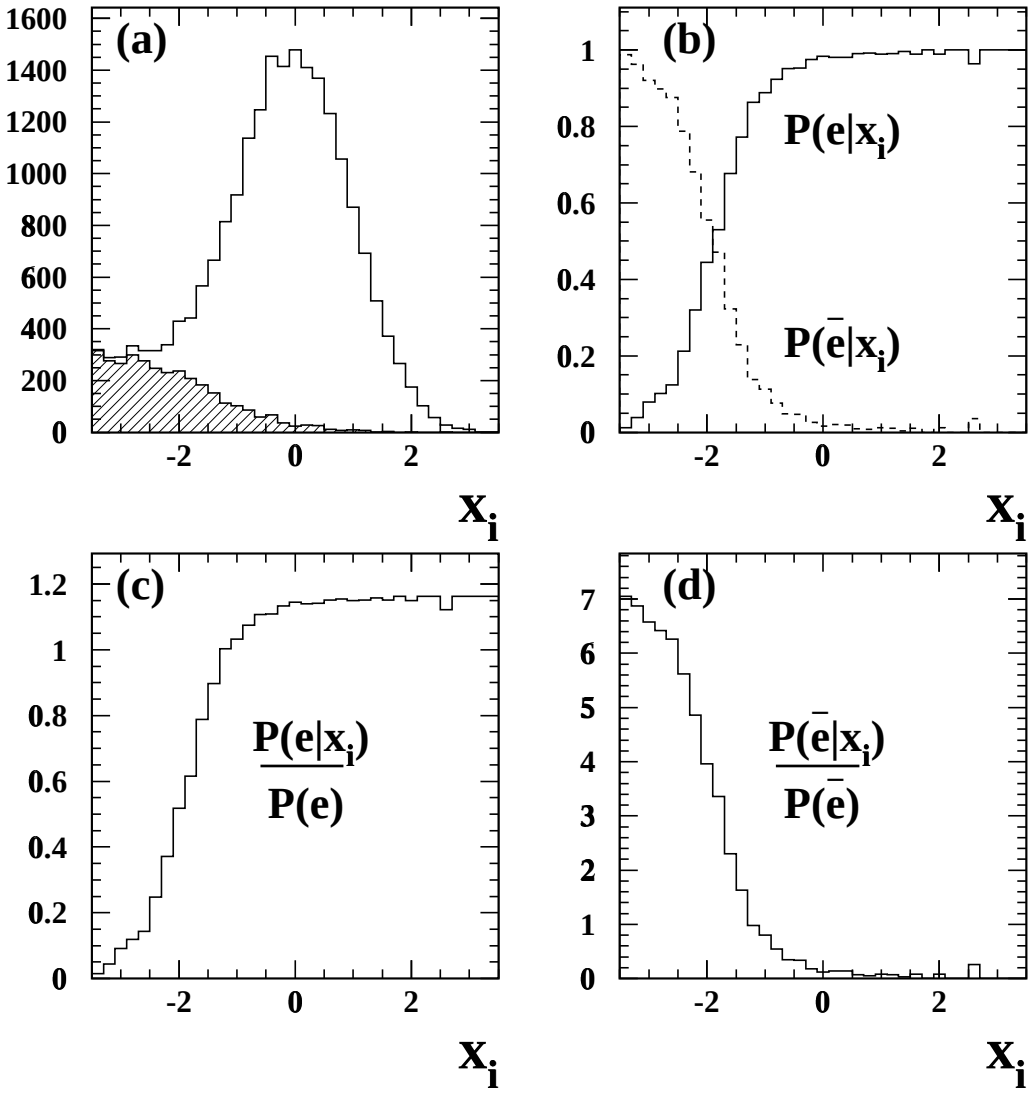

Figure A.1: Example of the construction of a likelihood selection reference histogram. (a) plots the distribution of signal (solid line) and background (shaded) of a selection variable x_i, and the resulting posterior probability distributions $P(e|x_i)$ and $P(\bar{e}|x_i)$ are shown in (b). The signal and background reference histograms for variable x_i are obtained by dividing these distributions by the prior probabilities $P(e)$ and $P(\bar{e})$ respectively, and are shown in (c) and (d). Because these histograms do not depend on $P(x_i)$, they are essentially independent of bin size.

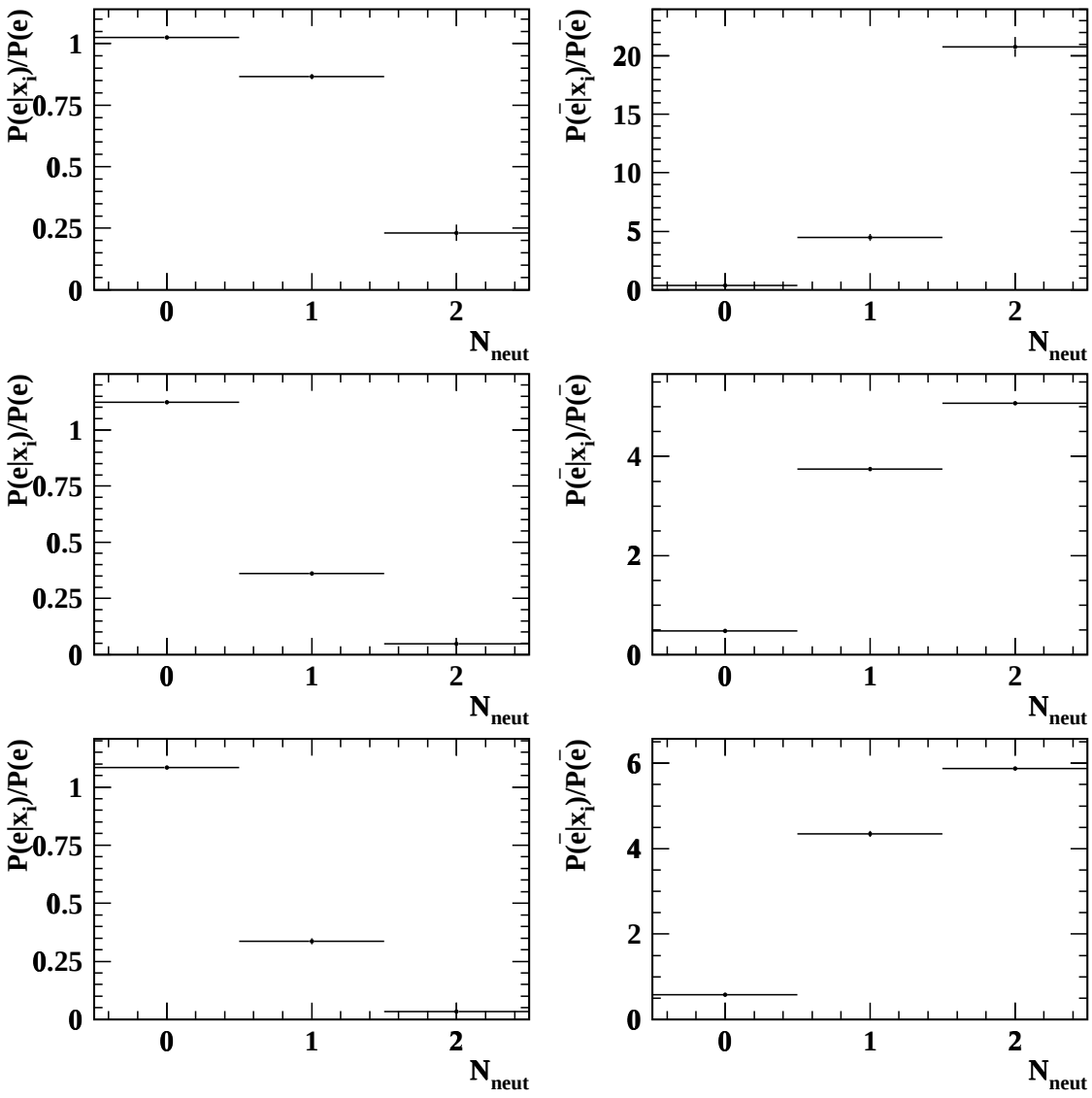

Figure A.2: Reference histograms for N_{neut} in the three momentum bins (top to bottom) $p \leq 5$ GeV, $5 < p \leq 20$ GeV and $p > 20$ GeV. The histograms on the left describe signal ($\tau^- \to \mathrm{e}^-\bar{\nu}_\mathrm{e}\nu_\tau$), while the histograms on the right describe the background from hadronic τ decays.

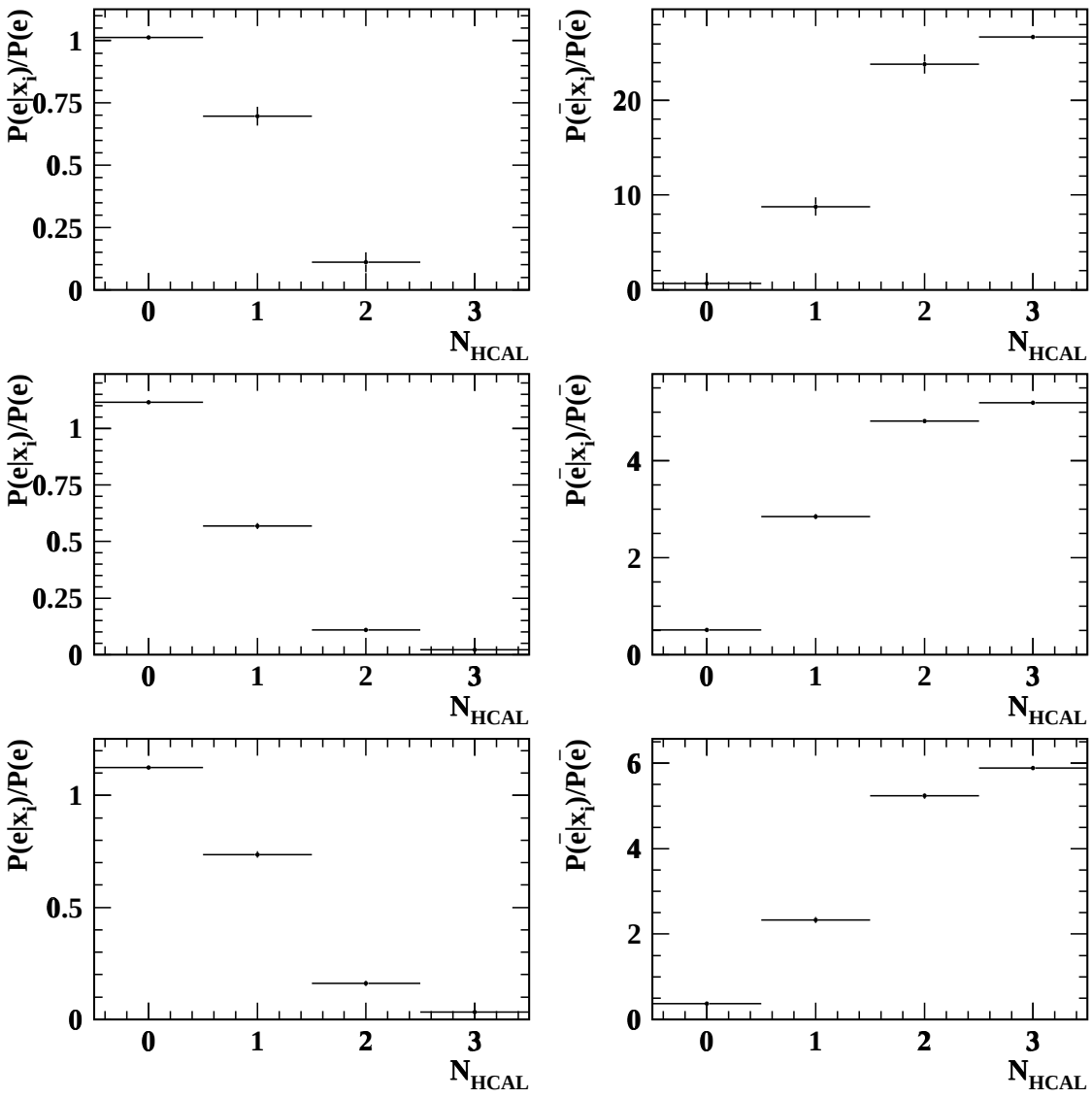

Figure A.3: Reference histograms for N_{HCAL} in the three momentum bins (top to bottom) $p \leq 5$ GeV, $5 < p \leq 20$ GeV and $p > 20$ GeV. The histograms on the left describe signal ($\tau^- \to \mathrm{e}^-\bar{\nu}_\mathrm{e}\nu_\tau$), while the histograms on the right describe the background from hadronic τ decays.

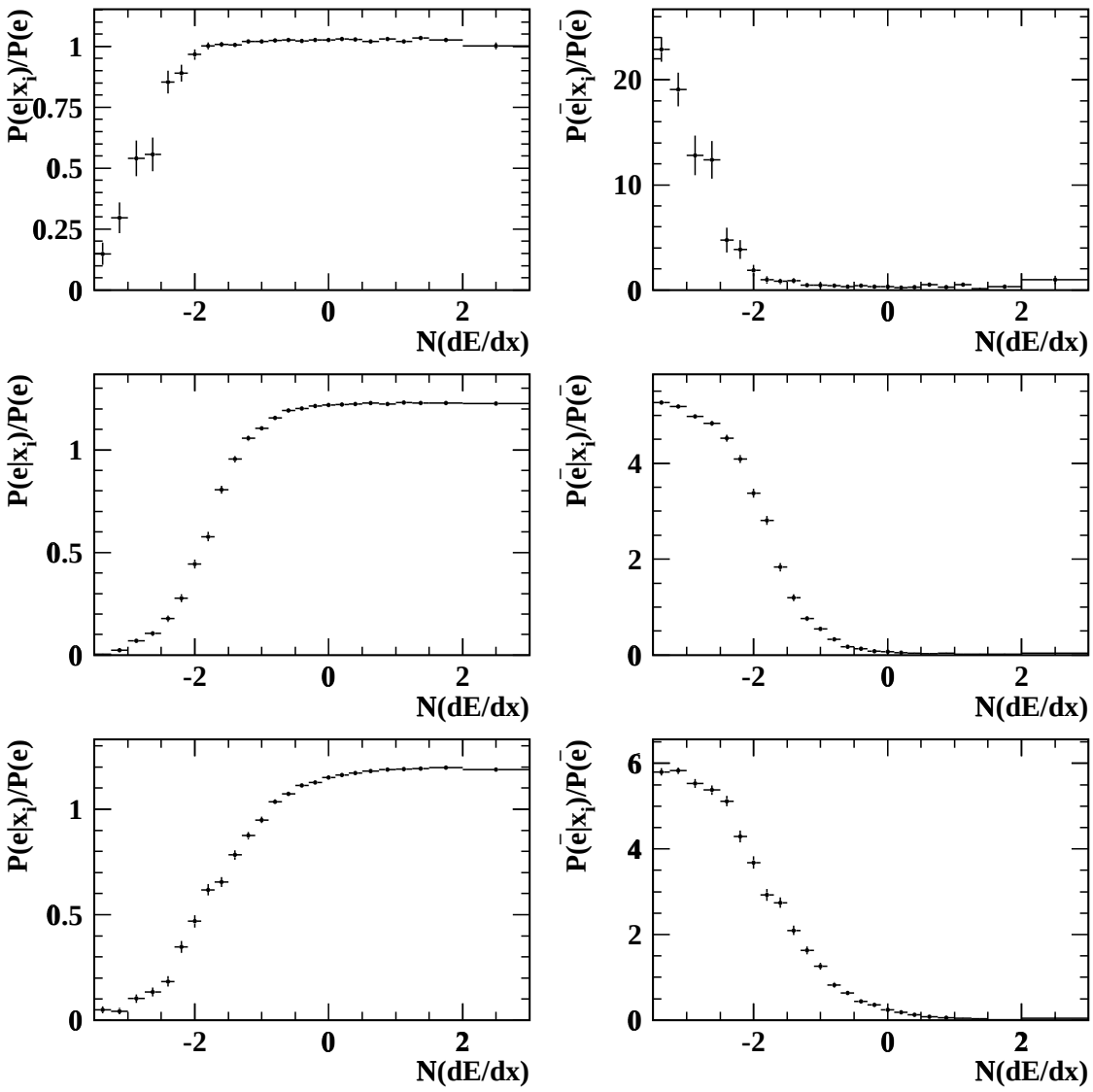

Figure A.4: Reference histograms for $N(\mathrm{d}E/\mathrm{d}x)$ in the three momentum bins (top to bottom) $p \leq 5$ GeV, $5 < p \leq 20$ GeV and $p > 20$ GeV. The histograms on the left describe signal ($\tau^- \to \mathrm{e}^-\bar{\nu}_\mathrm{e}\nu_\tau$), while the histograms on the right describe the background from hadronic τ decays.

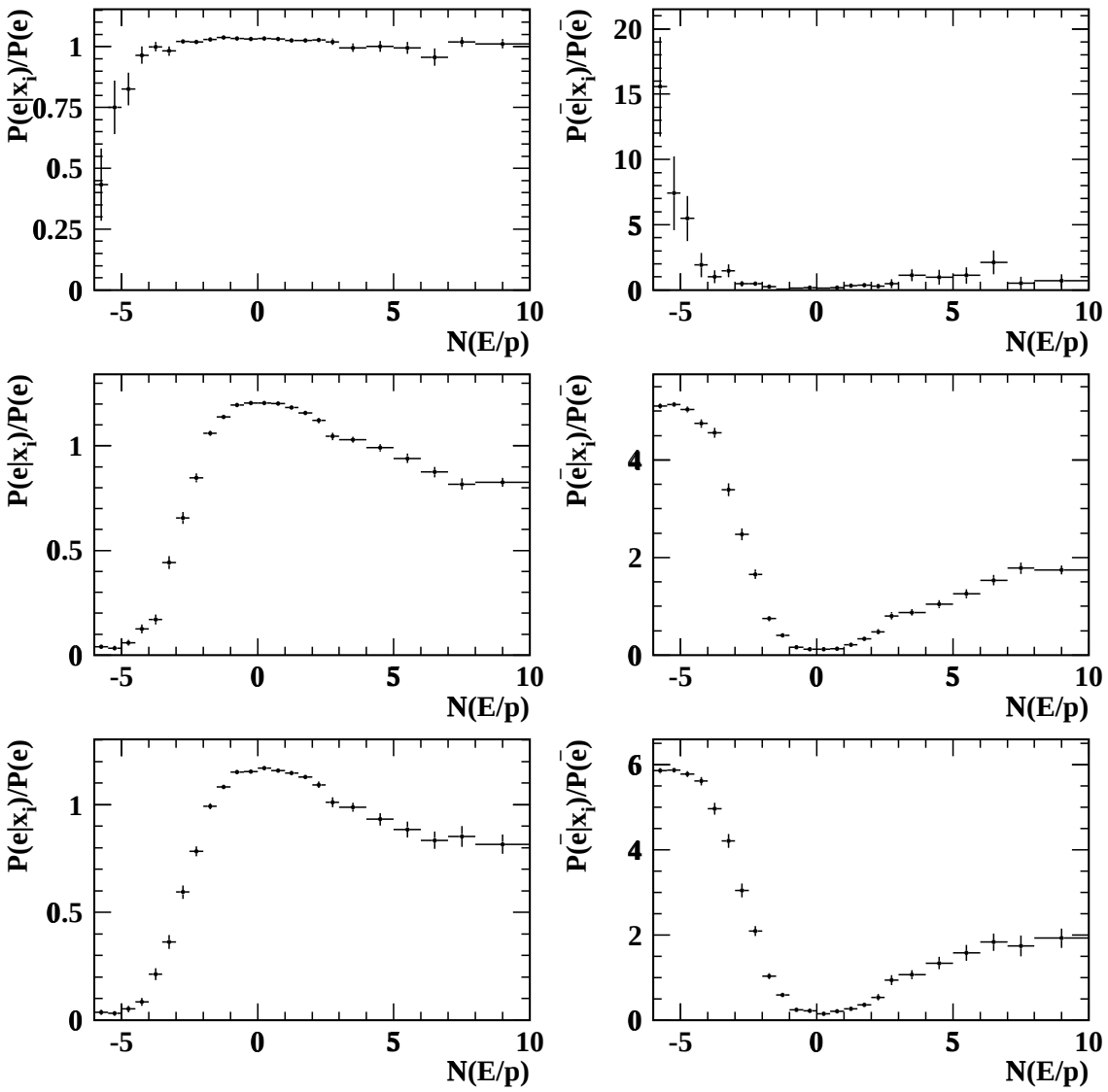

Figure A.5: Reference histograms for $N(E/p)$ in the three momentum bins (top to bottom) $p \leq 5$ GeV, $5 < p \leq 20$ GeV and $p > 20$ GeV. The histograms on the left describe signal ($\tau^- \to e^- \bar{\nu}_e \nu_\tau$), while the histograms on the right describe the background from hadronic τ decays.

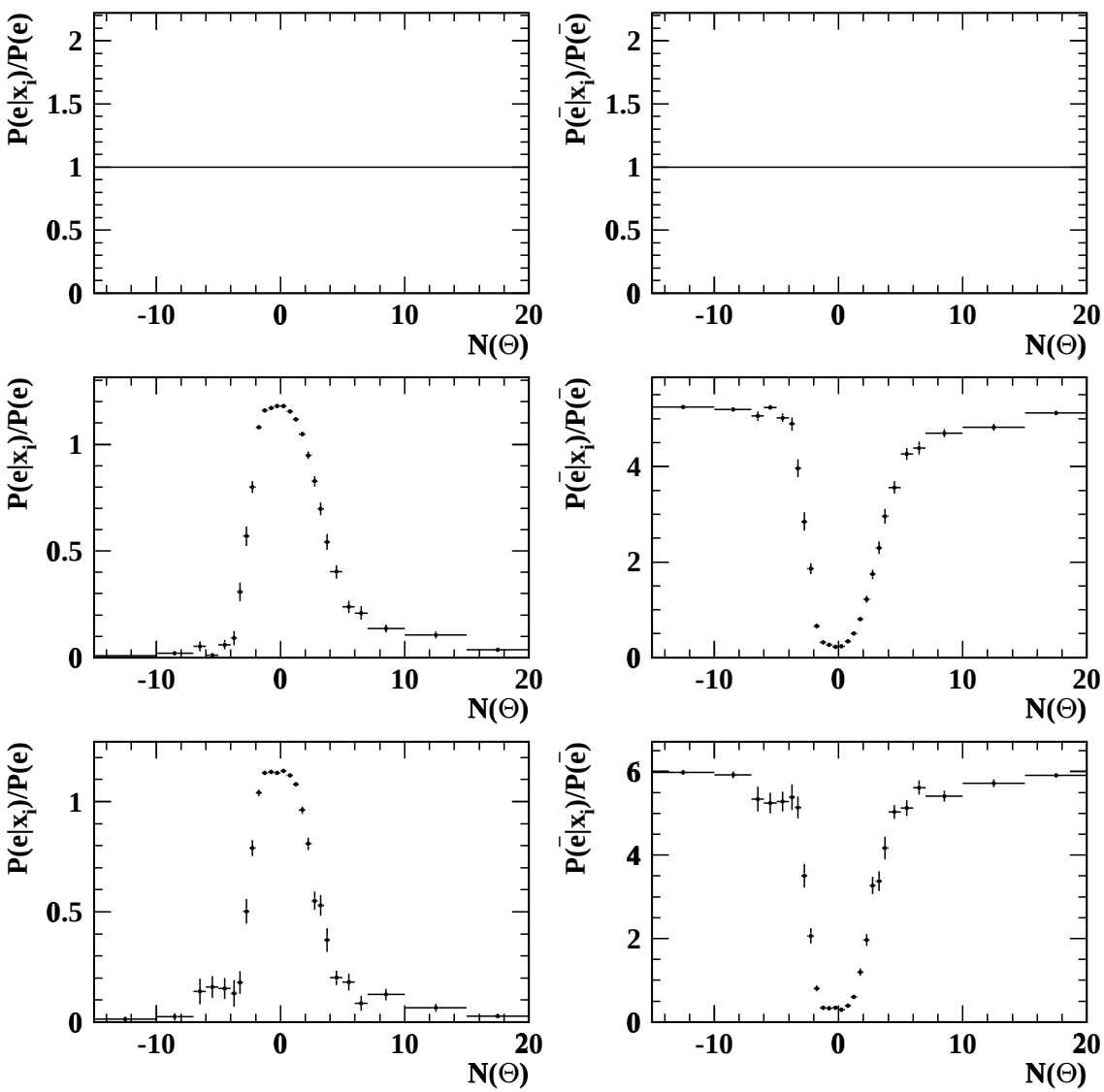

Figure A.6: Reference histograms for $N(\Delta\theta)$ in the three momentum bins (top to bottom) $p \leq 5$ GeV, $5 < p \leq 20$ GeV and $p > 20$ GeV. Because $N(\Delta\theta)$ is not defined for $p \leq 5$ GeV, the first set of histograms are empty. The histograms on the left describe signal ($\tau^- \to e^- \bar{\nu}_e \nu_\tau$), while the histograms on the right describe the background from hadronic τ decays.

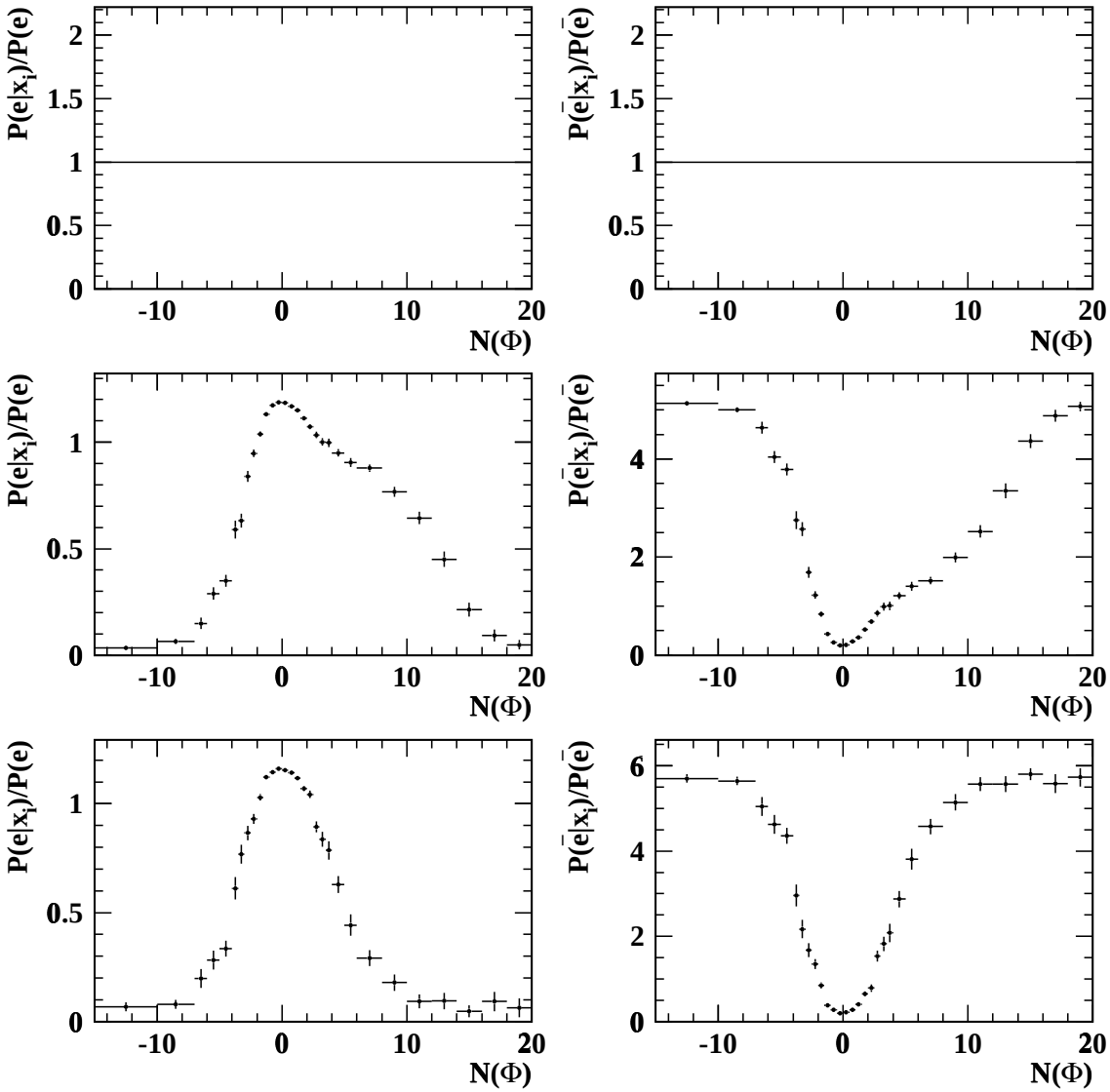

Figure A.7: Reference histograms for $N(\Delta\phi)$ in the three momentum bins (top to bottom) $p \leq 5$ GeV, $5 < p \leq 20$ GeV and $p > 20$ GeV. Because $N(\Delta\phi)$ is not defined for $p \leq 5$ GeV, the first set of histograms are empty. The histograms on the left describe signal ($\tau^- \to e^- \bar{\nu}_e \nu_\tau$), while the histograms on the right describe the background from hadronic τ decays.

Appendix B

Running $\alpha_s(m_\tau^2) \rightarrow \alpha_s(m_Z^2)$

This section presents a summary of the mathematical formalism used to evolve the measurement of $\alpha_s(m_\tau^2)$ from the τ mass scale to the Z^0 mass scale, and is taken primarily from [60]. The QCD beta function governs the evolution of α_s through the renormalization group (RG) equations:

$$\frac{da}{d\ln\mu^2} = \beta(a) = -a^2(\beta_0 + \beta_1 a + \beta_2 a^2 + \beta_3 a^3) + \mathcal{O}(a^6) \tag{B.1}$$

where $a \equiv \alpha_s/\pi$. The first three β coefficients are independent of the renormalization scheme, however $\beta_{\geq 3}$ are scheme dependent. The β_3 coefficient has recently been calculated up to four loops in the $\overline{\rm MS}$ scheme [59].

$$\begin{aligned}
\beta_0 &= \tfrac{1}{4}\left[11 - \tfrac{2}{3}n_f\right] \\
\beta_1 &= \tfrac{1}{16}\left[102 - \tfrac{38}{3}n_f\right] \\
\beta_2 &= \tfrac{1}{64}\left[\tfrac{2857}{2} - \tfrac{5033}{18}n_f + \tfrac{325}{54}{n_f}^2\right] \\
\beta_3(\overline{\rm MS}) &= \tfrac{1}{256}\left[\left(\tfrac{149753}{6} + 3564\zeta_3\right) - \left(\tfrac{1078361}{162} + \tfrac{6508}{27}\zeta_3\right)n_f \right. \\
&\quad \left. + \left(\tfrac{50065}{162} + \tfrac{6472}{81}\zeta_3\right){n_f}^2 + \tfrac{1093}{729}{n_f}^3\right]
\end{aligned} \tag{B.2}$$

where n_f is the number of quark flavours with mass less than the renormalization scale μ, and $\zeta_3 = 1.202056903...$ is the Reimann zeta-function.

The four-loop RG equation has been solved by [60] for α_s as an expansion in the

solution to the two-loop RG equation:

$$a(\mu) = a^{(2)}(\mu)\left(1 + c_2(\mu)[a^{(2)}(\mu)]^2 + c_3(\mu)[a^{(2)}(\mu)]^3\right) \tag{B.3}$$

where $a^{(2)}(\mu)$ is the approximate two-loop solution given by

$$a^{(2)}(\mu) = \frac{a(\mu_0)}{K + b_1 a(\mu_0) L + b_1^2 a(\mu_0)^2 (1 - K + L)/K} \tag{B.4}$$

$$c_2(\mu) = b_2(1 - K)$$

$$c_3(\mu) = \frac{b_3}{2}(1 - K^2) + b_1 b_2 K(K - 1 - L) + \frac{b_1^3}{2}\left(L^2 - (1 - K)^2\right)$$

and $K = 1 + \beta_0 a(\mu_0) \ln(\mu^2/\mu_0^2)$, $L = \ln(K)$ and $b_m = \beta_m/\beta_0$. Equations B.3 and B.4 give the value of α_s at energy scale μ explicitly in terms of the value $\alpha_s(\mu_0)$ at some reference scale μ_0.

Heavy particles decouple from the full theory at an energy scale $\mu \ll m$, where m is the mass of the heavy particle. This permits an effective field theory to be constructed in this regime which behaves as if only light particles are present. The parameters of the low-energy effective Lagrangian are related to the parameters of the full theory using matching conditions. In particular, the strong coupling constant α_s in a theory with n_f quark flavours is related to α_s in an effective theory with $n_f - 1$ flavours by a power series

$$a_{nf}(\mu_{\rm th}) = a_{nf-1}\left[1 + \sum_{k=1}^{\infty} C_k(x) a_{nf-1}^k(\mu_{\rm th})\right] \tag{B.5}$$

where the coefficients C_k depend on $x = \ln(\mu_{\rm th}^2/m^2)$ and m is the mass of the heavy quark that was decoupled from the theory at scale $\mu_{\rm th}$.

Matching is done at a scale such that $\mu_{\rm th}/m \sim \mathcal{O}(1)$ to achieve rapid convergence of the series. The functions $C_k(x)$ are obtained by applying the renormalization group

equation B.1 to both sides of expression B.5 and solving the resulting differential equations.

$$C_1 = \frac{x}{2}, \qquad C_2 = c_2 + \frac{19}{24}x + \frac{x^2}{36}$$
$$C_3 = c_3 + \left(\frac{241}{54} + \frac{13}{4}c_2 - \left(\frac{325}{1728} + \frac{c_2}{6}\right)n_f\right)x + \frac{511}{576}x^2 + \frac{x^3}{216} \tag{B.6}$$

The constants c_2, c_3 are normalization-scheme dependent constants of integration which depend on the choice of mass m used as a reference scale. If the RG-invariant $\overline{\rm MS}$ mass is used, they have the values

$$c_2 = -\frac{11}{72}, \qquad c_3 = \frac{82043}{27648}\zeta_3 - \frac{575263}{124416} + \frac{2633}{31104}n_f \tag{B.7}$$

When appropriate matching conditions are taken into account, the evolution of α_s to higher energy scales is essentially independent of the choice of energy scale used to pass heavy quark thresholds. Calculations describing τ dynamics are usually performed using effective field theories with $n_f = 3$ quark flavours, and so the procedure for obtaining $\alpha_s(m_{\rm Z}^2)$ from $\alpha_s(m_\tau^2)$ involves the crossing of two quark thresholds. When running of α_s is accomplished using equation B.3, and matching is performed using equation B.5 at energy scales near the b ($m_{\rm b} = 4.13 \pm 0.06$ GeV) and c ($m_{\rm c} = 1.31 \pm 0.06$ GeV) quark masses, the uncertainty introduced to $\alpha_s(m_{\rm Z}^2)$ has been estimated [60] to be 0.0003.

Bibliography

[1] For an overview of the Standard Model see for example:
F. Halzen and A. D. Martin *Quarks and Leptons: An Introductory Course in Modern Particle Physics*, (John Wiley and Sons, New York, 1984).

[2] Particle Data Group, C. Caso *et al.*, Eur. Phys. J. **C3** (1998) 1.

[3] S.L. Glashow, Nucl. Phys. **B 22** (1961) 579;
S. Weinberg, Phys. Rev. Lett., **19** (1967) 1264;
A. Salam, in: *Elementary Particle Theory, Proc. of the 8th Nobel Symp.*, ed. N. Svartholm (Almquist and Wiksell, Stockholm, 1968), 367.

[4] OPAL Collaboration, G. Abbiendi *et al.*, *A Measurement of the* $\tau^- \to \mathrm{e}^-\bar{\nu}_\mathrm{e}\nu_\tau$ *Branching Ratio*, **CERN-EP/98-175**, (Submitted to Phys. Lett. B.).

[5] P.W. Higgs, Phys. Rev. **145** (1966), 1156.

[6] G. Arnison *et al.*, Phys. Lett. **B122** (1983) 103.

[7] M. Banner *et al.*, Phys. Lett. **B122** (1983) 476.

[8] G. Arnison *et al.*, Phys. Lett. **B126** (1983) 398.

[9] P. Bagnaia *et al.*, Phys. Lett. **B129** (1983) 130.

[10] T.D. Lee and C.N. Yang, Phys. Rev. **104** (1956) 254.

[11] C.S. Wu, E. Ambler, R.W. Hayward, D.D. Hoppes, R.P. Hudson, Phys. Rev. **105** (1957) 1413.

[12] N. Cabibbo, Phys. Rev. Lett. **10** (1963), 531;
M. Kobayashi and T. Maskawa, Prog. Theor. Phys., **49**, (1973), 652.

[13] Super-Kamiakande Collaboration, Y. Fukuda *et al.*, Phys. Rev. Lett. **81** (1998) 1562.

[14] M.L. Perl *et al.*, Phys. Rev. Lett. **35** (1975) 1489; M.L. Perl *et al.*, Phys. Lett. **B63** (1976) 466.

[15] Y.S. Tsai, Phys. Rev. **D4** (1971) 2821.

[16] W.J. Marciano and A. Sirlin, Phys. Rev. Lett. **61** (1988) 1815.

[17] C.S. Lam and T.M. Yan, Phys. Rev. **D16** (1977) 703.

[18] E. Braaten, Phys. Rev. Lett. **60** (1988) 1606; E. Braaten, Phys. Rev. **D39** (1989) 1458.

[19] E. Braaten, S. Narison and A. Pich, Nucl. Phys. **B373** (1992) 581.

[20] F. Le Diberder and A. Pich, Phys. Lett. **B286** (1992) 147; F. Le Diberder and A. Pich, Phys. Lett. **B289** (1992) 165.

[21] M.A. Shifman, A.I. Vainshtein and V.I. Zakharov, Nucl. Phys. **B147** (1979) 385, 448, 519.

[22] E. Braaten and C.S. Li, Phys. Rev. **D42** (1990) 3888.

[23] A. Pich, **FTUV-97-03** (1997), Invited talk at 20th Johns Hopkins Workshop on Current Problems in Particle Theory, Heidelberg (1996).

[24] S. Narison, Nucl. Phys. **B40** (Proc. Suppl.) (1995) 47.

[25] K.G. Chetyrkin and A. Kwiatkowski, Z. Phys. **C59** (1993) 525.

[26] ALEPH Collaboration, R. Barate *et al.*, Eur. Phys. J. **C4** (1998) 409.

[27] OPAL Collaboration, K. Ackerstaff *et al.*, *Measurement of the Strong Coupling Constant α_s and the Vector and Axial-Vector Spectral Functions in Hadronic Tau Decays*, **CERN-EP/98-102**, (submitted to Eur. Phys. J.).

[28] LEP Design Report(Vol II); The LEP Main Ring CERN-LEP/84-01 (June 1984).

[29] G. Altarelli, R. Kleiss and C. Verzegnassi (editors) *Z Physics at LEP 1*, CERN 89-08, Vol 1 and 2 (21 September 1989).

[30] The LEP injector Study Group, LEP Design Report (Vol I); The LEP Injector Chain CERN-LEP/TH/83-29 (June 1983).

[31] OPAL Collaboration, K. Ahmet *et al.*, Nucl. Inst. and Meth. **A305** (1991) 275; P.P. Allport *et al.*, Nucl. Inst. and Meth. **A346** (1994) 476; P.P. Allport *et al.*, Nucl. Inst. and Meth. **A324** (1993) 34; O. Biebel *et al.*, Nucl. Inst. and Meth. **A323** (1992) 169.

[32] S. Anderson *et al.*, *Nucl. Instrum. Methods* **A403** (1998) 326. and references therein.

[33] M. Hauschild *et al.*, Nucl. Inst. and Meth. **A314** (1992) 74.

[34] S. Kluth and D.R. Ward, *A Study of the Performance of the OPAL Electromagnetic Calorimeter using* $e^+e^-\gamma$ *Events*, OPAL internal note **TN108** (July 17 1992).

[35] Ping Hu, *A Study of the Response of the OPAL Calorimeter to Hadrons*, M.Sc. Thesis, University of Victoria, (1995).

[36] KORALZ 4.0 generator: S. Jadach, B.F.L. Ward, and Z. Wąs, Comp. Phys. Comm. **79** (1994) 503.

[37] BABAMC generator: F.A. Berends, R. Kleiss and W. Hollik, Nucl. Phys. **B304** (1988) 712.

[38] BHWIDE generator: S. Jadach, W. Placzek and B.F.L. Ward, Phys. Lett. **B390** (1997) 298.

[39] JETSET 7.4 generator: Sjöstrand, Comp. Phys. Comm. **82** (1994) 74.

[40] VERMASEREN 1.01 generator: R. Bhattacharya, J. Smith and G. Grammer, Phys. Rev. **D15** (1977) 3267; J. Smith, J.A.M. Vermaseren and G. Grammer, Phys. Rev. **D15** (1977) 3280.

[41] GRC4F V1.1 generator: J. Fujimoto *et al.*, Comp. Phys. Comm. **100** (1997) 128.

[42] FERMISV generator: J. Hilgart, R. Kleiss and F. Le Diberder, Comp. Phys. Comm. **75** (1993) 191.

[43] R. Brun *et al.*, GEANT3, CERN Report DD/EE/84-1 (1989).

[44] J. Allison *et al.*, Nucl. Inst. and Meth. **A317** (1992) 47.

[45] TAUOLA 2.0 generator: S. Jadach *et al.*, Comp. Phys. Comm. **76** (1993) 361.

[46] OPAL Collaboration, G. Alexander *et al.*, Phys. Lett. **B266** (1991) 201;
OPAL Collaboration, P. Acton *et al.*, Phys. Lett. **B288** (1992) 373.

[47] OPAL Collaboration, G. Alexander *et al.*, Z. Phys. **C52** (1991) 175.

[48] M.A. Thompson, private communication; M.A. Thompson, *LEP 1 Tau Pair Cross Section and Forward-Backward Asymmetry*, OPAL internal note **TN490** (June 10 1997).

[49] OPAL Collaboration, G. Alexander *et al.*, Phys. Lett. **B369** (1996) 163; S. Bishop, P. Giguere, I. Lawson, and R. Sobie, *A New Measurement of the* $\tau^- \to e^- \bar{\nu}_e \nu_\tau$ *Branching Ratio*, OPAL internal note **TN285**, (1995); S. Bishop *et al.*, *Update of the* $\tau^- \to e^- \bar{\nu}_e \nu_\tau$ *Branching Ratio Measurement*, OPAL internal note **TN303**, (1995).

[50] OPAL Collaboration, R. Akers *et al.*, Phys. Lett. **B328** (1994) 207; A.Astbury *et al.*, *A New Clustering Algorithm for* τ *decays*, OPAL **TN139**, (1993); R.Sobie, *A New Clustering Algorithm for* τ *decays: II*, OPAL internal note **TN186**, (1993).

[51] S. Robertson, R. Sobie and J. White, *Measurement of the* $\tau^- \to e^- \bar{\nu}_e \nu_\tau$ *Branching Ratio*, OPAL internal note **TN539**, (April 21, 1998).

[52] J.M. Roney, *Recent Tau Decay Results from OPAL*, Proceedings of the International Europhysics Conference on High Energy Physics, Jerusalem, Israel 19-26 August 1997, to be published.

[53] OPAL Collaboration, R. Akers *et al.*, Z. Phys. **C66** (1995) 543.

[54] D.I. Britton *et al.*, Phys. Rev. Lett. **68** (1992) 3000.

[55] G. Czapek *et al.*, Phys. Rev. Lett. **70** (1993) 17.

[56] OPAL Collaboration, G. Alexander *et al.*, Phys. Lett. **B374** (1996) 341.

[57] BES Collaboration, J.Z. Bai *et al.*, Phys. Rev. **D53** (1996) 20.

[58] P.A. Rączka, Phys. Rev. **D57** (1998) 6862.

[59] T. van Ritbergen, J.A.M. Vermaseren and S.A. Larin, Phys. Lett. **B400** (1997) 379.

[60] G. Rodrigo, A. Pich, and A. Santamaria, Phys. Lett. **B424** (1998) 367.